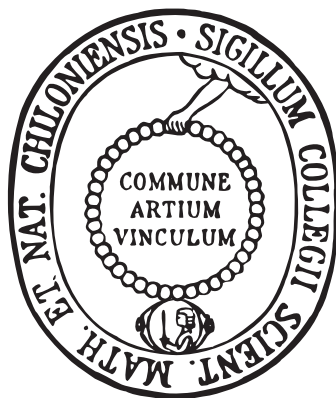Christian-Albrechts-Universität zu Kiel
Institut für Theoretische Physik und Astrophysik

Formation of Metal–Polymer Nanocomposites by Plasma-Based Deposition Methods: Kinetic Monte Carlo and Molecular Dynamics Simulations

Dissertation
zur Erlangung des Doktorgrades
der Mathematisch-Naturwissenschaftlichen Fakultät
der Christian-Albrechts-Universität zu Kiel

vorgelegt von
Jan Willem Abraham

Kiel, 2018

Gutachter

Prof. Dr. Michael Bonitz
Institut für Theoretische Physik und Astrophysik
Christian-Albrechts-Universität zu Kiel
Leibnizstr. 15
24098 Kiel
Germany

Tag der mündlichen Prüfung

Zum Druck genehmigt

gez.

Publications of the author

Articles in peer-reviewed journals

- M. Bonitz, A. Filinov, J. W. Abraham, and D. Loffhagen, *Extending ab initio plasma-surface simulations to experimentally relevant scales*, submitted to Plasma Sources Science and Technology, preprint: arXiv:1802.08710 [physics.plasm-ph] (2018)

- Ott

- Polonsk

- EPJD

- J. W. Abraham, and M. Bonitz, *Molecular dynamics simulation of Ag–Cu cluster growth on a thin polymer film*, Contributions to Plasma Physics **58**, 164 (2018)

- J. W. Abraham, T. Strunskus, F. Faupel, and M. Bonitz, *Molecular dynamics simulation of gold cluster growth during sputter deposition*, Journal of Applied Physics **119**, 185301 (2016)

- J. W. Abraham, N. Kongsuwan, T. Strunskus, F. Faupel, and M. Bonitz, *Simulation of nanocolumn formation in a plasma environment*, Journal of Applied Physics **117**, 014305 (2015)

- J. W. Abraham, and M. Bonitz, *Quantum Breathing Mode of Trapped Particles: From Nanoplasmas to Ultracold Gases*, Contributions to Plasma Physics **54**, 27 (2014)

- J. W. Abraham, M. Bonitz, C. McDonald, G. Orlando, and T. Brabec, *Quantum breathing mode of trapped systems in one and two dimensions*, New Journal of Physics **16**, 013001 (2014)

- C. R. McDonald, G. Orlando, J. W. Abraham, D. Hochstuhl, M. Bonitz, and T. Brabec, *Theory of the Quantum Breathing Mode in Harmonic Traps and its Use as a Diagnostic Tool*, Physical Review Letters **111**, 256801 (2013)

- J. W. Abraham, K. Balzer, D. Hochstuhl, and M. Bonitz, *Quantum breathing mode of interacting particles in a one-dimensional harmonic trap*, Physical Review B **86**, 125112 (2012)

Book chapter

- L. Rosenthal, T. Strunskus, F. Faupel, J. W. Abraham, and M. Bonitz, "Kinetic Monte Carlo Simulations of Cluster Growth and Diffusion in Metal-Polymer Nanocomposites", in *Complex Plasmas: Scientific Challenges and Technological Opportunities*, Vol. 82, edited by M. Bonitz, J. Lopez, K. Becker, and H. Thomsen, Springer Series on Atomic, Optical and Plasma Physics (Springer, Cham, 2014), pp. 321–370

Selected contributions to workshops and conferences

- J. W. Abraham, T. Strunkus, F. Faupel, and M. Bonitz, *"Simulation of (bi-)metallic cluster growth on polymer surfaces during sputter deposition"*, poster presentation at 44th EPS Conference on Plasma Physics, Belfast (June 27, 2017)

- J. W. Abraham, *"Molecular Dynamics Simulation of Au Cluster Growth During Sputter Deposition"*, contributed talk at 3rd German–Czech workshop "Nanoparticles from low temperature plasma and their applications", Lübeck (May 19, 2016)

- J. W. Abraham, *"Molecular Dynamics Simulation of Gold Cluster Growth on a Polymer Surface"*, contributed talk at TUM-DESY-CAU workshop "The polymer–metal interface", Garching (March 2, 2016)

- J. W. Abraham, K. Fujioka, S. Wolf, T. Strunkus, F. Faupel, and M. Bonitz, *"Simulation of nanocolumn formation in a plasma environment"*, poster presentation at 42nd EPS Conference on Plasma Physics, Lisboa (June 25, 2015)

- J. W. Abraham, T. Strunskus, F. Faupel, M. Bonitz, *"Simulation of Nanocolumn Formation in a Plasma Environment"*, contributed talk at ICOPS 2015 conference, Belek (May 26, 2015)

- J. W. Abraham, M. Bonitz, *"Simulation of Nanofilm Formation in Low-Temperature Plasmas"*, contributed talk at 56th Annual Meeting of the APS Division of Plasma Physics, New Orleans (October 29, 2014)

- J. W. Abraham, *"Kinetic Monte Carlo Simulations of Nanofilm Formation"*, lecture held at 4th Summer Institute "Complex Plasmas", South Orange (August 5, 2014)

- J. W. Abraham, M. Bonitz, *"Kinetic Monte Carlo Simulation of Nanocolumn Formation"*, contributed talk at 2nd German–Czech workshop "Nanoparticles from low temperature plasma and their applications", Prague (May 23, 2014)

Abstract

In this thesis, the formation of metal–polymer nanocomposites is studied by means of kinetic Monte Carlo (KMC) and molecular dynamics (MD) simulations.

The KMC simulations, which are considered first, are used to investigate the growth of metallic nanocolumns in a polymer host matrix during co-deposition of metal and polymer. The employed simulation model is an extended version of a previous model presented by Rosenthal *et al.* (Journal of Applied Physics **114**, 044305 (2013)) to make a similar study of nanocolumnar growth. The modifications of the model presented in this work are twofold: firstly, a process has been implemented to account for the creation of defects in the surface of the polymer, which is an important side effect of the sputter deposition technique. In doing so, the simulations are intended to answer the question if the growth of nanocolumns is also possible if sputter deposition is used instead of thermal evaporation. The primary effect of the occurrence of surface defects is an increased amount of trapped metal atoms and clusters; it is not known in advance how this affects the more complex formation of nanocolumns, which requires that initially spherical clusters—the "seeds" of the columns—reach a critical size. The results discussed in this work cover a broad regime of simulation parameters and thus provide a comprehensive answer to the question regarding the influence of defects. In addition to this, the second modification that has been made is the implementation of a process which describes the diffusion of metal atoms and clusters in the polymer bulk. As the influence of bulk diffusion has not been considered in the above mentioned work by Rosenthal *et al.*, it is now investigated for different ratios of surface and bulk diffusion coefficients.

The experimental scenario considered in the other part of this work is the formation of a nanogranular metal film on a polymer substrate during sputter deposition. In order to investigate such a process, a Langevin-based atomistic MD simulation model is developed, which allows one to reproduce the behavior on experimentally relevant time scales by performing the simulations with very large values of the deposition rate and the diffusion coefficients of metal atoms. Unlike conventional MD simulations of processes on a surface, which usually include an atomistic treatment of all involved particles, the atomistic description in this model is restricted to the deposited metal atoms; the polymer substrate, however, is modeled as a continuous medium on which and in which the metal atoms may perform random walks. In a first study, the time evolution of the morphology of a gold film is studied for various different simulation parameters. The employed method is extensively tested and a comprehensive comparison with experimental reference data is made. As the comparison displays good agreement over wide ranges of film thicknesses, another study is performed for the deposition of silver and copper instead of gold. The goal of that investigation is to assess to what degree

the tendency of both materials to occur in separated phases in the bulk also plays a role in the formation of nanofilms.

Kurzbeschreibung

In dieser Arbeit wird die Entstehung von Metall-Polymer-Nanokompositen mithilfe der Simu-
lationsmethoden "kinetic Monte Carlo" (KMC) und "molecular dynamics" (MD) untersucht.

Zuerst werden die Ergebnisse von KMC-Simulationen betrachtet, um das Wachstum metal-
lischer Nanosäulen in einer Polymermatrix während der Co-Deposition von einem Metall und
einem Polymer zu untersuchen. Das verwendete Simulationsmodell stellt eine Erweiterung
eines früheren Modells dar, welches von Rosenthal *et al.* entwickelt und bereits in einer ähnli-
chen Untersuchung des Wachstums von Nanosäulen angewendet wurde (Journal of Applied
Physics **114**, 044305 (2013)). Die Veränderungen am Modell sind von zweierlei Art: Zum einen
wurde ein Prozess implementiert, der eine wichtige Begleiterscheinung des Sputterdepositi-
onsverfahrens beschreibt, nämlich die Erzeugung von Defekten in der Polymeroberfläche.
Auf diese Weise sollen die Simulationen Auskunft darüber geben können, ob Nanosäulen
ebenfalls wachsen können, wenn die Deposition mittels Sputtern anstelle von thermischer
Verdampfung geschieht. Die primäre Auswirkung der Defekte ist eine zunehmende Immobili-
sierung der Metallatome und -cluster. Dabei ist nicht im Voraus bekannt, wie sich dies auf
den komplexen Wachstumsprozess von Nanosäulen auswirkt. Jener verlangt, dass anfänglich
sphärische Cluster – die "Wachstumskeime" der Säulen – eine kritische Größe erlangen. Da
die Ergebnisse in dieser Arbeit einen breiten Bereich an Simulationsparametern abdecken,
kann eine umfassende Antwort auf die Frage nach dem Einfluss der Defekte gegeben werden.
Zusätzlich dazu wird ein zweiter Prozess untersucht, der die Diffusion von Metallatomen und
-clustern im Innern des Polymers beschreibt. Da diese sogenannte Bulk-Diffusion noch nicht
in der oben genannten Arbeit von Rosenthal *et al.* berücksichtigt wurde, wird sie nun für
verschiedene Verhältnisse von Oberflächen- und Bulk-Diffusionskoeffizienten untersucht.

Der andere Teil dieser Untersuchungen widmet sich der Entstehung einer nanostruktu-
rierten Metallschicht auf einem Polymersubstrat während der Sputterdeposition. Zu diesem
Zwecke wird ein atomistisches MD-Simulationsmodell auf Basis der Langevin-Dynamik
entwickelt, welches es ermöglicht, das Verhalten auf experimentell relevanten Zeitskalen auf
deutlich kürzere Simulationen abzubilden. Dafür ist es notwendig, dass besonders hohe De-
positionsraten und Diffusionskoeffizienten der Metallatome in den Simulationen verwendet
werden. Anders als in gewöhnlichen MD-Simulationen von Oberflächenprozessen, welche
alle zugehörigen Teilchen atomistisch behandeln, beschränkt sich die atomistische Behand-
lung in diesem Modell auf die deponierten Metallatome; das Polymersubstrat hingegen wird
als kontinuierliches Medium beschrieben, in dem – und *auf* dem – die Metallatome einen
Random Walk durchführen. In einer ersten Untersuchung wird die Zeitentwicklung der
Morphologie einer dünnen Goldschicht für verschiedene Simulationsparameter untersucht.

Die verwendete Methode wird ausführlich getestet, und ein umfangreicher Vergleich mit experimentellen Referenzdaten wird durchgeführt. Da dieser Vergleich eine weitgehende Übereinstimmung für viele Schichtdicken liefert, schließt sich eine weitere Untersuchung an, in der die Deposition von Silber und Kupfer anstelle von Gold betrachtet wird. Dabei soll herausgefunden werden, in welchem Maße die Tendenz beider Materialien, in voneinander getrennten Phasen in Festkörpern aufzutreten, auch bei der Entstehung einer Nanoschicht eine Rolle spielt.

Contents

Chapter 1

Motivation and Outline

The research on complex materials on the nanoscale has rapidly advanced since the end of the twentieth century [1–3]. At that, small particles with sizes between 1 nm and 100 nm in at least one dimension [4]—so-called nanoparticles—have been of particular interest as their large surface-to-volume ratio leads to several properties which are clearly different from the corresponding properties of the bulk material [5]. Already today, nanoparticles are of enormous technological relevance [6, 7], but they are still in the focus of fundamental research [8].

A specific usage of nanoparticles is their incorporation into multifunctional composite materials, which finds application in various fields [9], for example, in electronics [10–15], plasmonics [16–19], food packaging [20–22] and medicine [23–25]. In recent years, much attention has been paid to a specific class of nanocomposites consisting of nanosized metal particles which are dispersed in or on a polymer host material [2, 9, 26–28]. These so-called metal–polymer nanocomposites offer the potential to be fabricated at low cost and with reproducible magnetic, electronic, optical and catalytic properties [2, 29–32]. Even though the production of metal–polymer nanocomposites is already routinely carried out using physical, chemical or physio-chemical methods [2], the highly complex formation mechanisms are still subject to ongoing research. It is of particular interest how the sizes, shapes, compositions and number densities of the metallic particles evolve during the formation process. Although the experimental diagnostics are continuously improved—for example, Schwartzkopf *et al.* presented the first real-time and *in-situ* results on the growth kinetics of gold nanostructures during sputter deposition [32]—there is still the need for further investigations to get an improved understanding of how the macroscopic details of the experimental set-up affect the behavior of atoms and clusters on microscopic scales. In fact, there already exist experimental methods to obtain three-dimensional pictures of single clusters at an atomic resolution [33], but the available studies on the formation of metal–polymer nanocomposites are typically lacking atomistic details.

Over the last few years, it turned out that the understanding of the nanocomposite formation process can greatly benefit from computer simulations [9, 34–39]. In the present thesis, we will therefore continue along this path and explore new capabilities of modeling and simulation. At that, we will concentrate on physical vapor deposition methods [40], in particular plasma-

based sputter deposition as this technique is frequently used in experiments and still offers the potential for fundamental research on the physics of complex plasmas [41, 42]. While nanomaterials and nanoparticles are widely associated with miniaturization or very small objects, the required system sizes, often exceeding several ten thousands of atoms, still pose a big challenge to modern particle-based simulation methods. Even more than that, the relevant time scales of experiments, exceeding seconds or minutes, are far out of reach of many simulation methods, in particular *ab-initio* methods such as time-dependent density functional theory [43, 44] or approaches based on nonequilibrium Green functions [45–47].

One of the standard methods to overcome the limitations of length and time scales in simulations is the kinetic Monte Carlo (KMC) method. It is a highly coarse-grained statistical method which is frequently applied to simulate various problems occurring in surface and materials science. Recently, it has been demonstrated that it also yields an adequate description of the formation of metal–polymer nanocomposites [9, 34–36, 38]. The simulation model presented by Rosenthal *et al.* [9, 36], which borrows some ideas from on older model by Thran and Faupel [38], has not only been applied to study the growth of spherical metal clusters on a polymer surface or in a polymer matrix, but also to explain the transition from a spherical to a columnar growth mode of nanostructures [34, 48]. The latter observation has also been made in preceding experiments described in Ref. [30]. The crucial technique of the mentioned KMC simulations is the description of atoms and clusters in terms of simple geometric shapes, and the polymer is treated as a continuous medium that provides the space for the diffusion of atoms and clusters. While the deposition technique used for the experiments in Ref. [30] was the simultaneous thermal evaporation of metal and polymer, it remained an open question whether nanocolumns can also be produced using sputter deposition for at least one of the components. In this work, we will pursue this question by using an extended version of Rosenthal's simulation model which accounts for the impact of highly energetic particles ejected from the plasma. This will be accomplished by assuming that each impact creates a defect in the polymer surface at which passing metal atoms or clusters are trapped. As this process contributes to a strong reduction of the amount of diffusing particles, one can expect that it has an important effect on the growth kinetics. Beyond that, the KMC study in this work contains two novelties: first, the simulations account for the diffusion of atoms and clusters in the polymer bulk—for the previous investigation of columnar growth in Ref. [34], this mechanism was neglected. Second, the results will be illustrated with 3D rendering images of the simulated columns and clusters. These images—which were created with the software *Blender* [49]—will provide an insightful supplement to the purely quantitative description that always hides certain details.

Despite the merits of KMC—the ability to explore large length and time scales—we will see that the method only works at the cost of rigid approximations and several uncertainties introduced by the establishment of a simple simulation model. In some cases, it may therefore be advantageous to resort to another well-established method, namely atomistic molecular dynamics (MD) simulations [41, 50]. Describing atoms as classical pointlike particles interacting via empirical force fields, the MD method propagates the Newtonian equations of motion to produce numerically exact trajectories of all involved particles. As conventional MD simulations are often limited to time scales of nanoseconds [50], a variety of techniques has been developed to extend the accessible time scales by many orders of magnitude [50,

51]. Although those so-called acceleration methods are always bound by certain restrictions, they make MD a valuable tool for the study of nanomaterials. In particular, despite various remaining challenges, the still emerging field that is concerned with the interaction of a plasma and a surface has already greatly benefited from MD simulations and the presently available acceleration techniques [50, 52, 53].

Due to the important advantages offered by atomistic simulations, another part of this work is devoted to the application of MD simulations in the field of metal–polymer nanocomposites. While MD simulations of composite systems often concentrate on processes on a metallic surface [52–56], much less attention is paid to polymer substrates, see, e. g., Refs. [37, 57–59]. The reasons are that a particle-based treatment of polymer chains is computationally very expensive and the established acceleration techniques work best for crystalline surfaces. To overcome these difficulties, this work will introduce a new simulation scheme for the growth of metal clusters on a polymer surface during sputter deposition. While the treatment of the metal atoms is completely particle-based, the simulation scheme also adopts several techniques from KMC simulations. For example, the polymer is modeled as a continuous background medium, which is a strong simplification as compared to the complex particle-based polymer models. The computational resources saved by this technique can be spent on incorporating a large amount of metal atoms; these are of particular interest with respect to the resulting film morphology. In fact, the number of deposited metal particles used for the results in this work exceeds several hundred thousand; that is much more than the numbers in comparable studies, e. g., Refs. [37, 60]. As the modeling of the polymer substrate is realized by performing Langevin dynamics for all metal atoms, it is possible to manually set the values of all involved diffusion coefficients describing the motion of metal atoms on the polymer surface and in the polymer bulk. Thus, performing the simulations with very large values of the deposition rate and the diffusion coefficients, the method also permits an imitation of the behavior on experimental time scales. Comparing with experimental data from Ref. [61], we will see that a realistic description of the morphology of a thin film can be obtained if the simulations maintain the ratio of the experimental values of the deposition rate and the surface diffusion coefficient. All simulations required for these comparisons were performed for the deposition of gold (Au) atoms. This material was also kept for various additional tests and applications, which will be in the primary focus of the MD studies in this work. Nevertheless, since the comparison with experimental results was promising, the results for gold were also extended by replacing the deposited material. As there is still just little knowledge about the miscibility of silver (Ag) and copper (Cu) on the nanoscale [62, 63], exactly these materials were chosen and studied for different ratios of their deposition rates. Hence, in another part of this work, we will consider the morphology of an Ag–Cu film and focus on the separation of both phases in the clusters.

Thesis outline

- Chapter 2 is intended to give a rather general overview of metal–polymer nanocomposites. In order to motivate the establishment of the simulation models in this work, several important physical properties and experimental techniques are explained.

- Chapter 3 serves as an introduction to the KMC and the MD method. Several technical aspects are already discussed, but most details referring to specific applications are given in later chapters.

- Chapter 4 is devoted to KMC simulations of nanocolumnar growth. The chapter contains a detailed description of the simulation model and a variety of results for different simulation parameters.

- In Chapter 5, the MD simulation scheme is developed and the rescaling method for the deposition rate and the diffusion coefficients is explained. The method is applied to the growth of gold clusters on a polymer surface during sputter deposition. A comprehensive comparison with experimental film morphology data is made.

- The entire Chapter 6 extends the discussion of the rescaling method presented in Chapter 5. This involves a comparison with an alternative approach based on rate equations.

- In Chapter 7, the MD simulation scheme is applied to study the morphology and phase separation of Ag–Cu clusters growing during sputter deposition.

- A concluding discussion of the results is given in Chapter 8.

Chapter 2

Metal–Polymer Nanocomposites

In this work, we use the term "metal–polymer nanocomposite" for two different system types [9, 26]: the first type consists of arbitrarily shaped metallic nanoparticles that are embedded in a "three-dimensional" polymer host matrix. For the present investigations, the thickness of those systems will remain below 100 nm. The other type refers to a thin nanogranular metal film on a polymer substrate; it is typical of such systems that the involved metal clusters are only partially embedded in the polymer. Sometimes, these systems are considered to be "two-dimensional", for example, to put the focus on the interfacial area of both components [64]. Both types of metal–polymer nanocomposites are often prepared on wafers whose side lengths are on the order of centimeters [61, 65]. Therefore, the characteristic nanoscale can only be found in the dimensions of the metallic particles and the thickness of the whole composite. From the theoretical perspective, it will be reasonable to treat the systems as if the two dimensions parallel to the wafer surface are infinitely large.

In this chapter, we review several fundamental aspects of metal–polymer nanocomposites, which will later help us to motivate the establishment of the simulation models. In Sec. 2.1, we are concerned with several important experimental techniques, and in Sec. 2.2, we discuss the behavior of the system during the deposition process.

2.1. Important experimental techniques

This section is intended to give a brief overview of the experimental techniques that are important for the understanding of the simulation methods used in this work. In Sec. 2.1.1, we will focus on the relevant physical vapor deposition methods. Then, in Sec. 2.1.2, we will discuss the grazing-incidence small-angle X-ray scattering technique—a diagnostic tool for the characterization of the film morphology.

2.1.1. Deposition methods

The investigations in this work are intended to extend the recent work by Rosenthal *et al.* [9, 34, 36]. Therefore, we only consider metal–polymer nanocomposites produced by physical vapor deposition methods at room temperature (or similarly low, but unspecified

temperatures). In particular, we assume that all metallic constituents are deposited in the form of isolated atoms—the deposition of metal clusters on a polymer surface using, e. g., gas aggregation sources is another typical experimental technique [35, 39, 66], but it is ignored in this work to reduce the complexity of the problems. All aspects mentioned in the following are of specific importance for later explanations of the simulation schemes. For a rather general overview of deposition methods, it is referred to Refs. [2, 9, 26, 48].

Deposition of metal atoms

A widely used method to deposit metal atoms on a substrate is sputter deposition [67, 68]. The term "sputtering" labels the ejection of atoms from a target material caused by the bombardment of the target with highly energetic particles. Such a process can be repeatedly enforced by exposing the target to a plasma and applying an external electric field to accelerate the ions towards the surface. In order to produce nanomaterials, one must arrange the target and an arbitrary substrate in such a way that the ejected atoms can be collected on the substrate. There, they may take part in highly complex and self-organized film formation processes. The sputter deposition is very popular nowadays because one can achieve very high deposition rates. A widely used technique to accomplish this draws upon a confinement of the charged plasma particles near the target with an additional magnetic field that is provided by a magnetron [24, 69].

When the sputter deposition technique is applied, one has to take into account that the employment of a plasma to bombard the target may lead to various side effects that result from additional interactions of the plasma with the substrate. One of these effects are impacts of plasma particles on the substrate. If the kinetic energy of the particles is high, they may presumably be implanted in the film, lead to a resputtering of the deposited material or create defects in the upper regime of the surface. The KMC model presented in Ref. [34] to study the growth of metallic nanocolumns in a polymer host matrix included none of these processes because it was designed to simulate the deposition by thermal evaporation [30, 65]. As opposed to this, the models presented in this work are intended to represent a sputter deposition process. It is already mentioned that only the last of the mentioned effects—the creation of surface defects—is taken into account by the models described in this work. However, as detailed experimental investigations of those effects are still lacking, those models may already contribute to a better understanding of the plasma–surface interaction.

Treatment of the polymer

So far, we have only been concerned with the deposition of the metallic phase. Depending on the aspired type of the composite, different techniques are used to add the polymeric components to the system. To embed the metal nanoparticles in a host matrix, one usually deposits both metal and polymer at the same time, but from different sources. This technique is called co-deposition. Just like metals, polymers can be sputtered or evaporated, but there also exist other frequently used methods, for example, plasma polymerization [9, 70]. As opposed to co-deposition, a sequential deposition of metal and polymer is carried out if one wants to produce a thin metal film on a polymer substrate. In such a case, spin coating

is another frequently used method to prepare the polymer substrate with high structural uniformity [71].

As the simulation models in this work treat the polymer as a continuous medium, we do not have to work out further details specific to any of those deposition methods. Primarily, it is important that we can assume that the specific choice of the deposition method for the polymer does not introduce additional effects to the simulation models. Hence, we will not have to specify to which method the simulations correspond. We will see that the treatment of surface defects remains on such a general level that it could also include the case that not only the metal but also the polymer is sputter-deposited.

2.1.2. Grazing-incidence small-angle X-ray scattering

Grazing-incidence small-angle X-ray scattering (GISAXS) is a non-destructive *in-situ* technique to characterize the morphology of discontinuous thin film in reciprocal space [72]. The method was introduced by Levine *et al.* for a study of evaporated gold films on glass substrates [73]. In the first part of this section, we will briefly explain the concept of the method and point out some details that will be important for the discussion of the simulations results shown in Chapter 5. At this, we will leave out most mathematical details of the theoretical foundation of the method. After that, we will briefly discuss a formula for the scattering cross section which we will apply to MD simulation results in Sec. 5.5.5. For missing details concerning the experimental procedure and the theoretical foundation of the method, it is referred to the literature, e. g., Refs [72, 74, 75].

Set-up of a GISAXS experiment

In a typical GISAXS experiment, a beam of monochromatic X-rays with wavelength λ is sent towards the surface of the sample under a shallow angle $\alpha_i < 1°$. When the beam reaches the surface, it changes its direction as a result of an elastic scattering process. By measuring the intensity of the scattered X-rays behind the sample in a sufficiently broad range of angles in horizontal and vertical direction, many morphological details of the sample can be inferred. The central quantity for the characterization of the directional dependence of the scattering process is the scattering vector $\mathbf{q} = (q_x, q_y, q_z)$. Assuming conservation of energy, $\mathbf{q}$ can be expressed as the difference of the wavevectors of the scattered beam, $\mathbf{k}_f$, and the incident beam, $\mathbf{k}_i$. If we define the Cartesian reference frame and the relevant angles as shown in Fig. 2.1, the components of $\mathbf{q}$ can be written as

$$\mathbf{q} = \mathbf{k}_f - \mathbf{k}_i = \frac{2\pi}{\lambda} \begin{pmatrix} \cos(\alpha_f)\cos(2\theta_f) - \cos(\alpha_i)\cos(2\theta_i) \\ \cos(\alpha_f)\sin(2\theta_f) - \cos(\alpha_i)\sin(2\theta_i) \\ \sin(\alpha_f) + \sin(\alpha_i) \end{pmatrix} . \tag{2.1}$$

In the following, we will assume that the vector $\mathbf{k}_i$ points in x-direction, i. e., $2\theta_i = 0$. This allows us to simplify the expression for $\mathbf{q}$ to

$$\mathbf{q} = \frac{2\pi}{\lambda} \begin{pmatrix} \cos(\alpha_f)\cos(2\theta_f) - \cos(\alpha_i) \\ \cos(\alpha_f)\sin(2\theta_f) \\ \sin(\alpha_f) + \sin(\alpha_i) \end{pmatrix} . \tag{2.2}$$
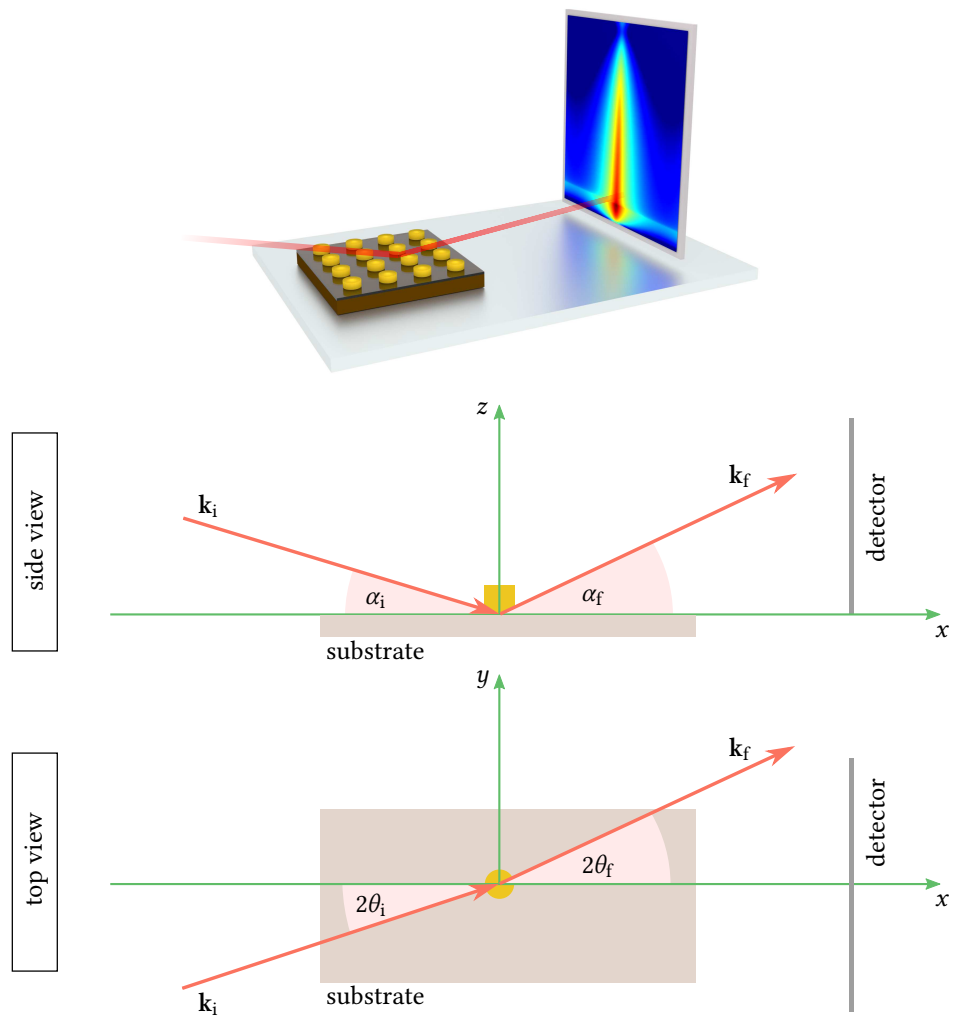
Figure 2.1.: Geometry of a GISAXS experiment according to Ref. [74]. The first row is a rendered image showing a simplified representation of the set-up. In the second and third rows, the angles of the incident wave vector $\mathbf{k}_i$ and the scattered wave vector $\mathbf{k}_f$ are defined.

If only small angles are considered—which is sufficient in typical GISAXS experiments—the trigonometric functions in Eq. (2.2) can be replaced by their respective first-order approximations, and one can assume that $q_x \ll q_y$ and $q_x \ll q_z$ holds [72]. Consequently, one may neglect the forward direction q_x and simply cover all relevant scattering vectors with a two-dimensional detector.

In order obtain a quantitative description of the film morphology from the measured intensity distribution $I(q_x, q_y)$, one can make use of the fact that, for many systems with

a simple geometry, there exist reliable theoretical to make accurate predictions about the scattering cross section that one would measure in a GISAXS experiment. An important step of the procedure is the construction of a hypothetical model system whose associated scattering cross section reproduces the measured scattering cross section as accurately as possible. One usually starts by guessing a simple geometrical shape or a mixture of different shapes that are expected to resemble the shapes of the scattering objects on the surface. Then, one adjusts the dimensions of these objects and their arrangement on the surface until best agreement between the hypothetical and the measured scattering cross section is achieved. This can be done in a fully automatized fit procedure, e. g., with the software programs *IsGISAXS* [74] or *BornAgain* [76]. If good agreement is achieved, one may assume that the geometry of the model system constitutes an accurate approximation of the actual film morphology. Typically, one then takes the sizes, shapes and spatial distributions of the model particles to quantify the experimental results.

Concerning the accuracy of the method, the estimation of the errors may be simplified if real-space images of the investigated samples are available in addition to the GISAXS data. However, in some cases, e. g., when GISAXS is performed during sputter deposition as reported in Refs. [32, 61], one has to interrupt the deposition process to obtain this kind of additional data, e. g., using electron microscopes. Furthermore, even if the scattering cross section of the model system is similar to the measured one, one cannot rule out that there exist other geometrical shapes and arrangements that would yield better agreement. For that reason, experimentalists often use a trial-and-error approach to find the best out of various different shapes. For example, in a comparison of hemispheres, full spheres, cylinders and parallelepipeds in Ref. [32], it turned out that hemispheres are the best representation of gold clusters grown by sputter deposition on a silicon oxide layer.

Calculation of the scattering cross section

In Ref. [74], the expression

$$\frac{\mathrm{d}\sigma}{\mathrm{d}\Omega}(\mathbf{q}) = \frac{1}{N_\mathrm{s}} \sum_{i=1}^{N_\mathrm{s}} \sum_{j=1}^{N_\mathrm{s}} F_i(\mathbf{q}) F_j^*(\mathbf{q}) \exp\left[-\mathrm{i}\mathbf{q} \cdot \left(\mathbf{R}_i - \mathbf{R}_j\right)\right] \tag{2.3}$$

has been derived in kinematic approximation for the differential scattering cross section of N_s scatterers with the spatial coordinates $\mathbf{R}_1, \ldots, \mathbf{R}_{N_\mathrm{s}}$. In the simplest approximation[1], the Born approximation, the factors F_i can be written as the Fourier transform of the shape function S_i of the i-th particle,

$$F_i(\mathbf{q}) = \int S_i(\mathbf{r}) \exp(-\mathrm{i}\mathbf{q} \cdot \mathbf{r}) \, \mathrm{d}^3 r \, . \tag{2.4}$$

The shape function $S_i(\mathbf{r})$ is defined such that it yields 1 if $\mathbf{r}$ is inside the boundaries of the particle and zero otherwise. The quantity F_i is usually called the form factor of a particle; for many simple particle shapes, e. g., spheres, cones and prisms, it can be calculated analytically. Nevertheless, further assumptions about the film morphology are often needed to simplify

---

[1]For many practical applications, a more complex expression obtained with the distorted-wave Born approximation is used. This approximation incorporates reflection-refraction effects at the surface of the substrate [74].

Eq. (2.3). For the evaluation of experimental results, one usually makes guesses about the distributions of particle sizes, shapes and arrangements. With such a statistical description, the discrete expression in Eq. (2.3) turns into a continuous integral for which many further approximations exist [74].

On comparisons with simulations of film formation

The idea of the above discussed GISAXS method is to reconstruct real-space quantities from quantities that are exclusively measured in reciprocal space. If one wants to make a comparison between GISAXS results and simulations results obtained in real space, two different approaches are conceivable: one may not only compare the real-space data, e. g., cluster shapes and sizes, but also try to calculate the scattering cross section from the simulation results which allows for a comparison in reciprocal space. The latter approach is often difficult because the relatively small sizes of the simulated systems do not allow one to obtain the required quantities with reliable statistics. The molecular dynamics results shown in this work thus draw upon a comparison with GISAXS data in real space. Nevertheless, in Sec. 5.5.5, we will also briefly discuss how the form factor—the central quantity for the calculation of the scattering cross section—can be calculated for the simulated clusters.

2.2. Behavior of metal atoms and clusters

In order to simulate the formation of metal–polymer nanocomposites, one first has to describe the system at the basis of a model with reduced complexity. The way metal–polymer nanocomposite are described in this work is largely adopted from the aforementioned work by Rosenthal [9, 48]. Perhaps the strongest simplification in this picture is the treatment of the polymer: this treatment neither takes into account that a multitude of different polymers is deployed for common applications, nor that even one specific polymer may display manifold physical and chemical properties which are strongly sensitive to the conditions of the experimental environment. Instead, the influence of polymers is reduced to setting the conditions for the diffusion of metal atoms and clusters in a continuous medium. Concerning the underlying physical properties of metal–polymer nanocomposites, we will therefore put the focus on the behavior of the metallic components in the system. The following explanations are intended to give an overview of the relevant physical aspects. For additional explanations, it is referred to Refs. [9] and [48], in which a big portion of the simplified picture of metal–polymer nanocomposites has first been developed.

Nucleation and growth of metal clusters

It is a characteristic property of many metal–polymer nanocomposites that the bonding of metal atoms is much stronger than the interaction between metal atoms and the polymer. If this is the case, the metallization of a polymer surface leads to the formation of a discontinuous metal film. The properties of the whole growth process are often subsumed under the term "Volmer–Weber growth" [77].

Initially, the formation of such a film is characterized by a multitude of cluster nucleation events all over the surface. In many cases, clusters consisting of only two metal atoms—so-called dimers—form the smallest stable aggregate [9, 78]. If the interaction with the polymer is sufficiently weak, metal clusters often attain a nearly spherical shape—the energetically favorable configuration. This happens particularly quickly for small clusters because even at room temperature, they are often in the liquid state—a result from a well-known phenomenon known as the melting point depression of metals [39, 79]. To estimate the size of a spherical clusters, the so-called liquid drop model gives sufficiently accurate results for many applications [9, 39, 80]. According to that model, the radius of a cluster containing N atoms of the same species is given by

$$r_{\mathrm{LD}}(N, r_{\mathrm{WS}}) = r_{\mathrm{WS}} N^{1/3} \; , \tag{2.5}$$

where r_{WS} is the Wigner–Seitz radius of the material. This formula is based on the assumption that the cluster has a uniform density of atoms which is the same as the density in the bulk. Hence, each atom in the cluster makes a contribution of $4/3 \pi r_{\mathrm{WS}}^3$ to the total volume of the cluster.

When clusters become larger, they solidify. Even then, they may relax into configurations with a high symmetry, but the process may take a very long time as it is driven by the diffusion of atoms on the cluster surface. Therefore, it is often the case that the complexity of the metallic nanostructures increases with the amount of deposited metal. Two examples of composites with nonspherical metal particles are relevant for this work: the first example is given by the aforementioned work of Schwartzkopf *et al.* [61]. It provides experimental evidence of several different growth modes of gold on polystyrene—starting with the nucleation of small islands and ending with the formation of a percolated network. The growth of metallic nanocolumns observed by Greve *et al.* during co-deposition of Fe–Ni–Co and Teflon AF [30] constitutes the other example. Rosenthal *et al.* have already explained that initially spherical clusters may continue to grow perpendicularly to the polymer surface if their radius exceeds a critical value that marks the transition from a liquid to a solid state [9, 34].

Diffusion of atoms and clusters

The diffusion of metal atoms and clusters during the deposition process greatly affects the microstructure of the resulting composite, in particular at the early stage of the growth [38]. However, while it is already challenging to obtain a correct theoretical description of the diffusion of adatoms on crystalline surfaces [81], the complex diffusive behavior of metal atoms and clusters in the highly complex environment of a polymer may be even more difficult to describe. A particular challenge of experimental investigations is the fact that it is hardly possible to make isolated observations of diffusing particles. For example, during the metallization of a polymer, the diffusion of atoms and clusters is frequently interrupted by aggregation processes; these processes change the sizes of the particles and thus also the speed of the diffusion. The behavior becomes even more complicated if the chemical interaction between the metal and the polymer is strong, but this can mostly be avoided using noble metals.

The difficulty of obtaining appropriate descriptions for simulations lies in the fact that experimental studies of the diffusion in metal–polymer nanocomposites draw upon obser-

vations of macroscopic quantities such as metal concentration profiles [82, 83] or critical island radii [61, 84]; many microscopic details of the involved mechanisms, however, remain unknown [38]. In this work, we thus keep the simple picture established in Refs. [9, 35, 36, 38]: all atoms and clusters in the system perform random walks unless they are trapped at certain points on the surface or in the bulk. The speed of the diffusion depends on the employed materials and two other factors: the size of the diffusing particle and whether it is in the polymer bulk or on the surface. While the diffusion coefficients of individual atoms are often unknown, the laws describing the size dependence of diffusion coefficients are more certain—at least in some cases. For the surface diffusion of clusters containing N atoms, Rosenthal has estimated that the diffusion coefficient scales with N^{-1} [36]. At the same time, a scaling with 2^{-N}, derived from the free volume theory [85–89] has been found appropriate for the bulk diffusion in systems below the glass transition temperature [9, 48]. The difference of these scalings already shows that the diffusion in the bulk is much slower than on the surface. However, the ratio of the surface and the bulk diffusion coefficient of atoms can only be roughly estimated. For example, the simulations presented in Ref. [38] were performed with ratios of 7.5 and 60, but the authors have guessed that the actual ratio should be even higher than 60. As opposed to this, a slightly different ratio of 40 has been proposed in Ref. [9] to describe the occurrence of bimodal cluster size distributions. It is thus clear that the exact ratio remains uncertain in many cases. Here, we will roughly estimate that realistic values are between 10 and 100.

Re-evaporation of metal atoms

When a polymer surface is metallized, only a certain fraction of the arriving metal atoms is actually adsorbed. This fraction, denoted by the condensation coefficient, strongly depends on the employed materials and the temperature [9]. For example, the condensation for silver on Teflon AF at room temperature is only 0.002, but the value for silver on PMDA-ODA polyimide is at least 0.95 [90]. For the modeling of the associated re-evaporation process, it is important that adatoms typically perform a diffusive motion on the polymer surface before they are desorbed [9]. The actual re-emission of the atom happens when the atom is exposed to randomly occurring strong kick of the vibrating polymer chains. According to Ref. [9], re-evaporation primarily affects isolated metal atoms on the surface. Furthermore, it is unlikely that larger clusters do not stick to the surface, and it is almost certain that metal atoms will not be re-emitted if they are deposited on top of an existing cluster.

Defects in the polymer surface

It has already pointed out by others that "point-like" defects in the polymer surface have a big influence on the resulting microstructure of metal–polymer nanocomposites [9, 64]. In some cases, defects are created intentionally, e. g., by a predeposition of a reactive metal or the bombardment with ions [83]. In other cases, however, the defects may result as a side effect of the deposition method; for example, if the composite is prepared by sputter deposition, highly energetic plasma particles may impinge on the surface during the whole deposition process. The rate at which this happens and the energy distribution of impacting

particles are expected to be very sensitive to the plasma parameters and the placement of the substrate with respect to the plasma. To this day, both aspects are largely unknown in the context of metal–polymer nanocomposites. Similarly to what has been mentioned about the diffusion of metal atoms, it is also the case for defects that typical experimental investigations remain on a macroscopic level: it is known that defects in the surface primarily lead to the trapping of metal atoms and clusters [9, 64], but microscopic details are hardly ever described. The treatment of the defects in this work will therefore remain on the level of a simple model: for the KMC simulations, the trapping mechanism described in Refs. [9, 48] is used, see Chapter 4; in the MD simulations, a very similar behavior can be achieved, but the nature of the simulations requires a different implementation, see Chapter 5. The novelty of the approach in this work is that not only preexisting surface defects are studied, but also additional defects that are created during the deposition process. In doing so, an important feature of sputter deposition can be studied—even though many details of the defect creation are still unknown.

Chapter 3

Simulation Methods

The two computational methods used in this work are molecular dynamics (MD) and kinetic Monte Carlo (KMC) simulations. Both methods are known to be suitable for problems on the length and time scales relevant for the formation of metal–polymer nanocomposites (see Fig. 4.1 for an overview), but they have different strengths and weaknesses. As a strongly coarse-grained method, KMC usually provides access to the largest systems and the longest simulation times; however, the method relies on a statistical treatment, which cannot describe certain phenomena, and it often requires rigid approximations. In contrast, MD simulations are considered deterministic (although statistical effects can be incorporated), and their accuracy is usually higher than the accuracy of KMC simulations. For many applications, the biggest drawback of MD simulations is the fact that many processes can only be investigated on time scales which remain far below the experimentally relevant scales. While the benefits from parallel computing are mostly restricted to making large system sizes accessible, there is no such simple and general technique to overcome the time scale issue. Nevertheless, there exists a variety of specific methods to extend the accessible time scales of at least some selected problems.

It is the aim of this chapter to an introduction to both KMC and MD (in particular *atomistic* MD and acceleration techniques). To give an overview, the following aspects remain on a rather general level. Specific details concerning applications of the methods in this work are postponed to later chapters.

3.1. Kinetic Monte Carlo simulations

Since the 1990s, the importance of the KMC method as a tool for coarse-grained simulations in surface science and adjacent fields has rapidly grown [91]. For that reason, there already exist various detailed derivations and reviews of the method, see e. g., Refs. [9, 43, 91–94]. In the following, we will therefore restrict ourselves to recapitulating the idea of the method and skip derivations. In particular, we will describe the algorithm used for the results in this work, make a few remarks on the application of KMC in this work and point out some critical aspects of the methods.
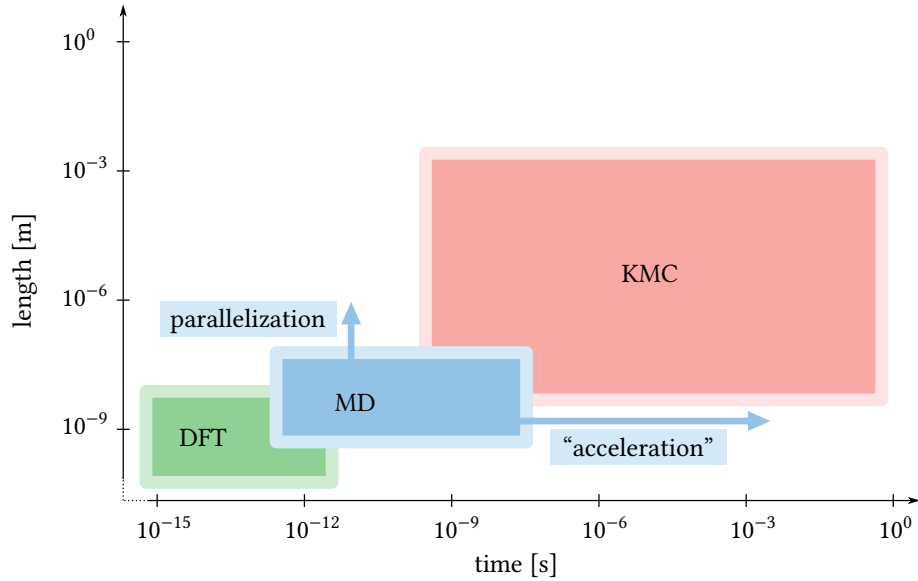
Figure 3.1.: Sketch of typical length and time scales accessible to density functional theory (DFT), molecular dynamics (MD) and kinetic Monte Carlo (KMC) simulation. Of course, the boundaries of the three boxes do not represent hard limits: depending on the employed hardware and the complexity of the considered problem, the scope of the methods may strongly differ from this rough illustration. The two arrows connected to the blue box represent the methods to extend the applicability of MD simulations: parallel computing and specific acceleration methods. The figure has been adapted from a similar figure (without arrows) in Ref. [43].

3.1.1. Idea of the method

To begin with, we make a few restrictions on the systems for which a description with KMC is appropriate. First, we demand that the properties of the system allow us to make the simplifying assumption that there exists only a finite number of system states with indices $1, 2, \ldots, N$[1]. At any point in time, the system may only be in one of these states. All transitions appear instantaneously, and no more than one transition happens at a time. Furthermore, we demand that the dynamics of the system can be described as a Markovian, i. e., "memoryless", stochastic process. That means that the occurrence of transitions between any states can be characterized in terms of probabilities which only depend on the current system state and not on any previous state. For example, a typical application of KMC is the description of surface diffusion in terms of instantaneous hops from one energy basin into another. Such a description may be very useful if the costly calculation of vibrational trajectories around local energy minima do not yield relevant physical information. To illustrate this, a typical trajectory of an atom on a surface—or a similar "energy-barrier-limited infrequent-event

---

[1]We demand this to simplify the notation. In principle, the method can also be applied to an infinite number of states as long as the states and the corresponding transitions are well-defined.
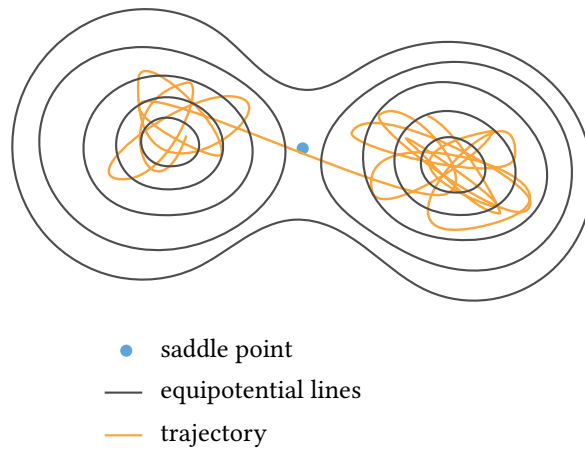
● saddle point
— equipotential lines
— trajectory

Figure 3.2.: Exemplary trajectory of a particle in an infrequent event system. Before a transi-
tion occurs, the particle spends most of the time vibrating around a local energy
minimum. The figure is an adaption of a similar figure in Ref. [94].

system" [94]—is sketched in Fig. 3.2.

In mathematical terms, we demand that the system under consideration can be described
by a set of N master equations

$$\frac{\mathrm{d}P_a(t)}{\mathrm{d}t} = \sum_b \left(W_{ab} P_b(t) - W_{ba} P_a(t) \right) \tag{3.1}$$

which govern the time evolution of the probabilities to find the system in one of the states
$1, 2, \ldots, N$. At that, P_a denotes the probability that the system is in state a at time t, W_{ab} the
transition probability per unit time from state b to state a—which will also be referred to as a
rate in the context of KMC simulations, and $W_{aa} = 0$ is defined for all a. For many practical
applications, analytical solutions of the master equations cannot be obtained. Beyond that, it
is often even impossible to obtain solutions with numerical integration techniques because
the number of system states is too large or the system states cannot be explicitly specified in
advance. For those cases, the KMC method presents an alternative description of the system
dynamics: instead of explicitly solving the master equations, an explicit realization of the
underlying stochastic process is produced by means of a state-to-state trajectory. In many
cases, such a trajectory already reveals important details of the system properties; in other
cases, however, it is necessary to obtain a few or more trajectories and then average over all
results.

In fact, there exist several equivalent algorithms to generate state-to-state trajectories for a
given set of system states and transition rates. One widely used algorithm is the Bortz-Kalos-
Lebowitz (BKL) algorithm [95], which is also frequently referred to as the n-fold way or the
variable step size method [91]. In each Monte Carlo step of this algorithm, one separately
determines from the sampling of two random numbers *when* the next transition happens
and *which* transition actually occurs. A comprehensive derivation of the method based on a

conversion of the differential master equation into an integral equation is given by Jansen in Ref. [91]. Another algorithm also derived by Jansen (and others, e. g., Ref. [9]) is the so-called first reaction method, which was invented by Gillespie [96–98]. The behavior produced by this method is equivalent to the behavior produced by the BKL algorithm, but the procedure during one Monte Carlo step is different: if the system is in a state from which M transitions to other states with rates $W_1, \ldots, W_M$ are possible, one first samples a waiting time Δt_k for each process k from the exponential distribution

$$f(\Delta t_k) = W_k \exp(-W_k \Delta t_k) \,, \tag{3.2}$$

and then carries out the process with the shortest waiting time. As the results presented in Chapter 4 were obtained with the first reaction method, a more detailed presentation of the algorithm is given in the next section.

3.1.2. First reaction method

In the following, we will write down the algorithm of the first reaction method. At that, we keep the algorithm in a general form, which can also be found in the literature, for example, in Refs. [9, 43, 91]. All details specific to the model used for the simulation of the formation of metal–polymer nanocomposites will be given later in Chapter 4.

Initialization

The following steps are required to prepare the simulation.

1. Set the simulation time t to an arbitrary initial value, typically $t = 0$.

2. Set up an initial system state that is in accordance with the initial conditions of the underlying master equation.

3. Prepare a list L in which all possible transitions including their prospective execution times are stored. This list will be updated in each Monte Carlo step.

4. Define a stopping criterion for the simulation.

Monte Carlo step

The following tasks are repeated until the stopping criterion is fulfilled.

1. Find all transitions which are allowed at the current simulation time t and which do not yet exist in the list L.

2. For each found transition, sample a waiting time Δt from the distribution

$$f(\Delta t) = W \exp(-W \Delta t) \,, \tag{3.3}$$

where W is the rate of the transition. Then, insert both the transition and the associated execution time $t + \Delta t$ into L. (For the sake of performance, L should remain in a time-ordered state after each insertion.)

3. Execute the transition with the earliest execution time t' in L and advance the time to t'.

4. Remove all transitions from L which have become obsolete due to the execution of the last transition.

3.1.3. Application of kinetic Monte Carlo simulations in this work

While the standard KMC algorithms are relatively simple to describe, the computational implementation of specific simulation models may be rather elaborate. For many standard models such as atomistic on- and off-lattice models, there exists versatile and freely available software, for example, *SPPARKS*[2] [99] or *KMCLib*[3] [100]. For the problem investigated in this work, however, a code written by Rosenthal was used as it is specialized to simulations of metal–polymer nanocomposite formation and thus required only small modifications. For recent results obtained with that code, it is referred to Refs. [34–36]. A comprehensive description of all details of the implementation can be found in Ref. [9]—in Chapter 4 of this work, only the most important aspects and the modifications made to include the generation of surface defects will be explained.

3.1.4. Critical aspects of the KMC method

The significance of KMC simulations crucially depends on the quality of the underlying model and the accuracy of the transition rates. In the following, we briefly discuss both aspects.

Concerning the transition rates, it is often possible to obtain them from separate calculations on a microscopic level. For example, if the migration pathways are known, one can often calculate the transition rates in the framework of the so-called transition state theory [101, 102] using the formula

$$W = W_0 \exp\left(-\frac{\Delta E}{k_\mathrm{B} T}\right) . \tag{3.4}$$

Here, k_B is the Boltzmann constant and T is the temperature of the system; hence, only ΔE, the energy barrier of the process, and the prefactor W_0 have to be determined, e. g., from DFT calculations. A typical case where this formalism is applied is the treatment of the diffusive motions of adatoms on a metal surface, for example, see the DFT study on the self-diffusion on Au(100) in Ref. [103]. However, there are also cases where the process rates cannot be determined with standard methods—this also applies to many rates that are required for the above mentioned simulation model by Rosenthal. While it is sometimes possible to extract the required rates directly from experimental data, e. g., in the case of deposition rates, in other cases, one has to draw upon guessed values. Nonetheless, even if the values are guessed, one can still obtain reasonable results if the unknown quantities are varied until a specific set of reference data can be reproduced. Such a procedure can be thought of as a best fit: it may yield a correct quantitative description of observed phenomena in a fixed parameter

---

[2]http://spparks.sandia.gov/index.html
[3]https://github.com/leetmaa/KMCLib

regime, but the extension to other parameter regimes may give rise to an incorrect behavior. Comprehensive tests are therefore necessary to assess the quality of the simulations.

While systematic improvements of the process rates are often possible, the establishment of an adequate simulation model may be the more critical aspect of the KMC method. Even if the rates of all implemented processes are known exactly, it is often difficult to rule out that the underlying model is too coarse or that the model still lacks important processes. For example, in Ref. [94], Voter mentions that the exchange mechanism of an adatom on an fcc(100) surface has been unknown for a long time although it may be crucial to describe the surface diffusion of certain materials. Nevertheless, many KMC models are based on heuristic descriptions of highly complex systems. Although there exist microscopic methods that help to discover initially unknown processes and their reaction paths, see e. g., Refs. [55, 104], it often remains impossible to examine the quality of the simulation model without extensive testing against experimental reference data.

3.2. Molecular dynamics simulations

Since its invention by Alder and Wainwright in the 1950s [105, 106], the MD method has become an extensively used tool to study the time evolution of many-body systems in various areas of computational research. In this section, we recapitulate the basics of atomistic MD including common approaches to accelerate the dynamics, and we focus on the details required for this work. Further aspects of the methodology that are skipped in this presentation can be found in Refs. [41, 107, 108]. For another recent overview, including the specific aspect of plasma–surface interaction, it is also referred to Ref. [50].

3.2.1. Introduction

The general aim of the MD method is to provide numerical solutions $\{\mathbf{r}_i(t) \mid i = 1, \ldots, N\}$ of the Newtonian equations of motion

$$m_i \frac{\mathrm{d}^2 \mathbf{r}_i(t)}{\mathrm{d}t^2} = \mathbf{F}_i \qquad (i = 1, \ldots, N) \tag{3.5}$$

for N pointlike particles with masses m_i. The terms $\mathbf{F}_i$ represent the forces that characterize the system under consideration; they may be obtained from a classical force field—as in classical MD—or from electronic structure calculations—as in *ab inito* MD [50]. Furthermore, if it is necessary to describe the system, $\mathbf{F}_i$ may also contain arbitrary other external forces.

In this work, we are concerned with MD simulations of entire atoms, i. e., each particle represents both the nucleus and the electrons. This level of description allows us to simulate sufficiently large systems and achieve sufficiently long simulation times. Performing atomistic MD, interatomic interactions resulting from the interplay of electrons (and nuclei) are usually treated on the basis of coarse-grained models which yield classical force fields for the problem of interest. The development of force fields for various kinds of problems is a large field of research in itself. In fact, as the forces are of crucial importance to MD simulations, there exist force fields for numerous materials and their combinations in all kinds of scenarios; furthermore, it is even possible to model chemical reactions even though electrons are not

explicitly taken into account. For an overview of different force fields and their applications, it is referred to the literature, for example Refs. [109–113]. Here, in Sec. 3.2.3, we will only discuss one type of force field that was used for the treatment of metal atoms in the simulations for this work: the underlying formalism is the so-called embedded-atom method.

3.2.2. Langevin dynamics

For many applications, it is required to control the system temperature T in order to approximate a canonical ensemble. For this task, there exist several standard algorithms—called thermostats [41]—for example, the Nosé–Hoover thermostat [114, 115], the Berendsen thermostat [116] and Langevin dynamics [117]. The simulations for this work were performed with Langevin dynamics because the underlying model, the interaction of the particles with an implicit solvent, is useful to describe the motion of metal atoms in and on a polymeric background medium. Details of the specific implementation of the thermostat can be found in Refs. [118] and [119].

The Langevin equation of motion for the i-th particle reads

$$m_i \frac{\mathrm{d}^2 \mathbf{r}_i(t)}{\mathrm{d}t^2} = \mathbf{F}_i - \frac{m_i}{\tau} \dot{\mathbf{r}}_i + \sqrt{\frac{2 m_i k_\mathrm{B} T}{\tau}} \mathbf{R}_i \, , \tag{3.6}$$

where τ is a damping parameter and $\mathbf{R}_i$ is an uncorrelated Gaussian process with zero-mean [41, 120]. This equation is essentially a reproduction of Eq. (3.5), but with two additional terms on the right-hand side; these terms represent a friction force and a stochastic force resulting from collisions with the background medium. The damping parameter τ should be adjusted to material-specific conditions; it roughly indicates the time it takes for the system temperature to relax to the value T.

In the absence of interparticle forces, the Langevin equation describes a random walk. For one particle with mass m and a d-dimensional position vector $\mathbf{r}$, the Langevin equation reads

$$m\ddot{\mathbf{r}} = -\frac{m}{\tau} \dot{\mathbf{r}} + \sqrt{\frac{2 m k_\mathrm{B} T}{\tau}} \mathbf{R} \, . \tag{3.7}$$

The resulting motion can be characterized by the mean squared displacement

$$[\mathbf{r}(t) - \mathbf{r}(0)]^2 = 2dDt \tag{3.8}$$

with the diffusion coefficient [120]

$$D = \frac{k_\mathrm{B} T \tau}{m} \, . \tag{3.9}$$

In Secs. 5.2 and 5.3, we will need these relations to calculate the diffusion coefficients of isolated metal atoms.

3.2.3. Embedded-atom method

Ever since its invention by Daw and Baskes in the 1980s [121, 122], the embedded-atom method (EAM) has become a widely used approach to describe the interaction of metals and

alloys in MD simulations [110, 123]. The functional form of the total potential energy U of N atoms reads

$$U = \frac{1}{2} \sum_{i=1}^{N} \sum_{\substack{j=1 \\ j \neq i}}^{N} \phi_{X(i)X(j)}(r_{ij}) + \sum_{i=1}^{N} F_{X(i)}(\overline{\rho}_i) \, . \tag{3.10}$$

Here, the subscript $X(i)$ denotes the atom species of the i-th atom, i. e., Eq. (3.10) can be used for any mono- or multimetallic system. The first term on the right-hand side represents electrostatic contributions associated to each pair of atoms i and j at the distance $r_{ij} = |\mathbf{r}_i - \mathbf{r}_j|$. The second term is a sum over the so-called embedding functions. These functions, labeled $F_{X(i)}(\overline{\rho}_i)$, denote the amount of energy it takes to place an atom belonging to $X(i)$ at the position $\mathbf{r}_i$, where it is exposed to the local electronic density $\overline{\rho}_i$ resulting from the presence of all surrounding atoms. One of the critical assumptions of the method is that each surrounding atom j makes makes an independent contribution that solely depends on the distance r_{ij}; the resulting density is thus calculated as the superposition

$$\overline{\rho}_i = \sum_{\substack{j=1 \\ j \neq i}}^{N} \rho_{X(j)}(r_{ij}) \, . \tag{3.11}$$

An improvement of this concept is, for example, provided by the modified embedded-atom method (MEAM), which introduces an additional angular dependence of the functions $\rho_{X(j)}$ [110, 124].

In order to represent specific materials, one first has to specify explicit expressions for the embedding function, the electronic density function and the pairwise interaction function. For a monometallic material, these are three functions in total; in contrast, seven functions are required for a combination of two materials A and B, namely F_A, F_B, ρ_A, ρ_B, ϕ_{AA}, ϕ_{BB} and ϕ_{AB}. To obtain the functions for specific materials, one usually makes an ansatz for the functional form first, and then fixes the parameters such that selected reference data can be reproduced. Typical reference quantities are characteristic properties of the bulk system, for example, equilibrium lattice constants, elastic constants and vacancy-formation energies [125].

The simulations for this work were carried out for a system containing only gold atoms and another system containing both silver and copper atoms. All employed EAM potentials are standard potentials which are widely used for the description of solids, surfaces and clusters—their references will be given in the respective chapters. As most EAM potentials are, per design, best suited for large systems, one should bear in mind that the description of small clusters is often inaccurate. This becomes less problematic as clusters increase in size. It is expected that the errors due to the limited accuracy of the EAM potentials used in this work are far below other possible errors. Therefore, it was refrained from employing more accurate, but computationally more expensive potentials. Nevertheless, the employment of other force fields is a straightforward task, which can be done without further modifications of the simulation scheme.

Lastly, it is mentioned that most available EAM potentials are usually short-range. Therefore, they are usually equipped with a cut-off radius which puts a limit on the maximum

interatomic distance for which a finite contribution to the potential energy is made. The employment of a cut-off radius has an important effect on the time to calculate the forces: as every atom typically has a limited amount of neighbors within the cut-off radius, the computation time scales with $O(N)$, as opposed to the quadratic scaling for systems with long-range potentials such as Coulomb interaction [126].

3.2.4. Numerical integration and acceleration methods

There exists a variety of standard methods for the numerical integration of the equations of motion. The method used in this work is the velocity version velocity version of the Verlet integration [127, 128]; it is frequently used by others, too, because of its stability and its performance with respect to conservation of energy [108]. The choice of the time step used for the integration must be sufficiently small to capture the dynamics of the fastest processes in the system. In many problems of surface science and materials science, these fastest processes are the elementary vibrations of the atoms in the considered solid. Therefore, typical values of the time step used for these problems are on the order of 0.1 fs to 2 fs [50, 54, 129]. In the remainder of this section, we will not only see that such a small size of the time step is a problem for many practical applications, we will also get an overview of common approaches to solve this problem.

The time scale problem and the role of hardware

It has often been discussed in the literature that the time scales accessible to standard MD simulations are insufficient to describe many relevant phenomena in solids or on surfaces [50, 55, 130]. This holds, in particular, for thin-film deposition processes as sufficiently long studies should cover seconds or minutes observe successive deposition events and the diffusion processes in the time between [34, 99]. As a rule of thumb, the authors of Ref. [50] have pointed out that most MD simulations running on modern hardware do not exceed time scales of nanoseconds—only for selected problems, it is also possible to reach microseconds. Here, we merely illustrate the resulting time scale problem with a simple example.

In an MD simulation of a freely vibrating gold dimer—a very small system, an average of 1.2×10^6 integration steps per second was achieved on one modern CPU core. As the employed time step had a value of 1 fs, it would take a computation time of roughly 25 years to obtain the trajectory for one second. It is not necessary to discuss further details of the employed hardware and the computational procedure—we can already see that simulation times on the order of seconds are far out of reach of typical atomistic simulations. Even parallelization techniques could not help to achieve a significant reduction of the computation time because the amount of parallelizable computations is small in this example. Instead, the benefits from parallelization are rather attributed to the possibility to study similar but larger systems in nearly the same amount of time. Despite these limitations, several approaches—often called "acceleration methods"—have been developed to overcome the time scale problem in MD simulations. As the application of the MD simulation scheme presented in Chapter 5 of this work may result in an effective acceleration of the simulation time, too, we will proceed by discussing some of the most relevant acceleration techniques to put this

work in a context.

Acceleration methods

We will concentrate on four methods which frequently occur in the literature. For the sake of brevity, we will only mention their basic ideas; for a broader overview, it is referred to Refs. [50, 51, 55, 130]. The first three methods presented hereinafter have been developed by Voter and co-workers to make transitions in infrequent event system occur more frequently while maintaining the correct statistical weights of all possible transitions [51, 55]. In a sense, they are based on similar principles as the KMC method, but the knowledge of possible states and transitions is not required in advance. The fourth presented method has recently been reported by Filinov *et al.* This approach is based on a formulation of rate equations whose parameters are extracted from MD simulations.

Hyperdynamics.   The hyperdynamics approach, which was first presented in Ref. [131], can be applied to systems whose transitions obey the previously mentioned transition state theory (TST) [101, 102]. It works be employing a biased potential energy landscape

$$U'(\mathbf{r}) = U(\mathbf{r}) + \Delta U(\mathbf{r}) \tag{3.12}$$

to reduce the energy barriers associated to transitions between adjacent states. The bias $\Delta U(\mathbf{r})$ must be non-negative and sufficiently small to ensure that the biased system still obeys TST. Furthermore, it must be chosen such that it vanishes at all dividing surfaces and such that the ratios of the resulting transition rates are the same as in the unbiased system. In doing so, the state-to-state dynamics of the system will be the same as in the unbiased system, but the waiting times between transitions can be strongly reduced.

The main difficulty of the method lies in the construction of an appropriate bias potential because this task already requires a certain knowledge of expected transitions. In the first study of hyperdynamics in Ref. [131], ΔU was constructed from a Hessian matrix. Thereby, the diffusion of an Ag_{10} cluster on an $Ag(111)$ surface was accelerated by a factor of 8×10^{-3}. However, ever since then much higher boost factors have been achieved using other approaches. For example, Fichthorn *et al.* constructed ΔU from the nearest-neighbor bond lengths in a solid and achieved boost factors of up to 10^6 for the diffusion of Cu atoms on a $Cu(001)$ surface [132]. For the same system, even higher boost factors of 10^9 were reached with the collective-variable hyperdynamics (CVHD) method recently developed by Bal and Neyts [54]. The CVHD method draws upon combining hyperdynamics with metadynamics [133, 134] to incrementally build up a bias potential that only depends on one collective variable. This rather general concept lends the method a high flexibility; for example, CVHD has also been applied to the folding of a polymer chain model [54] and fuel combustion mechanisms [135].

Temperature accelerated dynamics.   Using temperature accelerated dynamics (TAD), first introduced in Ref. [136], one tries to exploit that transitions occur more frequently if the simulations are performed at an elevated temperature. However, as raising the temperature

alone would lead to a corrupt state-to-state dynamics, an additional mechanism is applied to revoke each transition from a local energy minimum until a sufficiently long list of escape paths and times has been collected. The escape times in this list are extrapolated to lower temperatures, and the event associated to the earliest escape time is actually carried out.

As opposed to hyperdynamics, TAD is more restrictive because it requires the system to satisfy the harmonic version of TST. Nevertheless, it can be very effective: for example, is has been reported in Ref. [55] that a simulation of the growth of a Cu(100) surface at a temperature of 77 K was accelerated by a factor of 10^7.

Parallel replica dynamics.   We mentioned above that parallelization techniques are mainly used to increase the accessible system sizes. Nevertheless, for infrequent event system with exponentially distributed first-escape times of all occurring processes, a method called parallel replica dynamics (ParRep) also allows one to extend the accessible time scales [137, 138]. Using ParRep, the reduction of the computation time is realized as follows: first, one produces dephased copies of the system on each available processor; then each system independently evolves in time until a transition from the initial state A to another state B occurs on one processor. Next, the system clock is set to the sum of the simulation times on all processors, and the procedure is repeated starting from state B.

As the boost factors achievable with ParRep are limited by the number of parallel computing devices, ParRep presently cannot surpass the efficiency of TAD and hyperdynamics. Nevertheless, it is a less restrictive and simple-to-implement method, and it is advantageous that the efficiency of the method can be improved without any theoretical effort. Furthermore, under certain circumstances, it is possible to combine ParRep with other acceleration methods.

Coupling of MD and rate equations for atom adsorption.   Another recently presented approach builds on combining MD simulations with a rate equation model [52, 53]. This method, named MD-RE by the inventors, was specifically developed to study the the adsorption and desorption of rare gas atoms on metal surfaces. The authors of Refs. [52, 53] showed that these processes can be fully described in terms of rate equations for the populations of three characteristic states: the projectile may be either trapped, quasi-trapped or in a scattering state. Furthermore, the authors showed that the transition probabilities required by the rate equations can be accurately determined from atomistic MD simulations. Hence, MD-RE provides an acceleration in the sense that a solution of the rate equations may be used to extend the MD results to macroscopic time scales.

3.2.5. Application of molecular dynamics in this work

In this section, we have introduced the basic concepts of the MD simulations used in this work. However, the specific application to the growth of metal clusters on a polymer surface requires us to elaborate many further details; as this section was intended to give an overview, we will do this later in Chapter 5. In particular, we will also give a detailed explanation of the method used in this work to reach long time scales.

Here, we conclude by mentioning that all MD simulations of this work were carried out with the software *LAMMPS*, a publicly available MD program distributed by Sandia National

Laboratories [139]. *LAMMPS* provides the basic functionality to carry out many standard tasks in typical atomistic MD simulations. In fact, all steps described in Chapter 5 could be realized with solely built-in features. For the evaluation and visualization of the atomistic simulation data, both self-written scripts and the software *OVITO* [140] were used.

Chapter 4

Growth of Metallic Nanocolumns in a Polymer Matrix

In this chapter, we apply the KMC method to simulate the growth of metallic nanocolumns during co-deposition of metal and polymer. As mentioned before, this investigation is an extension of the previous work performed by Rosenthal *et al.* [9, 34]. We will use their simulation model and modify it so that we can investigate how the columnar growth is influenced by bulk diffusion and the creation of surface defects during deposition.

In Sec. 2.2, we have already explained that the onset of nanocolumnar growth is assumed to be associated to the solidification of initially spherical clusters, which sets in when the clusters reach a critical size. Such a critical size can only be reached by the clusters if the ratio κ of the metal and the polymer deposition rate is sufficiently large. In the simulations by Rosenthal and the preceding experiments described in Ref. [30], it was shown that it only takes a small increase of κ to modify the system such that it contains a large amount of columns instead of only spherical clusters. It has been found that the onset of nanocolumnar growth leads to a characteristic behavior of the volume filling factor f, the ratio of the volume of the deposited metal and the total volume of the composite, expressed as a function of κ: for small ratios κ, the metal clusters remain spherical and the filling factors are relatively small. However, once κ reaches a critical value, many of the spherical clusters turn into columns, and the filling factor steeply increases. This happens in a relatively small regime of intermediate κ-values; for larger values, the increase rapidly levels off. Many of the results shown in this chapter will display exactly this behavior. Yet, we will see that it is greatly affected by the occurrence of surface defects as well as a variety of other conditions.

In Sec. 4.1, we start by explaining the underlying simulation model. The presentation contains as many details as are believed to be required for the understanding of this work. A more comprehensive explanation referring the original model is given in Refs. [9, 34, 48]. In Sec. 4.2, we study the influence of defects by analyzing KMC simulation results which were performed under various different conditions.
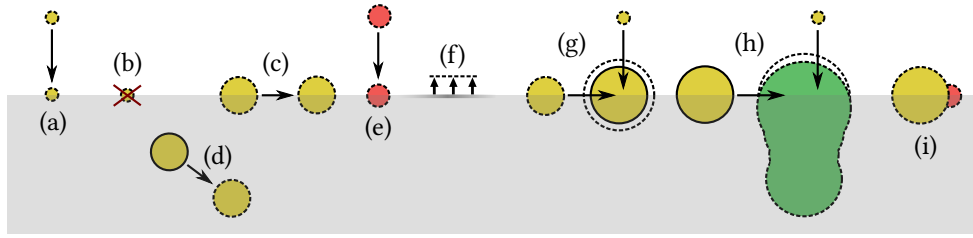
Figure 4.1.: Side-view illustration of the KMC simulation model: creation of an atom on the polymer surface (a), removal of an atom due to re-evaporation (b), jumps of a cluster (or an atom) on the surface (c) and in the bulk of the polymer (d), creation of a surface defect (e), shift of the surface due to deposition (f), coalescence of two clusters and attachment of a deposited atom to a cluster (g), attachment of a cluster or a deposited atom to a column (h), and trapping of a cluster at a defect site (i). Adapted from [141].

4.1. Description of the model system

In the following, we will recapitulate the most important details of the KMC simulation model by Rosenthal *et al.* and explain all modifications that were made for the simulations in this work. Concentrating on the model, we will skip any details on the specific implementation of the first reaction method; these rather technical aspects can be found in Refs. [9, 48].

Before we proceed, it is referred Fig. 4.1 which provides a graphical illustration of the processes discussed in the following. Furthermore, it is already remarked that in same sentences in this chapter, the word "cluster" not only refers to actual clusters, but also to atoms. In that sense, an atom can be understood as a cluster of size one.

4.1.1. Components of the model and growth

Simulation box and treatment of the polymer

The KMC simulations are performed with a rectangular simulation box which represents the polymer matrix on which (and in which) the metal particles move and grow. The polymer is hence treated implicitly: it provides a continuous and homogeneous space and the boundaries for the metal atoms and clusters, but it does not directly affect their motion. Accordingly, we can understand the plane at the top of the simulation box as the surface of the system and the space in the box as the polymer bulk including metallic filler particles. In the following, we will use the set

$$\left\{(x, y, z) \mid 0 \leq x \leq L_x,\ 0 \leq y \leq L_y,\ 0 \leq z \leq L_z\right\} \tag{4.1}$$

to formally describe all points comprised by the simulation box. The dimensions L_x and L_y of the box in x- and y-direction, i. e., parallel to the surface, cannot change while the simulation is running. To reduce edge effects and thereby approximate a larger system, periodic boundary
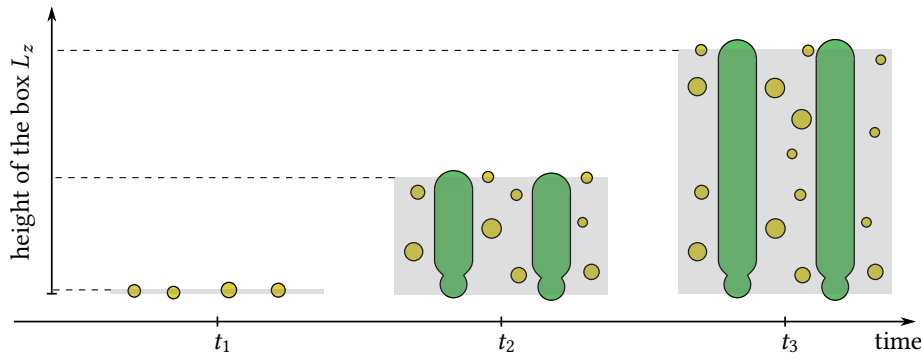
Figure 4.2.: Illustration of the distribution of spherical clusters (yellow) and nanocolumns (green) in the polymer host matrix (gray) at three different times during one simulation. The upper part of the gray area represents the surface and marks the upper boundaries of the simulation box.

conditions are applied to the x- and y-direction.evtl unten The height of the simulation box, L_z, represents the thickness of the deposited film. Its value is time-dependent and starts with $L_z = 0$ at the beginning of the simulation. The following two mechanisms lead to a shift of the surface height:

- Whenever a Monte Carlo step is performed, it is assumed that the amount of the polymer deposited during the time Δt between the current step and the previous step leads to the shift $\Delta L_z = R_\mathrm{p} \cdot \Delta t$, where R_p is the deposition rate of the polymer with the dimension [length] $\cdot$ [time]$^{-1}$.

- Whenever a metal atom is deposited, the surface height is shifted by an effective thickness $\Delta L_z = \delta_\mathrm{atom}$, which corresponds to the thickness of a thin layer with the volume of one metal atom, V_atom. It can thus be calculated by $\delta_\mathrm{atom} = V_\mathrm{atom}/(L_x L_y)$. In the same way, L_z is reduced by the same amount δ_atom whenever an atom is removed from the surface in the course of a re-evaporation event (see below).valueofV

As the KMC algorithm leads to randomly occurring deposition and re-evaporation events, the surface height is a unique non-monotonic function of time in each simulation run. An illustration of the expanding simulation box is given in Fig. 4.2.

Discrete components: atoms, clusters and columns

In contrast to the polymer, a discrete particle model is employed for the metallic component. In this model, single metal atoms are represented by spheres whose radius is equal to the Wigner-Seitz radius of the simulated material. However, atoms are only resolved as long as they freely diffuse in or on the polymer matrix. All agglomerates consisting of two or more metal atoms are described as a single object with either a perfect spherical shape or a columnar shape. The spherical cluster model is a realization of the liquid drop model which

has already been presented in Sec. 2.2. Although the reference experiment by Greve *et al.* [30] was performed with iron, nickel and cobalt, the model is based on a simplified and generic description with a monometallic material. The Wigner–Seitz radius used for the liquid drop model of clusters and atoms (see Eq. (2.5)) is set to $r_{WS} = 0.145$ nm. This roughly approximates the values for iron, nickel and cobalt, which are in between 0.144 nm and 0.147 nm [142].

As we will see later, for the assignment of certain processes, it is necessary to distinguish between particles on the surface and particles in the bulk. This is realized by calculating the difference of the surface height L_z and the z-coordinate of the center of the particle under consideration. The algorithm defines a particle to be on the surface if $L_z - z$ is less than its radius—otherwise, it is in the bulk.

Growth of spherical clusters and columns

All growth events appear as instantaneous updates of the system configuration whenever pre-defined criteria of their executions are met. Hence, unlike events such as jumps or depositions of atoms, the growth is *not* controlled via reaction rates, but it happens when the system is updated after Monte Carlo steps. In the following, the rules of two implemented growth modes—spherical and columnar—are specified.

If the distance between two spherical clusters of sizes N and M (atoms are included for $N, M = 1$) falls below a pre-defined interaction length, the clusters are merged into a new single object. This process represents the coalescence of clusters. If the sum $N + M$ is below a critical size, the newly formed object is again a spherical cluster whose radius $r_{LD}(N + M, r_{WS})$ is calculated according to Eq. (2.5). The center of mass of the new cluster is set to the center of mass of the cluster which has moved in the last Monte Carlo step. When more than two clusters agglomerate in one step, all pairs of interacting clusters are successively merged until only one cluster remains.

If the radius of a spherical cluster becomes larger than a pre-defined critical radius r_{crit}, the object will be treated as a nanocolumn in the remaining time of the simulation. That means that it no longer maintains its spherical shape during growth, but instead expands in the direction perpendicular to the surface. The nanocolumnar growth mechanism follows a simple geometrical model based on the idea that the attachment of clusters or atoms to the column only affects the part of the column above the surface (and not the whole object as is the case of spherical clusters). While a comprehensive description of the columnar growth model can be found in the original works by Rosenthal [9, 34], here, we restrict ourselves to an explanation of the basic ideas. A graphical illustration of these aspects can be found in Fig. 4.3.

When the columnar growth mode is initiated, the growing particle still has the shape of a sphere. Its part over the surface is therefore a spherical cap. At the next growth event, this spherical cap is replaced by a another spherical cap cut off from a larger sphere. The atom or cluster that has been attached during this Monte Carlo step is then removed from the simulation. The size of the new spherical cap is determined according to the following rules.

- The volume of the new spherical cap is the sum of the volume of the previous spherical cap and the volume of the attached atom or cluster. Assuming that no atoms are lost during the process, that means that the density of the metallic material is conserved.
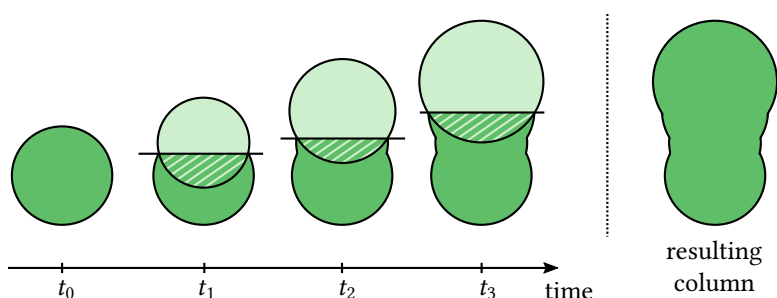
Figure 4.3.: Side-view illustration of the nanocolumnar growth model employing a stacking of spherical caps. The seed of a column—an initially spherical cluster—is shown at time t_0. The respective changes induced by three growth events are shown at times t_1, t_2 and t_3. The horizontal lines indicate the surface height at the times of the growth events. On the right, only the contour of the resulting column is shown.

- The area of intersection between the spherical cap and the plane representing the surface remains unchanged during the replacement of the spherical cap. That means that the vertical position of the sphere from which the new spherical cap is cut off must be shifted from the position of the original spherical cluster.

As the top of the nanocolumn maintains the shape of a spherical cap, all subsequent growth events can be handled in the same manner. As the surface height is permanently shifted, this procedure creates a stack of many thin sphere segments with spherical caps at the top and at the bottom. The morphological details of the column are hence determined by the different sizes and shapes of the sphere segments. In practice, a nanocolumn with a length of 100 nm often consists of several hundreds or thousands of segments. The column radius becomes nearly constant if there are only weak fluctuations of the particle flux towards the column.

4.1.2. Processes

Having addressed the components of the model in the previous section, we now turn towards the processes that drive the time-evolution of the system configuration: deposition of particles, jumps of atoms and clusters on the surface and in the bulk, creation of surface defects, and re-evaporation of atoms. In the following, it is explained how these processes are incorporated into the simulation model and how the corresponding rates are determined.

Deposition of atoms

The simulation model includes two processes which represent the deposition of metal and polymer. As the treatment of the polymer has already been explained in Sec. 4.1.1, we now address a process that represents the deposition of metal by successively adding particles to the system. At each deposition event, one spherical particle is created at a random position at

the surface, i. e., at the top of the simulation box. At this, the center of mass of the particle is aligned with the current surface height. If the sampled position of the deposited particle lies within the interaction range of any already existing particle, a growth event immediately follows the deposition. Otherwise, the particle will perform a diffusive motion according to the process described in the next section. In either case, the deposition of a metal atom is always followed by a shift of the surface, as explained in Sec. 4.1.1, too.

As is typical of sputter deposition, only atoms are deposited in the simulations.[1] In the following, we assume that the deposition of the metallic components is intended to be carried out with the constant rate R_{m}. Beyond that, we also assume that R_{m} denotes the effective film thickness deposited per unit time, which is a typical way of expressing the deposition rate in experimental works. For the simulations, however, it is required to obtain a rate for the addition of atoms on a surface with the area $L_x L_y$. This rate, labeled v_{m}, can be obtained from the conversion

$$v_{\mathrm{m}} = R_{\mathrm{m}} L_x L_y \rho_{\mathrm{m}} \, , \tag{4.2}$$

where ρ_{m} is the number density (number of atoms per volume) of the deposited material. Instead of referring to v_{m}, we will later consider an equivalent quantity, the flux of atoms towards the surface, J_{m}. It can be obtained by

$$J_{\mathrm{m}} = \frac{v_{\mathrm{m}}}{L_x L_y} \, . \tag{4.3}$$

Surface and bulk jumps

The diffusion of atoms and clusters is modeled by creating a sequence of jump events which translate the position of a particle to a point at the distance $l_{\mathrm{jump}} = 0.6\,\mathrm{nm}$ from the original position. The value of l_{jump} has been chosen such that it approximates the diameter of a polycarbonate chain [9], but it can be understood as a free parameter. The direction of the jump is sampled right before the jump event is carried out. To model the different characteristics of the diffusion of particles on the surface and particles in the bulk, two processes different processes have been implemented—we will call these "surface jumps" and "bulk jumps". Both processes differ in their ranges of allowed jump directions and the way the associated rates are calculated.

A bulk jump moves a particle to a randomly sampled point $(\tilde{x}, \tilde{y}, \tilde{z})$ on the three-dimensional sphere with the radius l_{jump} around the current position of the particle. All points on this sphere have equal sampling probabilities. If the sampled point is above the surface, the third coordinate of the new point is set to L_z. If the sampled point is below the bottom face of the simulation box, i. e., $\tilde{z} < 0$, the third coordinate is set to $-\tilde{z}$. In contrast to bulk jumps, surface jumps leave the vertical coordinate of the particle unchanged. That means that the new coordinates $(\tilde{x}, \tilde{y})$ are picked from a circle around the current position whose radius vector with the length l_{jump} is parallel to the surface. While bulk jumps may be performed by both particles on the surface and particles in the bulk, surface jumps may only be performed by particles on the surface.

---

[1] For other purposes, the functionality to employ any other size distribution for the deposited particles was implemented to the simulation program by Nuttawut Kongsuwan during his RISE internship in summer 2014.

Per definition, every particle is on the surface right after its deposition event. As surface jump rates are usually higher than bulk jump rates, many particles on the surface perform a relatively long two-dimensional random walk before a bulk jump or a shift of the surface makes them enter the bulk for the first time. Once a particle is in the bulk, it does not have to stay there forever: if it comes close enough to the surface, it will be considered as a surface atom again.

Surface and bulk diffusion coefficients

For random walks in a d-dimensional space with the jump length l_{jump}, the relation between the diffusion coefficient D and the jump rate v is known to be [9]

$$D = \frac{l_{\text{jump}}^2 v}{2d} \ .$$
(4.4)

Hence, it is possible to adjust the rates of the surface and bulk jumps such that specific systems with known diffusion coefficients are represented. However, separate and accurate measurements of the bulk and the surface diffusion coefficient can hardly be found in the literature on metal–polymer nanocomposites. This work therefore pursues the approach by Rosenthal *et al.* which relies on estimated values of the diffusion coefficients of atoms and postulated laws for the size dependence of the diffusion coefficients of clusters [9, 36].

For the calculation of the bulk diffusion coefficient D_N^{b} of a cluster containing N atoms, the formula

$$D_N^{\text{b}} = 2^{-N} D_1^{\text{b}}$$
(4.5)

is used. At this, D_1^{b} is an estimated value of the bulk diffusion coefficient of an atom. The functional form of Eq. (4.5)—an exponential decay with the cluster size N—was proposed for systems below the glass transition temperature. As mentioned before, the theoretical basis of this can be found in the aforementioned free volume theory [85–89]. For the surface diffusion coefficient, Rosenthal *et al.* propose the size dependence

$$D_N^{\text{s}} = N^{-1} D_1^{\text{s}} \ ,$$
(4.6)

where D_1^{s} is the surface diffusion coefficient of an atom.

Re-evaporation of atoms

To represent incomplete condensation, the simulation scheme contains a process to remove atoms from the system. This is only possible for atoms which are considered to be on the surface (according to the definition above) and not trapped. A re-evaporation event is realized by an instantaneous deletion of the particle at its current position. For each atom that comes into question for a deletion, the corresponding process time is sampled with the rate v_{re}. As material-specific values of v_{re} are not known, it is treated as a free parameter. However, knowing that an atom typically makes several jumps before it is re-emitted [9, 143], it is reasonable to assume that the re-evaporation rate is smaller than the surface jump rate of an atom. In the following, we will therefore express v_{re} as

$$v_{\text{re}} = \lambda_{\text{re}} v_1^{\text{s}} \ .$$
(4.7)

where λ_{re} is a scale factor that is typically less than one, and ν_1^s is the surface jump rate of atoms that be obtained from Eq. (4.4). If one wants to make a systematic study of the effects resulting from an incomplete condensation, the simulations should be performed with many different values of λ_{re}.

Trapping at defects

A defect in the polymer structure is represented by a three-dimensional sphere whose radius is a free parameter. The position of a defect cannot change during the simulation. Once a defect and a metal particle intersect each other, the metal particle is considered as trapped and it becomes immobile for the rest of the simulation run. That means that it cannot perform surface or bulk jumps, but it can still coalesce with other particles. If the trapped particle is an atom, the trapping has the additional effect that it prevents the atom from re-evaporating.

The old simulation model already offered the possibility to create an initial distribution of defects in the plane at $z = 0$. This distribution could be defined by choosing the areal number density of the defects, ρ, and a pattern for the arrangement of the defects, e. g., random or hexagonal. To account for the impingement of highly energetic particles during sputter deposition, this functionality has been extended to allow for the creation of new defects during the whole deposition process. For that purpose, a new random process has been implemented which creates defects at random places in the plane at the height of the current surface. At this, it is not checked whether this space is already covered by another defect or metal particle. It is thus possible that the creation of a defect immediately leads to the trapping of an existing particle.

Due to the simplicity of the model for the defects, it is difficult to find a correspondence between the specific values of the defect creation rate, labeled J_d, and the conditions of an actual experiment (e. g., plasma parameters). We therefore introduce another free parameter,

$$\gamma = \frac{J_d}{J_m} \; , \tag{4.8}$$

which must be varied to study the influence of the defects. Again, instead of making a direct guess for the unknown parameter, it is related to another known parameter—in this case, it is assumed that the amount of deposited atoms is much higher than the amount of created defects, i. e., γ should be much less than one.

Trapping at columns

When both clusters and columns co-exist in the system, a cluster may not only encounter the top of a column on the surface, but also any part of the column in the bulk. The previously described columnar growth events are only carried out in the former case. In the latter case, the concerned cluster becomes immobile for the rest of the simulation run. This behavior is intended to reflect the assumption that the structural relaxation of large objects is hampered in the bulk.

4.2. Simulation results

In this section, we study how the generation of surface defects influences the growth of nanocolumns. For that purpose, we make a comprehensive analysis of simulation results obtained with the present KMC model. In Sec. 4.2.1, we start with some general remarks on the simulations. Then, we turn towards the influence of the defects in Secs. 4.2.2 and 4.2.3. In Sec. 4.2.4, we conclude this investigation by analyzing the effects of bulk diffusion.

4.2.1. Preliminary remarks

Fixed simulation parameters

All simulations were carried out with the same surface size $L_x = L_y = 300\,\text{nm}$, and the simulations were always terminated when the value of the height L_z reached 100 nm. Apart from that, the simulation model involves a considerable number of parameters, but not all of them have been varied for this study. As it is the goal to show the effects of the extensions of the simulation scheme developed by Rosenthal *et al.*, many values of the parameters have been taken over from previous investigations. For completeness, all fixed parameters are summarized in the following list. For further details and thorough discussions, it is referred to Refs. [9, 34, 36].

- The diffusion coefficient of atoms on the surface, D_1^s, was set to the fixed value $1.7 \times 10^{-11}\,\text{cm}^2/\text{s}$, which is close to the values which were used in Ref. [9].

- In Refs. [34] and [9], bulk diffusion was neglected, i.e., atoms and clusters in the bulk were unable to move. In some cases, the neglect of bulk diffusion may indeed correspond to the actual behavior of a real system. As far as only computational aspects are considered, however, it is most important that the simulation times are much shorter without bulk diffusion. For this analysis, we will first keep the assumption that bulk diffusion can be neglected, in Secs. 4.2.2 and 4.2.3, and later, in Sec. 4.2.4, we will study possible deviations caused by variations of the bulk diffusion coefficient D_1^b.

- The interaction length was set to 0.3 nm.

- The critical radius for the onset of columnar growth was set to $r_{\text{crit}} = 1.15\,\text{nm}$, which corresponds to a cluster size of 500 atoms.

- The radius of the defects was set to 0.3 nm.

Deposition rates

All simulations have been performed with the same deposition rate of metal atoms, $R_m = 0.8\,\text{nm/min}$, but different deposition rates of the polymer, R_p. For the discussion of the results, the ratio

$$\kappa := \frac{R_m}{R_p} \tag{4.9}$$

will be used. Just as in Refs. [9, 34], the results in this work have been obtained for κ-values between 0 and 5. We will see that this range covers the characteristic increase of the filling factor that is related to the onset of columnar growth.

Analyzed column properties

In this chapter, most quantitative statements concerning the growth of nanocolumns build on three quantities extracted from the simulation data: the number of columns, the diameter of the columns, and the volume filling factor. As mentioned before, the filling factor, labeled f, denotes the ratio of the volume of the deposited metal, V_{m} and the total volume of the composite,

$$f = \frac{V_{\mathrm{m}}}{L_x L_y L_z} \ . \tag{4.10}$$

The diameter of a column, d_0, is obtained by dividing the widths of the sphere segments by the total number of sphere segments. However, if bulk diffusion is allowed, a correction to this value is applied to account for clusters which are trapped at a column: if we let h be the height of the column, the corrected diameter is defined as the diameter of a cylinder with the height h whose volume is equal to the sum of the volume of the column, approximated by $\pi(d_0/2)^2 h$, and the total volume of the trapped clusters. Hence, the correction of the diameter describes the radial extension of the column if the total volume of all clusters is homogeneously distributed on the side surface of the volume.

Computational aspects

Each simulation run was executed on one CPU core. So far, no parts of the code support parallel running. The longest simulation times are required when many deposited atoms are removed due to re-evaporation. This can be the case when the rate ν_{re} is high or when the number of defects is very low. With the aforementioned settings for the simulation box, the total number of all involved atoms may grow up to the order of 10^8. While the treatment of such a high number of atoms would exceed the capabilities of most atomistic simulations, the computation times with the present KMC model always remained below 10 hours.

4.2.2. Influence of defects on the substrate

Although the KMC program had already offered the possibility to study the influence of defects existing on the surface before the deposition starts, such an analysis has not yet been performed for nanocolumnar growth. For this reason, we will do this in this section by considering variable defect densities ρ for hexagonal and random arrangements of defects. The more complicated situation, the continuous creation of defects during the deposition process, will be in the focus of Sec. 4.2.3.

Hexagonal pattern of defects

If a polymer substrate is pre-treated in a plasma environment to create defects in the surface, a disordered arrangement of defects will appear. From a theoretical point of view, however,
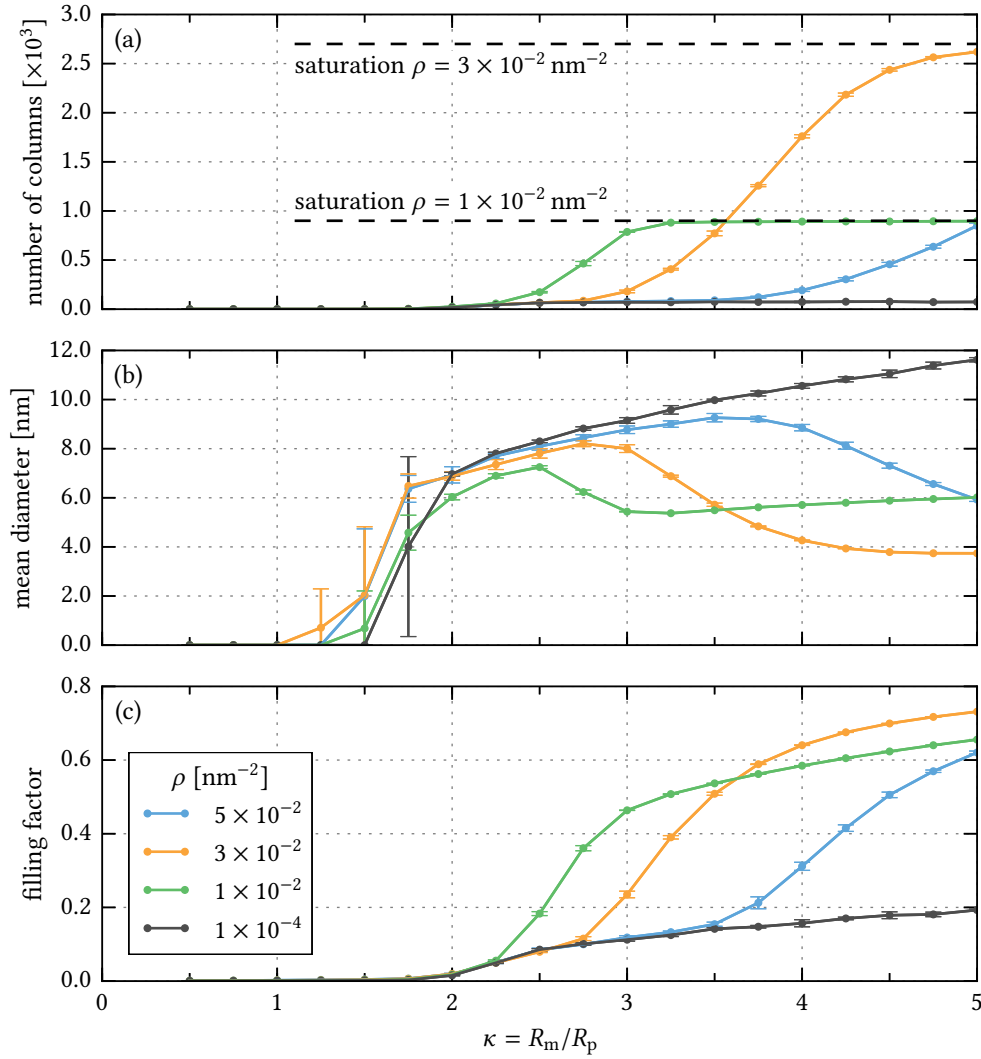
Figure 4.4.: Column properties as a function of the ratio of metal and polymer deposition rates for different defect densities ρ. The results have been obtained with a hexagonal arrangement of defects and the re-evaporation rate $v_{\mathrm{re}} = 0.9 v_1^{\mathrm{s}}$. Each point of the curves represents an average value obtained from 5 simulations with the same parameters, but different seeds of the random number generator. The errorbars indicate the standard deviation. Adapted from [141].

it is also of interest to study an idealized case where the defects are placed on a lattice. For example, this has the advantage that one can easily check if the nanocolumns reproduce the pattern of the defects by creating visualizations of the simulation results. Beyond that, one can avoid different distances between the defects, which allows for a further simplification of the analysis. Before we turn towards a random distribution of defects, we will therefore

concentrate on the idealized case that the defects are arranged on a hexagonal lattice. For the most part, the basis for our observations will be provided by Fig. 4.4, where the κ-dependence of the number of columns, the mean diameter of the columns and the filling factor is shown for $v_{\mathrm{re}} = 0.9 v_1^{\mathrm{s}}$ and four different defect densities[2] ρ. At first, we make a detailed analysis for an intermediate value of ρ. Only then, we describe the effects that result from an alteration of the defect density. Finally, we also make a brief analysis of the lengths of the columns.

Investigation for an intermediate defect density. We start by considering the data for $\rho = 1 \times 10^{-2} \, \mathrm{nm}^{-2}$, as it most obviously displays the behavior described in Refs. [9, 34]: as shown by Fig. 4.4a, no columns are formed for small values of κ because the amount of deposited metal is so small that the clusters radii do not exceed the critical value. This changes when κ is between 2 and 3 as the number of columns steeply increases and the number of spherical clusters decreases, cf. Fig. 4.5. In Fig. 4.4c, we find that the onset of columnar growth is associated with a sharp increase of the filling factor. This can be explained by the fact that the top parts of the columns provide a large area of the surface at which subsequently deposited atoms are captured. For $\kappa > 3.5$, the number of columns already reaches a saturated state: in this regime, an increase of κ only leads to thicker columns, cf. Fig. 4.4b, but *not more* columns—the filling factor still increases as it reflects the growing relative amount of metal in the system. Unlike the number of columns and the filling factor, the diameter of the columns is a non-monotonic function of κ. It attains a maximum value of approximately 7 nm close to $\kappa = 2.5$, where the curvatures of the other quantities change their sign. The occurrence of the maximum can be explained by considering the competing growth events of different columns: for a critical value of κ, the number of columns is so high that a uniform distribution of the deposited metal comes along with a reduction of the amount of metal per column. Only when the number of columns does not change any more, the increase of the diameter becomes monotonic.

Visualization of clusters and columns. Before we continue with the analysis of other defect densities, we specify the observations for $\rho = 1 \times 10^{-2} \, \mathrm{nm}^{-2}$ with the aid of the visualizations in Fig. 4.6. The images in this figure provide a top view and an auxiliary view of the final system configurations of three simulations with different values of κ. In the first row, for $\kappa = 0.5$, no columns, but only spherical clusters are present. These clusters are uniformly distributed over the whole polymer matrix—only at the bottom of the simulation box, most clusters are very close to a defect, but this is hard to recognize in the images.

The second row of Fig. 4.6, representing $\kappa = 2.5$, displays some features that are characteristic of the onset of columnar growth: both clusters and columns co-exist, but the number of clusters is already strongly reduced. In addition to this, the arrangement of the defect already plays a crucial role because all columns and almost all clusters are located at a defect site. In the following, we explain the depicted configuration in the figure by tracing it back to some important steps at the beginning of the growth process. When the deposition starts, it

---

[2]The listed values of ρ are the values that have been used as an input for the simulation program. The values of ρ used in the actual simulations may be slightly altered to satisfy the requirement of a hexagonal lattice structure. For the given surface size, the resulting deviations are negligible.

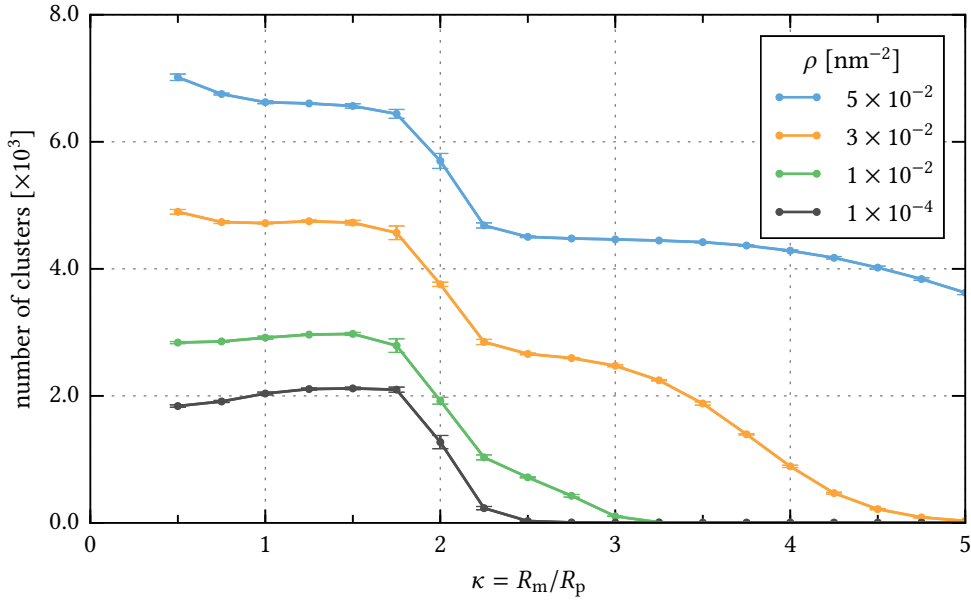Figure 4.5.: Dependence of the number of spherical clusters on the ratio of metal and polymer deposition rates for different defect densities ρ. The results have been obtained with a hexagonal arrangement of defects and the re-evaporation rate $v_{re} = 0.9v_1^s$. Each point of the curves represents an average value obtained from 5 simulations with the same parameters, but different seeds of the random number generator. The errorbars indicate the standard deviation.

is unlikely that clusters nucleate at a position outside the vicinity of a defect because the re-evaporation rate, $v_{re} = 0.9v_1^s$, is very high. As the amount of deposited metal suffices to cover almost all defects with a cluster—only one defect site remains free in this example—nearly all deposited atoms are either absorbed by these immobile clusters or re-evaporate from the surface. While the deposition process continues, the clusters grow at nearly the same rates until some of them eventually turn into a column. It depends on just small fluctuations of the growth rates which clusters become columns and which not. Once all columns have formed, it becomes more and more unlikely that deposited atoms are attached to one of the clusters instead of a column. Hence, the growth of clusters is disrupted and only the columnar growth persists. From that point on, the growth is stationary, i. e., the characteristics of the resulting composite will not change any more. Even if new clusters are formed by random nucleation on the elevated surface, it is unlikely that they are buried before they diffuse into an area where they are absorbed by a column. Hence, the only essential effect of the deposition in the remaining time is a vertical extension of the columns.

Based on the explanations for $\kappa = 2.5$, we can immediately understand the behavior for $\kappa = 4$, depicted in the third row of Fig. 4.6: in this case, the amount of deposited metal is large enough that all initially existing spherical clusters turn into columns. As these columns absorb almost all atoms and clusters in the space between them, the number of columns

remains equal to the number of defects. In accordance with the aforementioned observations from Fig. 4.4, the images in the third row are exemplary for the behavior in the regime where the number of columns cannot be further increased just by raising the ratio κ. If the corresponding images for any other κ-value in that regime had been used, they would look very similar: the number of columns would be the same, but the thickness of the columns would be slightly different.

To conclude, we can state that the graphical analysis has helped us to show that the saturation of the number of columns occurs when each defect is the origin of one column. Hence, the total number of columns can be calculated from the expression $\rho L_x L_y$. The lower one of the two horizontal lines in Fig. 4.4a represents exactly that value for the density $\rho = 1 \times 10^{-2} \, \mathrm{nm}^{-2}$; in fact, it accurately captures the simulation results for large values of κ.

Before we proceed, we use the images shown in Fig. 4.6 to make some additional remarks concerning the shape of the columns. All the columns extend over the whole space of the simulation box in vertical direction, i.e., their lengths are roughly $100 \, \mathrm{nm}$. Although the columns consist of multitudinous stacked sphere segments, their widths exhibit only small fluctuations. The bottom parts of the columns reveal some details of the initial phase of their growth: once a spherical cluster becomes large enough that the columnar growth is initiated, the thickness of the column steadily increases until a stable value is reached. This behavior is in agreement with a similar observation made with a continuous model to describe the growth of nanocolumns in Ref. [144]. Nevertheless, we may have some doubts about the description of the very thin part of the column where the spherical part at the bottom merges into the elongated part. It is plausible that this is just an artifact of the simulation model which results from the discontinuous change from one growth mode to the other. However, we cannot expand on this without further reference data.

Effects of increased/reduced defect densities.   Now that we have given a detailed explanation for the behavior associated with $\rho = 1 \times 10^{-2} \, \mathrm{nm}^{-2}$, we can turn towards other values of the defect density and discuss the occurring deviations. To begin with, we consider the value $\rho = 3 \times 10^{-2} \, \mathrm{nm}^{-2}$ because the behavior is quite similar: again, the onset of columnar growth is associated with a steep increase of the filling factor and the occurrence of a maximum column thickness, but the growth sets in for larger values of κ. The reason for this is the following: when the number of defects is increased, the number of clusters nucleating at the beginning of the deposition process becomes larger, too. As all clusters together contain nearly the same amount of metal as the clusters occurring for $\rho = 1 \times 10^{-2} \, \mathrm{nm}^{-2}$, the average cluster size is smaller. At the same time, that means that more metal—and thus a larger value of κ—is required for the columnar growth to set in. Just as for $\rho = 1 \times 10^{-2} \, \mathrm{nm}^{-2}$, we could again observe the tendency that each column grows at a defect site, but this is not explicitly shown here. In the saturated state, the number of columns therefore becomes three times as large as for $\rho = 1 \times 10^{-2} \, \mathrm{nm}^{-2}$. However, as the columnar growth sets in for larger values of κ, the occurrence of saturation is shifted to larger κ, too. In fact, Fig. 4.4a reveals that even for $\kappa = 5$, the number of columns has not yet reached the expected maximum, i.e., the same value as the number of defects. Considering the thickness of the columns and the filling factor, we find that the relation between these quantities and the number of columns is similar to
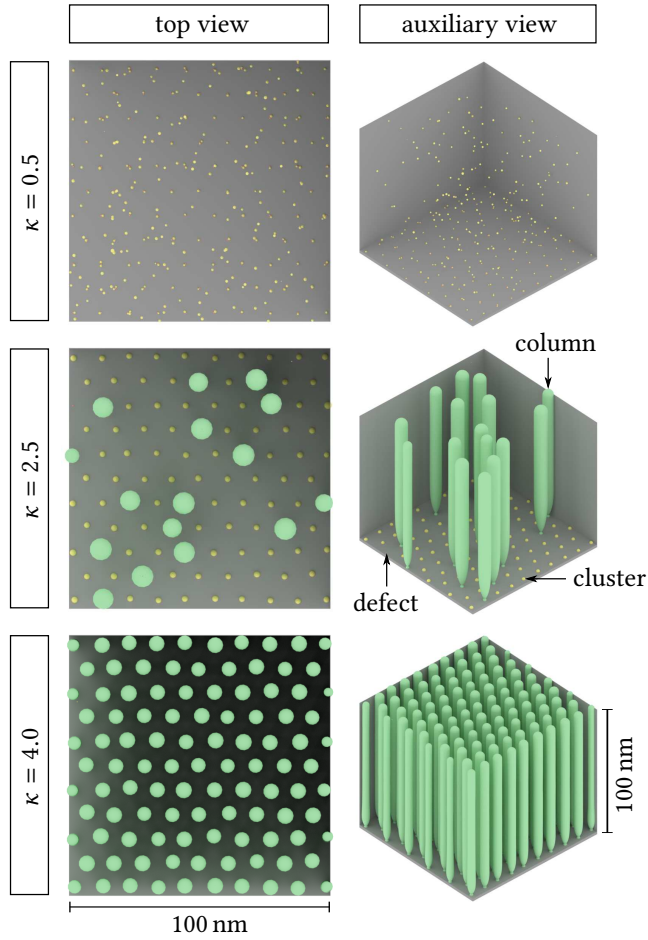
Figure 4.6.: Illustration of the distribution of nanocolumns (green) and clusters (yellow) for different values of κ, as seen in a top view and in an auxiliary view. The empty space between the columns and clusters represents the continuously modeled polymer. The simulations have been performed with a hexagonal arrangements of defects with the density $\rho = 1 \times 10^{-2}\,\mathrm{nm}^{-2}$, and the re-evaporation rate $\nu_{\mathrm{re}} = 0.9\nu_1^{\mathrm{s}}$.

the case with $\rho = 1 \times 10^{-2}\,\mathrm{nm}^{-2}$. In fact, it turns out that there is a close relation between the thickness of the columns and the number of columns which is widely independent of the defect density. For example, this becomes apparent for $\kappa \approx 3.5$, where the number of columns and the mean diameter are the same for $\rho = 3 \times 10^{-2}\,\mathrm{nm}^{-2}$ and $\rho = 1 \times 10^{-2}\,\mathrm{nm}^{-2}$. Beyond that, even the curves of the filling factor intersect with each other at that point. The reason for this is that the total volume of the spherical clusters can be neglected in this regime. The volume of the metal can thus be approximated by the product of the number of columns and the mean diameter, which is the same for $\rho = 3 \times 10^{-2}\,\mathrm{nm}^{-2}$ and $\rho = 1 \times 10^{-2}\,\mathrm{nm}^{-2}$.

Now we consider the defect density $\rho = 5 \times 10^{-2}\,\mathrm{nm}^{-2}$. Compared to the two other discussed values, the columnar growth is strongly suppressed: the considered range of κ-values only covers the initial increase of the number of columns, and even for $\kappa = 5$, the value is still far below the value 4500, which we obtain by using again the product $\rho L_x L_y$ to estimate the number of columns in the saturated state. Apart from this, however, the system behaves similarly to the previously discussed cases. For example, the mean diameter of the columns attains a maximum value at $\kappa \approx 3.5$, but the peak is much broader. We can therefore expect that the mentioned trends persist also for $\rho = 5 \times 10^{-2}\,\mathrm{nm}^{-2}$, but the saturation of the number of columns sets in for a very large value of κ which is not covered by the present data.

To conclude the investigation of the quantities shown in Fig. 4.4, we turn towards the lowest of the four densities, $\rho = 1 \times 10^{-4}\,\mathrm{nm}^{-2}$. Although the length of the vertical axis in Fig. 4.4a makes it difficult to recognize any details, we can find again that the number of columns goes into saturation. However, in this case, the value is on the order of 70, which is significantly larger than the value 9 resulting from the product $\rho L_x L_y$. We can thus deduce that the considered defect density yields an example for the case when the number of defects is so small that their influence can be neglected; in such a case, the columnar growth is initiated by a sequence of random nucleation events rather than preferred nucleation events at defect sites. This behavior also causes the occurrence of a disordered arrangement of the columns instead of the previously observed hexagonal arrangement. Furthermore, it may even happen that some of the columns are formed at elevated surface heights instead of the bottom of the simulation box. An example for this behavior can be found in Fig. 4.7, where the final configuration of a simulation with the parameter $\kappa = 5$ is shown. Now, considering the diameter of the columns shown in Fig. 4.4b, we find that the density $\rho = 1 \times 10^{-4}\,\mathrm{nm}^{-2}$ yields the largest values for almost all employed values of κ. Again, this can be explained by the small number of columns resulting in a reduced relevance of the competition between growth events at different columns. Nevertheless, the curve for the filling factor reveals that the increased thickness does not compensate for the low number of columns: the values remain below the values of the other curves in almost all cases. In particular, these differences become very large as κ is increased from 3.5 to 5.

Lengths of the columns. While we have so far concentrated on the diameter of the columns and made some remarks on the shape of the columns, we now move to make a brief analysis of the lengths of the columns. In most of the previously discussed examples, almost all columns originate from a large cluster at the bottom of the simulation box, and they continue to grow until the simulation is stopped. However, we have already seen by the example of Fig. 4.7 that there are conditions under which there is a high chance that some columns are formed far above the initial surface height. It has been found that this is the main reason for the occurrence of columns whose lengths are below the final thickness of the composite. In the following, we therefore complement the previous analysis by discussing the distributions of the column lengths for different defect densities ρ. In doing so, we refer to data for the selected value $\kappa = 5$ shown in Fig. 4.8. For all values of ρ, the curves exhibit a sharp maximum close to the final thickness of the composite, namely 100 nm. However, it is
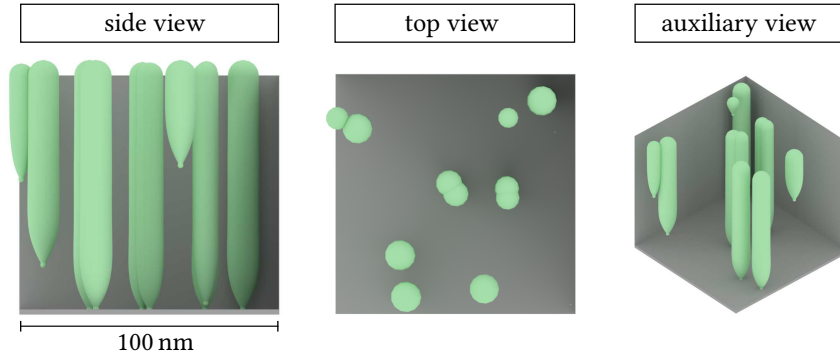
Figure 4.7.: Illustration of the final arrangement of the columns occurring in a simulation with the parameters $\kappa = 5$, $v_{\mathrm{re}} = 0.9v_1^{\mathrm{s}}$, and the defect density $\rho = 1 \times 10^{-4}\,\mathrm{nm}^{-2}$. As a peculiarity of simulations with low values of ρ, columns are not only formed at the bottom of the simulation box, but also at elevated heights. Beyond that, the images give some examples for the intersection of two columns.

apparent that all peaks occur for values that are slightly larger than 100 nm. The reasons for this that the routine to measure the length of a column computes the difference between the highest point of the spherical cap at the top of a column and the lowest point of the spherical part at the bottom. As explained in Sec. 4.1.1, the z-coordinate of the latter point may even have a negative value. Hence, the length of a column may be slightly larger than the height of the simulation box.

Looking at the data more closely, we first notice that there are small variations of the peak positions which depend on the value of the defect density. Comparing with the mean diameter of the columns for $\kappa = 5$ shown in Fig. 4.4b, we find that the position of the peaks reflects the thickness of the columns: the thicker a column is, the larger is the value of the peak position. Again, this follows from the fact the top of the column is a spherical cap: the radius of the corresponding sphere, which is approximately equal to the radius of the column, is also a rough measure for the difference between the column length and the height of the surface. While the distributions for all densities look very similar, the most apparent deviations from the common trend are displayed by the curve for the defect density $\rho = 1 \times 10^{-4}\,\mathrm{nm}^{-2}$: the main peak after 100 nm is the flattest and broadest of all four peaks, and the flat branch below 100 nm displays a multitude of very small side peaks with strong fluctuations. In fact, these peaks exactly reflect the previously observed occurrence of columns with displaced origins. Although this effect is clearly noticeable, the relative amount of such shortened columns is still small. We will later see that the creation of defects during the deposition process may lead to an enhancement of this trend.

Randomly distributed defects

In this section, we extend the analysis of the column properties to the case where the defects are randomly distributed on the initial surface. The employed probability density is uniform,
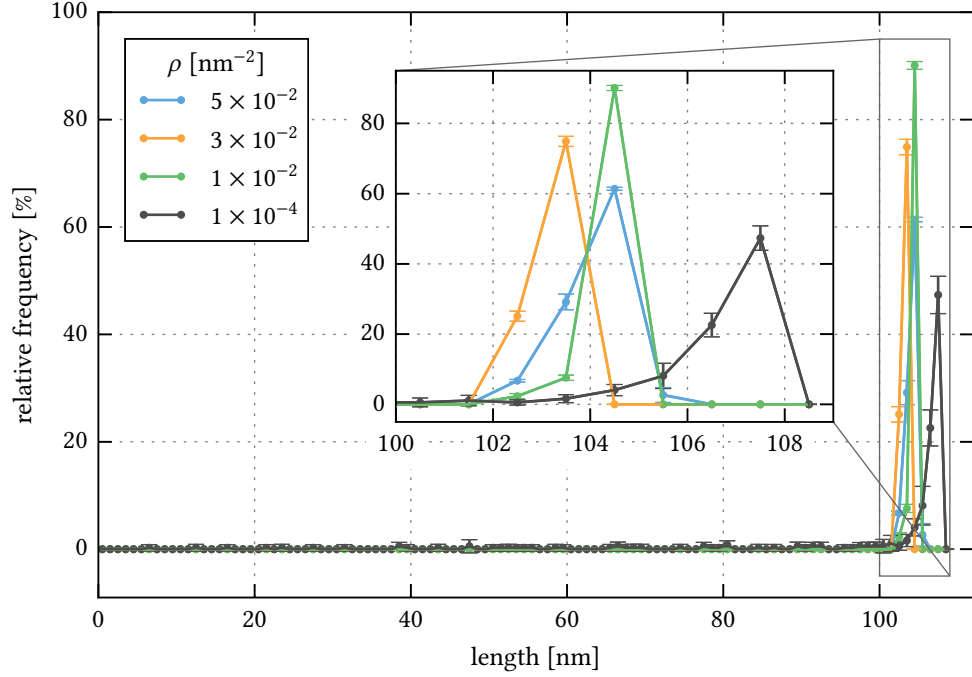
Figure 4.8.: Distribution of final column lengths occurring in simulations with the same parameters $\kappa = 5$ and $v_{\mathrm{re}} = 0.9v_1^{\mathrm{s}}$, but different values of the defect density ρ. The arrangement of the defects was hexagonal. Each curve represents the average values obtained from 5 simulations with the same parameters, but different seeds of the random number generator. The errorbars indicate the mean deviations from the indicated values. Adapted from [141].

i. e., no regions of the surface are preferred, and the overlapping of defects is not forbidden. In the following, we will study this case on the basis of the data shown in Fig. 4.9. These results have been obtained in simulations with the same parameters as the results in Fig. 4.4, but a disordered arrangement of defects was employed instead of a hexagonal one. Making use of the findings for the idealized case discussed in the previous section, we can immediately understand the main trends of the presented data. In particular, can find the same relation between the number of columns, the diameter and the filling factor. For this reason, we will restrict ourselves to investigating the quantitative deviations of the number of columns caused by the employment of a random distribution. On this view, one of the main features we observe is that the number of columns in the saturated regime of κ-values is lower than for the hexagonal arrangement. This can be explained by the fact that the random placing of the defects may lead to two or more overlapping defects which effectively count as just one defect as far as the formation of a nanocolumn is concerned. The relevance of this effect particularly increased for high defect densities. In the following, we make an attempt to convert the density ρ to an effective density ρ_{eff} that we can be used to predict the number of
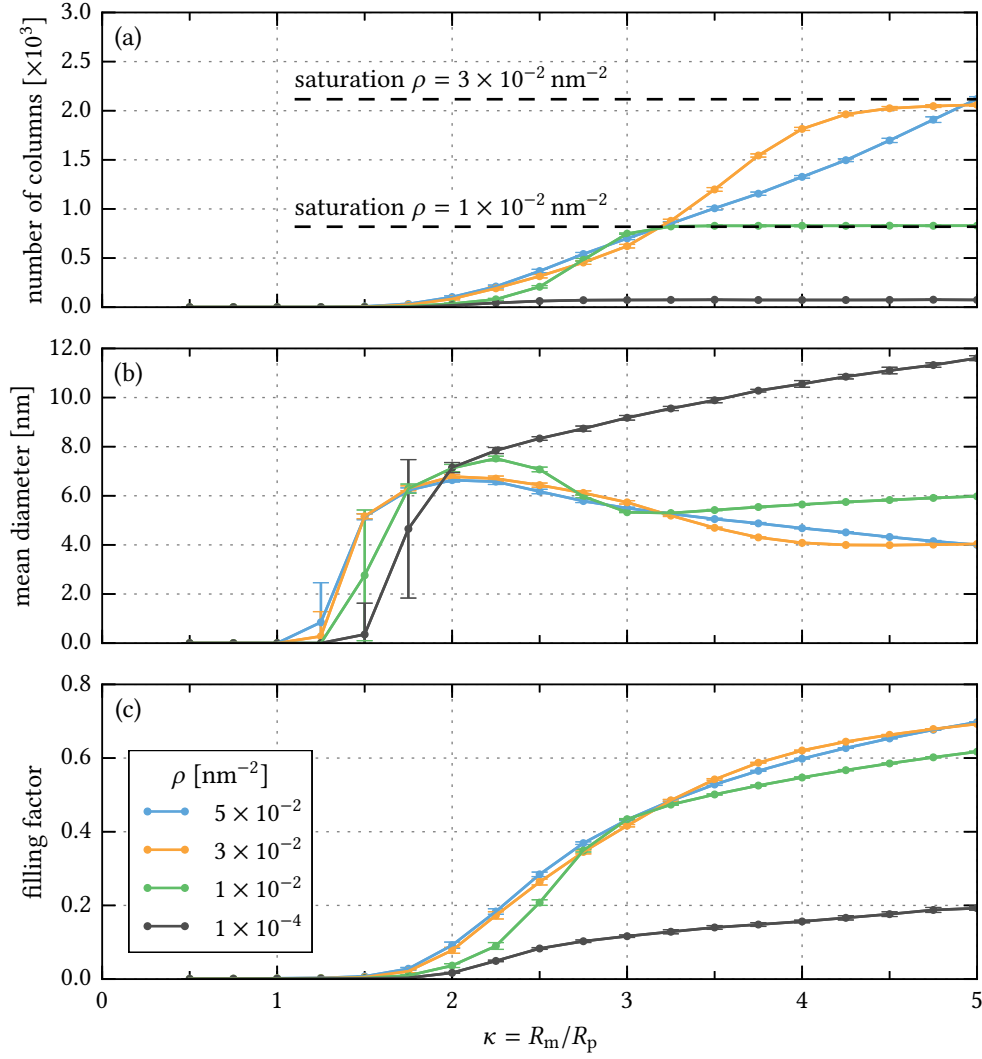
Figure 4.9.: Column properties as a function of the ratio of metal and polymer deposition rates for different defect densities ρ. The results have been obtained with a random arrangement of defects and the re-evaporation rate $\nu_{\mathrm{re}} = 0.9\nu_1^{\mathrm{s}}$. Each point of the curves represents an average value obtained from 13 simulations with the same parameters, but different seeds of the random number generator. The errorbars indicate the standard deviation. Adapted from [141].

columns in the saturated state via

$$N_{\mathrm{columns}} = \rho_{\mathrm{eff}} L_x L_y \ . \tag{4.11}$$

For the determination of ρ_{eff}, we first express it as a fraction of the actual density ρ,

$$\rho_{\mathrm{eff}} = k\rho \ , \tag{4.12}$$
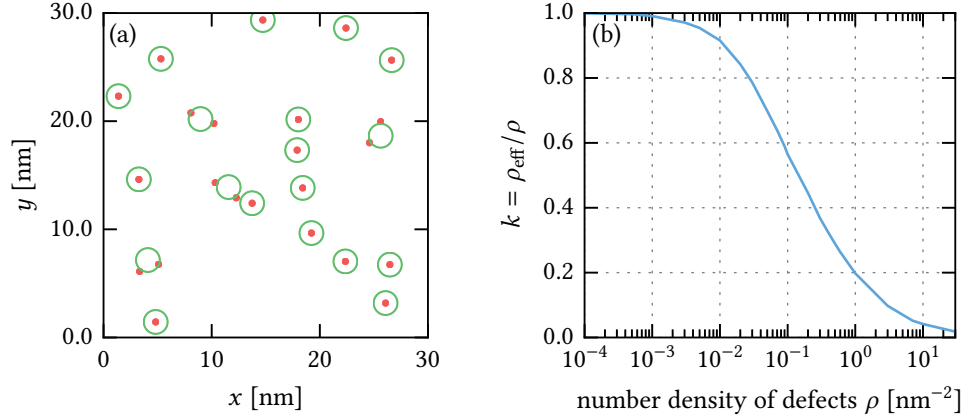
Figure 4.10.: (a) Exemplary coverage of defects (red) with columns (green), as suggested by the algorithm described in the text. The defect density for this example is $\rho = 1 \times 10^3 \, \mathrm{nm}^{-2}$. (b) Dependence of the factor k, introduced in Eq. (4.11), on the defect density ρ. Adapted from [141].

where only the factor $k \in [0, 1]$ remains to be determined. We can expect that k is not constant, but an unknown function of the density ρ_{eff}. To determine this function, we first assume that the factor $(1 - k)$ denotes the fraction of defects which have at least one neighbor that is so close that at most one column can be formed in their vicinity. In fact, we do not know in advance how large the minimum distance between two defects must be such that each of them may become the origin of a column. Yet, we can make a guess for the value of this quantity and check if the number of columns can be predicted with that. In this spirit, a separate Monte Carlo routine has been written to detect agglomerates of randomly placed defects for arbitrary densities. The employed algorithm works as follows: First, the density ρ and the dimensions of a sufficiently large surface are fixed. Then, a number of points that represent the defects at the given density are created on the surface. Finally, the algorithm searches for arrangements of equal-sized circles which cover all points on the surface. These circles represent the columns; as their radius must be guessed, the value $1.15 \, \mathrm{nm}$—the critical radius for the onset of columnar growth—has been used. Furthermore, a point is defined to be covered by a circle if the distance between the point and the center of the circle is less than the sum of the radius of the circle and half the defect radius. Again, this definition is rather arbitrary, but it has been found to work out for this purpose. Among all found arrangements of circles, only the one with the smallest number of circles is accepted. In order to obtain good statistics for a given defect density ρ, this routine can be repeated many times. Last of all, the factor k is extracted from the ratio of the average number of required circles and the number of points. For a further illustration of the method, it is referred to Fig. 4.10b, which shows an exemplary configuration of circles and points that the algorithm has produced for the density $\rho = 3 \times 10^{-2} \, \mathrm{nm}^{-2}$. The results for the dependence of k on ρ, are shown in Fig. 4.10a: in accordance with the above assumptions, the factor k smoothly transitions from 1, for low densities, to zero, for high densities.

The two horizontal lines in Fig. 4.9a indicate the predicted values of the number of columns using the formula $N_{\text{columns}} = k\rho L_x L_y$ for the densities $\rho = 1 \times 10^{-2}\,\text{nm}^{-2}$ and $3 \times 10^{-2}\,\text{nm}^{-2}$; the corresponding values of k are 0.91 and 0.75. For $\rho = 1 \times 10^{-2}\,\text{nm}^{-2}$, the simulation results are accurately captured in the regime $\kappa \geq 3.25$. Also, for $\rho = 3 \times 10^{-2}\,\text{nm}^{-2}$, the prediction seems to be accurate, but further data points for $\kappa > 5$ would be required to analyze this in greater detail.

Comparing the curve for $\rho = 5 \times 10^{-2}\,\text{nm}^{-2}$ with the corresponding curve for the case of hexagonally arranged defects, we notice that the curve for the random arrangement reaches much higher values in the displayed range of κ-values. Again, we can explain this behavior with the overlap of a certain amount of defects, which makes a characteristic difference in this case: for the random arrangement, the effective density ρ_{eff} is so much smaller than ρ that the tendency of the defects to shift the onset of columnar growth to larger values of κ becomes much less relevant. In neither case, however, the presently considered range of κ-values permits a check of predictions concerning the number of columns at saturation; even for $\kappa = 5$, both curves are still far from leveling off.

Lastly, we briefly consider the value $\rho = 1 \times 10^{-4}\,\text{nm}^{-2}$. In this case, the density is so low that the overlapping of two defects is very unlikely. Consequently, the data shown in Figs. 4.9a–c for this value of ρ is nearly identical to the corresponding data for the hexagonal arrangement shown in Figs. 4.4a–c. As it is again the case that the number of columns is much higher than the number of defects, this means in particular that Eq. (4.11) cannot yield correct predictions for low densities. Currently, it is therefore only possible to ascertain that the concept of effective defect densities is appropriate for intermediate values of ρ.

4.2.3. Defect creation during deposition

In this section, we extend the previous analysis by considering the more complex case when new surface defects may be formed at any point during the deposition process. In doing so, we can expect that the description becomes more appropriate for the sputter deposition method, as it is characterized by frequent impacts of highly energetic particles on the substrate. For the most part, we will base this discussion on the the simulation results presented in Fig. 4.11. The figure shows the κ-dependence of the number of columns, the mean diameter of the columns and the filling factor for different values of the parameter $\gamma = J_{\text{d}}/J_{\text{m}}$, which denotes the ratio of the fluxes of defects and atoms towards the surface, see Eq. (4.8). As it very difficult to find a mapping between the conditions of an actual experiment, e. g., a set of plasma parameters, and the required values of γ, the simulations have been performed with different values of γ which cover several orders of magnitude. As mentioned before, also the re-evaporation rate remains a free parameter on this level of description. For this reason, both columns of the figure are intended to represent the cases of high and low re-evaporation rates, namely $\nu_{\text{re}} = 0.9\nu_1^{\text{s}}$ and $0.2\nu_1^{\text{s}}$. Despite the creation of defects during the deposition, an initial distribution of defects on the surface has also been employed in this case; the arrangement was random, and the density was $\rho = 1 \times 10^{-2}\,\text{nm}^{-2}$. All other simulation parameters—which are not explicitly listed here—do not differ from the values used for the results of the previous section.

Again, we start the discussion by first considering the number of columns. For the results
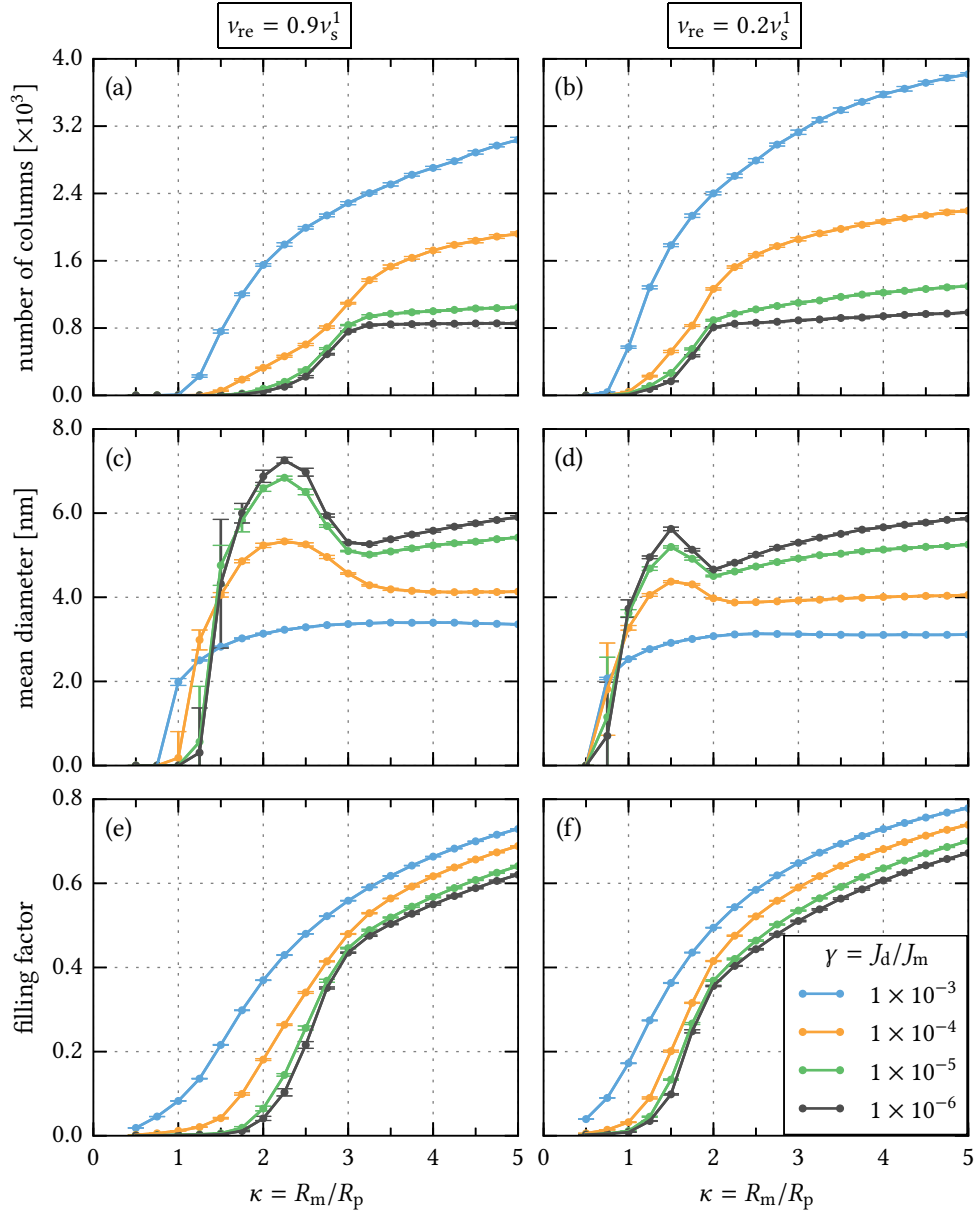
Figure 4.11.: Column properties as a function of the ratio of metal and polymer deposition rates for two different re-evaporation rates ν_{re} and different fractions of deposited defects γ. Each point of the curves represents an average value obtained from 12 simulations with the same parameters, but different seeds of the random number generator. The errorbars indicate the standard deviation. Adapted from [141].
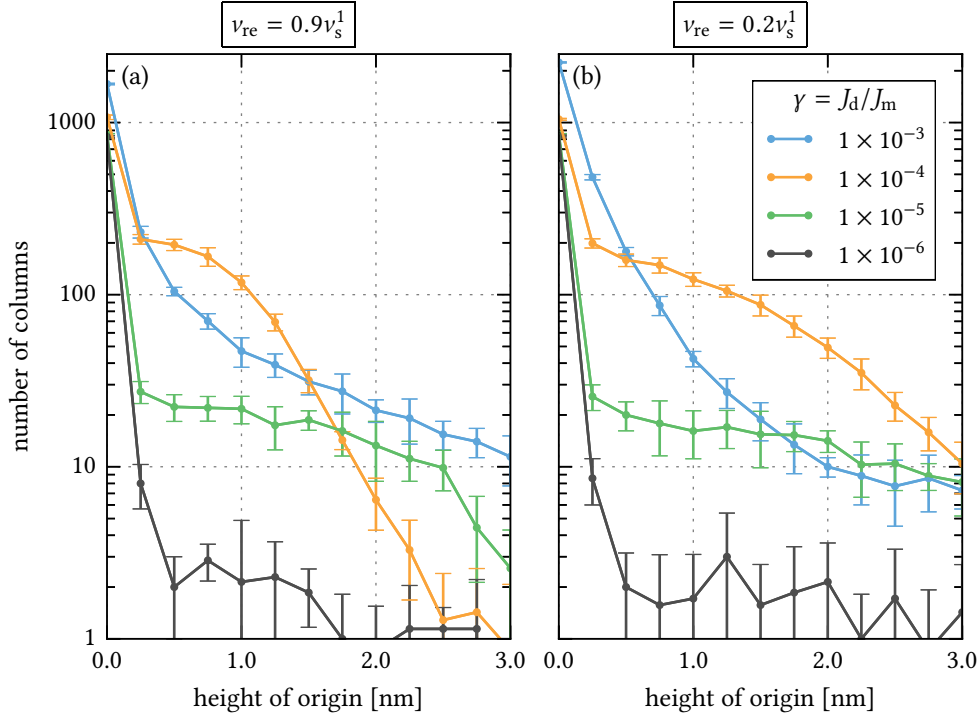
Figure 4.12.: Influence of the ratio γ on the distribution of heights at which the nanocolumns are formed in the simulations. The results in (a) and (b) have been obtained for two different values of the re-evaporation rate ν_{re}. Each curve represents the average values obtained from 7 simulations with the same parameters, but different seeds of the random number generator. The errorbars indicate the mean deviations from the indicated values.

for the parameters $\gamma = 1 \times 10^{-6}$ and $\nu_{re} = 0.9\nu_1^s$, the effect of the additionally created defects is still weak. Hence, the curve is nearly identical to the corresponding curve shown in Fig. 4.9a. However, we find some deviations for $\nu_{re} = 0.2\nu_1^s$, which has not been considered in the previous section: apparently, the use of a small re-evaporation rate shifts the steep increase of the number of columns to smaller values of κ, and—instead of a branch with constant values—the steep increase is followed by another increase, but the corresponding slope is very slow. Such an additional increasing part for large values of κ is caused by the increased probability for the formation of columns in the space between the majority of columns which originates from defect sites. While this behavior can can be nearly completely suppressed for the re-evaporation rate $\nu_{re} = 0.9\nu_1^s$, it obviously has a noticeable effect for $\nu_{re} = 0.2\nu_1^s$. Despite these small differences, we will simplify the following discussion by referring to both values of ν_{re} at the same time. In fact, all effects mentioned below are similar in both cases, only they are more pronounced for the smaller re-evaporation rate, $\nu_{re} = 0.2\nu_1^s$.

When γ is raised, we notice three dominant effects: the number of columns is raised for all considered values of κ, smaller values of κ are required to observe the growth of nanocolumns,
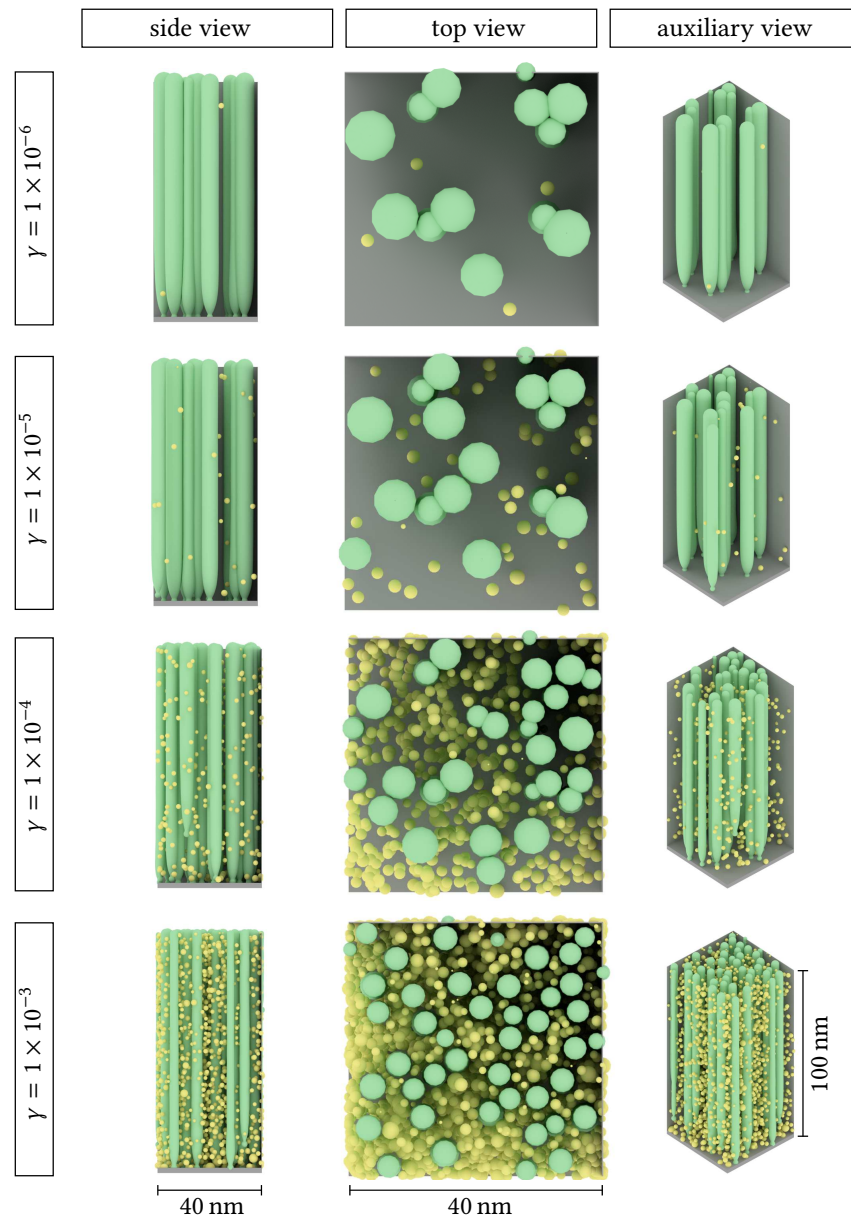
Figure 4.13.: Rendered illustration of columns and spherical clusters for different values of the parameter γ, which is used to control the amount of defects created during deposition. The images correspond to the final states of simulations with $v_{\text{re}} = 0.9 v_1^{\text{s}}$ and $\rho = 1 \times 10^{-2}\,\text{nm}^{-2}$. It can be noticed that several columns shown in the first and second row have the same positions. The reason for this is that the initial distribution of defects has been the same in all simulations—also for $\gamma = 1 \times 10^{-4}$ and 1×10^{-3}, but in these cases, the influence of the initially existing defects is negligible.

and the constant (or nearly constant) part for large κ-values gets replaced by a part that displays an ongoing increase. With the same arguments as in the previous section, we can immediately understand the first point: an increased amount of defects leads to more columns because they preferably growth in the vicinity of a defect. Yet, the last two points are different from the corresponding behavior we observed in Figs. 4.4 and 4.9 for an increase of ρ. For example, we found that an increase of ρ shifts the onset of columnar growth to larger κ-values, but an increase of γ does the opposite. The reason for this contrary behavior is the placing of the defects: the initially existing defects are all placed at the initial height $z = 0$. That means that the formation of nanocolumns is most likely when the amount of deposited metal suffices to form them before these defects are buried due to the elevation of the surface. In contrast, if the defects are permanently created during deposition, the situation is different: the ongoing addition of defects makes it much more likely that nanocolumns are also formed at later stages of the deposition, i.e., also when the surface has reached a high position. A confirmation of this trend is also provided by Fig. 4.12, which shows the distribution of column origins for all considered values of γ and ν_{re}. Yet, the data in the figure reveals that the difference occurring due to the growth of additional columns at elevated heights is still made at the early stage of the deposition: the relative amount of columns whose origin is above a height of 3 nm is in all cases very small. With the observation of the column formation at higher position in the simulation box, we can explain both remaining trends of the number of columns, the vanishing saturation and the shift of the increase to smaller κ-values. The other two quantities shown in Fig. 4.11 are again closely related to the number of columns: the thickness of the columns reaches the largest values for the smallest value of γ because of the reduced amount of competing growth events for a small number of columns. The curves for the filling factor have the same order as the curves for the number of columns, i.e., the largest filling factors are associated with a large number of defects.

For additional insights on the influence of the parameter γ, we make again use of visualizing the final system configurations. In Fig. 4.13, the final states are shown as seen in three different views for all considered values of γ between 1×10^{-6} and 1×10^{-3}. The images confirm all above discussed trends—in addition to this, they show that an increase of γ is related to a strong increase of the number of spherical clusters in the space between the columns. These clusters are preferably formed at the additional defect sites, i.e., most of the clusters are immobile and cannot be absorbed by the columns. The simultaneous presence of both columns and clusters is a characteristic effect of the creation of defects during deposition—in the preceding studies without the addition of defects, we have always found that either columns or clusters prevail against the other ones.

4.2.4. Influence of bulk diffusion

All the previous findings are based on the assumption that the columnar growth is only weakly influenced by cluster diffusion processes in the bulk. In this section, we seek to verify this assumption by studying the column properties obtained from simulations that allow atoms and clusters to perform bulk diffusion jumps[3]. As mentioned before in Sec. 2.2, we

---

[3]For the implementation of the bulk diffusion process, the author received assistance from Nuttawut Kongsuwan.
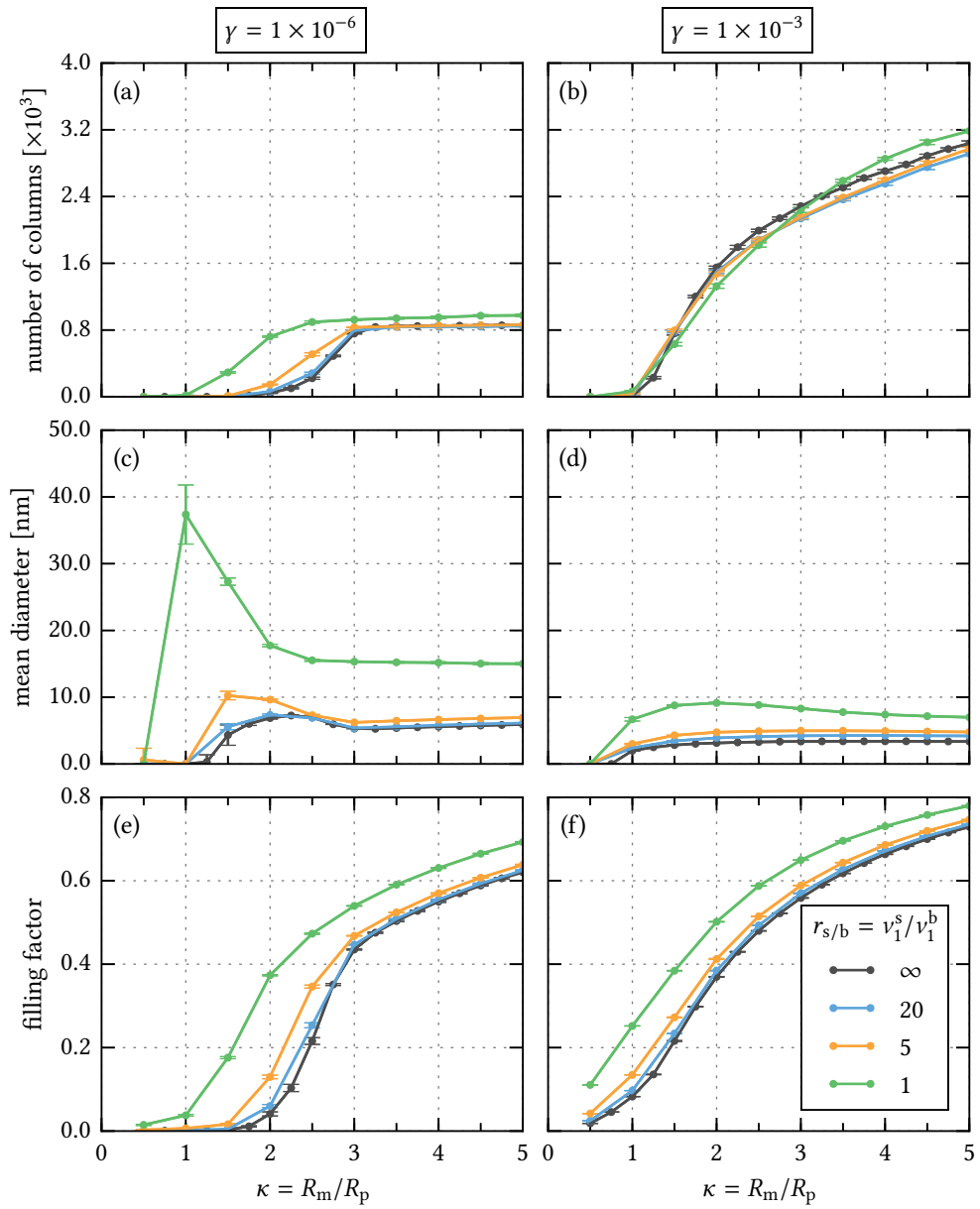
Figure 4.14.: Influence of the ratio of surface and bulk jump rates for atoms, $r_{s/b} = v_1^s/v_1^b$, on the growth of nanocolumns. The case $r_{s/b} = \infty$ corresponds to simulations without bulk diffusion. All simulations have been performed with the same re-evaporation rate $v_{re} = 0.9v_1^s$, but two different values of γ, 1×10^{-6} (left column) and 1×10^{-6} (right column). Each point of the curves for $r_{s/b} = 1$, and 20 represents an average value obtained from 8 simulations with the same parameters, but different seeds of the random number generator. The errorbars indicate the mean deviations from the indicated values. Adapted from [141].

cannot do such an investigation without making rough estimations for the ratio between surface and bulk diffusion coefficients. In order to make a systematic study, we therefore introduce the parameter

$$r_{\mathrm{s/b}} = v_1^{\mathrm{s}}/v_1^{\mathrm{b}} \ , \tag{4.13}$$

which denotes the ratio of the surface and bulk jump rates of atoms. Keeping the same value of v_1^{s} as before, only v_1^{b} is varied by considering three different values of $r_{\mathrm{s/b}}$: 1, 5 and 20. As compared to the previously mentioned value of roughly 60, these values are relatively small. The intention of this choice is to clearly demonstrate the trends resulting from the activation of bulk diffusion.

In the following, we discuss the results shown in Fig. 4.14. They have been obtained for the γ-values 1×10^{-6} and 1×10^{-3} in simulations with the fixed values of the re-evaporation rate, $v_{\mathrm{re}} = 0.9 v_1^{\mathrm{s}}$, and the density of randomly distributed defects, $\gamma = 1 \times 10^{-4}$. For comparison, the figure also shows the results for the case without bulk diffusion, which we loosely express by $r_{\mathrm{s/b}} = \infty$. In general, we can expect that the effect of bulk diffusion is most apparent when the influence from other circumstances that limit the diffusion of clusters is minimal. Concerning the data shown in Fig. 4.14, this is the case for $\gamma = 1 \times 10^{-6}$, because the fraction of trapped clusters is small, and for small values of κ, because the formation of large clusters and columns, which move slowly or not at all, is limited. The curves for $r_{\mathrm{s/b}} = 1$ in the left column of the figure indeed confirm this assumption. In the regime below $\kappa = 3$, all three quantities display the largest deviations.

With the exception of the curves representing the number of columns for $\gamma = 1 \times 10^{-3}$ in Fig. 4.14b—which are so close to each other that it is difficult to make out any trend—we can summarize the influence of bulk diffusion as follows: the ability of clusters to perform bulk jumps not only increases the overall mobility of the clusters, it also enables atoms to jump from the surface to the bulk and thus reduces the re-evaporation probability of atoms. Both mechanisms are conducive to the rapid formation of large clusters and columns, which is in agreement with the observation that a decrease of $r_{\mathrm{s/b}}$ leads to a shift of the increasing branch of the number of columns to smaller κ-values in Fig. 4.14a. In contrast to the many examples discussed before, we find in this case that such an early increase of the number of columns is not necessarily accompanied by a decrease of the mean diameter. Although it is again the case—at least for $\gamma = 1 \times 10^{-6}$— that the diameter has a non-monotonic κ-dependence, a decrease of v_1^{s} in all cases leads to thicker columns. The filling factor follows exactly the same trend because it reflects the increased amount of metal in the system.

According to the above description, the incorporation of the bulk diffusion process may indeed affect the columnar growth. Nevertheless, the data in Fig. 4.14 also reveals that noticeable effects only appear in specific regions of κ-values and, in particular, for very large bulk diffusion coefficients. For example, the deviations from the case without bulk diffusion that occur for $v_1^{\mathrm{s}} = 20$ are very small. Even for the ratio $v_1^{\mathrm{s}} = 5$, which is already far below the aforementioned value of 60, a neglect of bulk diffusion may still be sufficient for many practical applications. For $v_1^{\mathrm{s}} = 1$, we see rather strong deviations, but it remains questionable if this case provides a realistic representation of any relevant experimental combination of materials.

4.3. Summary

In this chapter, we used an extended version of the KMC model by Rosenthal *et al.* [9, 34] to study the influence of surface defects on the growth of nanocolumns. The defects have two opposing effects: they decrease the mobility of atoms and clusters whose diffusion is important for the growth of columns, but they also provide sites for preferred nucleation of clusters, which may eventually become large enough to form a column. The results in this chapter show that the latter effect predominates for many combinations of simulation parameters, i. e., the columnar growth can be enhanced by the addition of defects. This statement largely holds concerning the initial distribution of defects as well as the additional defects created during deposition. At this, it has been found that the thickness of the columns not only depends on the ratio of the metal and polymer deposition rates, but, in many cases, also on the number of columns. We can roughly summarize that the thickness of the columns is often decreased when the number of columns is increased. The filling factor indicates the total relative amount of metal in the system. Hence, it reflects both the number of columns and their thickness. Furthermore, it may also indicate the presence of spherical clusters existing alongside the columns, e. g., when defect creation rate is large.

As typical of KMC simulations, the present description of the metal–polymer nanocomposite formation involves a high degree of coarse graining. Still, many of the simulation parameters had to be treated as free parameters due to the lack of accurate reference data. However, since the old version of the simulation model has undergone extensive testing and adequately described the growth processes in different case scenarios [9, 34–36], we may assume that the predictive power of the extended version is on a similar level. For a deeper analysis of the accuracy, however, it would be beneficial to make comparisons with new experimental data.

Chapter 5

Growth of Gold Clusters on a Polymer Surface

Now that we have extensively studied the formation of metal–polymer nanocomposites by means of KMC simulations, we will continue by exploring an alternative approach based on atomistic MD simulations. The main advantage offered by MD simulations is that no prior assumptions about possible cluster shapes have to be made. As all atoms arrange themselves according to the energetic conditions imposed by the employed force fields, MD simulations can, in principle, produce all kinds of highly complex metallic structures. However, this only works at the cost of a large computational effort. As opposed to the KMC simulations, we will therefore concentrate on small "two-dimensional" systems in this chapter. Concerning the limitations put on the accessible time scales, we will work out a specific procedure to imitate the behavior on realistic experimental time scales.

In this chapter, we will investigate a new MD simulation scheme which was originally designed to simulate the growth of thin gold (Au) films on a polymer substrate with similar conditions as in the experiment conducted by Schwartzkopf *et al.* [61]. For this reason, we will start by summarizing the procedure of that experiment in Sec. 5.1. A detailed explanation of the simulation scheme and a discussion of the approach to reach long time scales will be given in Secs. 5.2 and 5.3. In the remaining parts of the chapter, we will study the simulated film morphology for various combinations of simulation parameters and make a comprehensive comparison with the experimental reference data from Ref. [61].

5.1. Experimental reference data

In the experiments described in Ref. [61], radio frequency sputter deposition with an argon plasma was performed to grow a nanostructured gold film on a thin polystyrene film at room temperature. The morphological changes of the gold film were traced by carrying out time-resolved *in-situ* GISAXS measurements during the deposition process. The patterns of the scattered X-rays were used to calculate the number density of clusters, the heights and radii of the clusters, and the distances between clusters. The concept of the method has already been explained in Sec. 2.1.2, but the comparison between the experimental data and
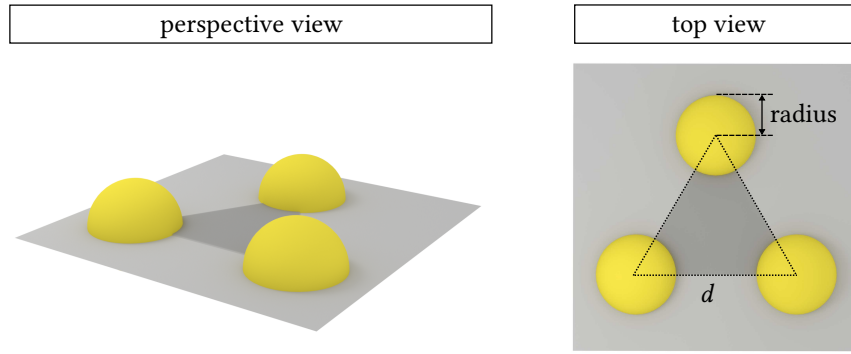
perspective view	top view

Figure 5.1.: Illustration of the geometrical model used in Refs. [32] and [61] for the fit to experimentally measured GISAXS data. The clusters are assumed to have a hemispherical shape and a hexagonal arrangement with distance d.

the simulation results in Sec. 5.4 will refer to specific details of the experiment; for clarity, these are briefly summarized in the following.

The deposition process of the thin gold layer took 1012 s, and the interval between subsequent GISAXS measurements was 0.1 s. Directly after the deposition, a measurement of the effective Au layer thickness yielded the value 8.31 nm. With this, an effective deposition rate of 0.49 nm/min was determined. Each recorded frame of scattering patterns in the q_y-q_z-plane (cf. Sec. 2.1.2) was separately evaluated to characterize the film morphology at specific points in time. The interparticle distance d was deduced from the position $q_{y,1,\max}$ of the first side peak in q_y-direction according to

$$d = \frac{2\pi}{q_{y,1,\max}} \ . \tag{5.1}$$

Assuming a local hexagonal arrangement of hemispheres for the cluster geometry, the radius of the clusters was calculated with the knowledge of d and the effective film thickness corresponding to the data under consideration. At the same time, the number density of clusters was extracted from size of the triangular unit cell. The heights of the clusters were determined in an independent procedure by fitting the parameters of a model system to the experimental data. For that purpose, the scattering patterns of hemispheres on a regular one-dimensional lattice were simulated, and the heights of the hemispheres were adjusted such that the minima in q_z-direction could be reproduced.

5.2. Simulation scheme

In the following, a comprehensive explanation of the simulation method is given. To ease the understanding, a graphical illustration of most aspects discussed throughout this section is given in Fig. 5.2.
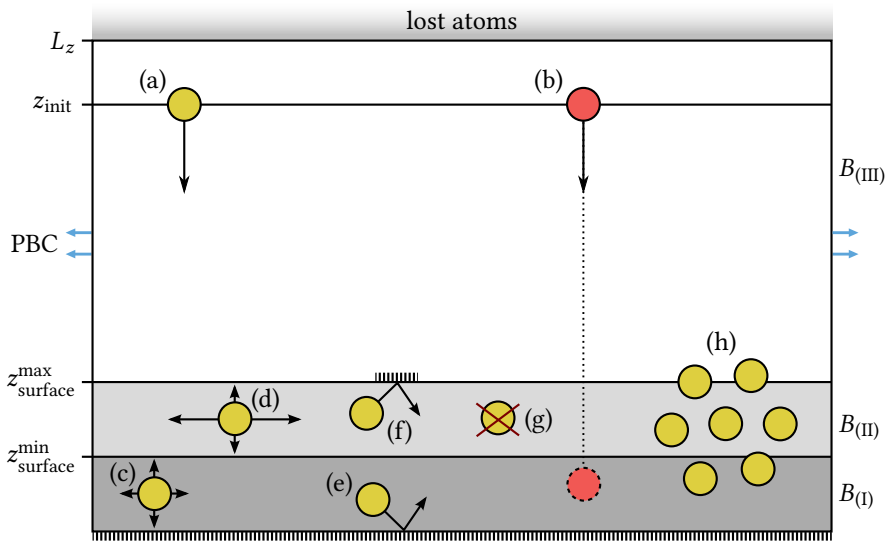
Figure 5.2.: Illustration of the partitioning of the simulation box and the atomic processes occurring in the simulations: deposition of an atom (a), deposition and implantation of an atom that represents a defect (b), diffusion in the bulk region $B_{(I)}$ (c), diffusion in the surface region $B_{(II)}$ (d), reflection of an atom at the bottom of the simulation box (e), reflection of a neighborless atom at the top of region $B_{(II)}$ (f), removal of an atom from region $B_{(II)}$ due to re-evaporation (g), formation of a cluster that extends over regions $B_{(I)}$, $B_{(II)}$ and $B_{(III)}$ (h). The label "PBC" indicates periodic boundary conditions for the lateral directions. When an atom crosses the boundary at the vertical position L_z—a very rare event—, it is removed from the simulation box. Adapted from [145].

Material constants of gold

As a preliminary remark, it is mentioned that the simulations require the atomic mass and the density of gold as input quantities. The respective values used in this work are m_{Au} = 196.97 u and ϱ_{Au} = 19.30 g/cm^3.

Partitioning of the simulation box

The motion of the atoms is restricted to a simulation box comprising all points in the set

$$B = \left\{(x, y, z) \,|\, 0 \leq x \leq L_x,\, 0 \leq y \leq L_y,\, 0 \leq z \leq L_z\right\} \,. \tag{5.2}$$

For the results in this work, L_x and L_y are always between 40 nm and 60 nm, and L_z always has the value 8 nm. To represent the upper part of the polymer bulk, the surface of the polymer and the area above the surface, the simulation box is partitioned into the three

respective subsets

$$B_{(I)} = \left\{ (x, y, z) \mid 0 \leq x \leq L_x, \, 0 \leq y \leq L_y, \, 0 \leq z < z_{surface}^{min} \right\} ,$$
$$B_{(II)} = \left\{ (x, y, z) \mid 0 \leq x \leq L_x, \, 0 \leq y \leq L_y, \, z_{surface}^{min} \leq z < z_{surface}^{max} \right\} , \qquad (5.3)$$
$$B_{(III)} = \left\{ (x, y, z) \mid 0 \leq x \leq L_x, \, 0 \leq y \leq L_y, \, z_{surface}^{max} \leq z \leq L_z \right\} .$$

The z-direction is thus defined to be perpendicular to the surface. By applying a different treatment of the atoms in each of the regions $B_{(I)}$ to $B_{(III)}$, it is possible to emulate the behavior of metal atoms at the polymer surface without the need of incorporating an explicit particle model for the polymer. Further details will be explained below.

Creation of atoms

Initially, no atoms exist in the system. When the simulation starts, new atoms are successively created at a random position in the plane at the height $z_{init} = 7$ nm. The choice of z_{init} has no particular meaning—in fact, the simulation results will not be different, if one sets z_{init} to any other value which is less than L_z and much larger than the expected cluster heights at the end of the simulation. The interval between successive creations of atoms is a constant time whose value is calculated from the pre-defined flux of atoms J_m^{sim}. The initial velocity of every created atom is set to $\mathbf{v}_{init} = (0, 0, -0.1 \, \text{nm/ps})$, i. e., the atoms approach the surface under an angle of $90°$.

Of course, this is a strongly simplified description of a real deposition process, for which one can expect different (and in particular broader) distributions of velocities and impact angles. However, these distributions are difficult to obtain, and even if accurate data was available for implementation, the following two points should be considered:

- A main assumption of the model is that most of the deposited atoms remain on the surface or slightly below it. It may therefore be impossible to adequately simulate the impact of very fast particles which are expected to penetrate into deeper regions of the polymer bulk. In contrast, for the impact of fast particles on metal clusters, a more appropriate description would be expected, but such a case would possibly require one to perform the simulations with significantly smaller time steps.

- As long as the distribution of impact angles remains relatively narrow and has a maximum at $90°$, no significant deviations from the current results with the fixed angle of $90°$ are expected. Nevertheless, it is known that the deposition under oblique angles may lead to interesting effects, e. g., due to the shadowing of certain areas on the surface (for example, see Refs. [146, 147]). So far, it has not been checked whether the simulation scheme has the ability to reproduce effects of that kind.

Equations of motion

The main idea for an implicit representation of the polymer surface is to perform Langevin dynamics with anisotropic forces in regions $B_{(I)}$ and $B_{(II)}$, and purely microscopic dynamics (without external forces) in region $B_{(III)}$. At the same time, the interatomic forces are governed

by the same potential U in all regions of the simulation box. In this case, the EAM potential for gold atoms provided by Foiles *et al.* [125] is used. In the following, we look more closely at the equations of motion, assuming that the system contains N_{m} atoms with the coordinates $\mathbf{r} = (\mathbf{r}_1, \mathbf{r}_2, \ldots, \mathbf{r}_N)$ and the masses $m_1, m_2, \ldots m_{N_{\mathrm{m}}}$. In the case of simulations with gold atoms, these masses are all set to the same value of m_{Au}.

In region $B_{(\mathrm{III})}$, which corresponds to the area above the surface, the atoms may only be influenced by other metal atoms; in particular, that means that the atoms remain unaffected by the presence of the polymer surface. The equation of motion for the three-dimensional spatial coordinate $\mathbf{r}_i$ of the i-th particle thus takes the simple form

$$m_i \ddot{\mathbf{r}}_i = \mathbf{F}_i(\mathbf{r}) \,, \tag{5.4}$$

where $\mathbf{F}_i$ is the interatomic force acting on the i-th particle at the position $\mathbf{r}_i$. This force is the derivative of the potential U with respect to the coordinates of the i-th atoms at the position $\mathbf{r}_i$,

$$\mathbf{F}_i = -\frac{\partial}{\partial \mathbf{r}_i} U(\mathbf{r}) \,. \tag{5.5}$$

In the other regions, the influence of the polymer is taken into account by generating a diffusive motion using Langevin dynamics. According to the explanations in Sec. 3.2.2, this is done by adding a friction term and a stochastic force to the equation of motion. In region $B_{(\mathrm{II})}$, the diffusion parallel to the surface, i.e., in x- and y-direction, should be faster than the diffusion perpendicular to the surface. For that purpose, the damping parameter $\tau_{\mathrm{surface}}^{\parallel}$ is used for both the x- and y-components of the forces, and another damping parameter, $\tau_{\mathrm{surface}}^{\perp} < \tau_{\mathrm{surface}}^{\parallel}$, is used for the z-component. Using the componentwise notations

$$\mathbf{r}_i = \begin{pmatrix} x_i \\ y_i \\ z_i \end{pmatrix} \qquad \text{and} \qquad \mathbf{F}_i(\mathbf{r}) = \begin{pmatrix} F_i^x(\mathbf{r}) \\ F_i^y(\mathbf{r}) \\ F_i^z(\mathbf{r}) \end{pmatrix} \,, \tag{5.6}$$

the equations of motion for the i-th particle in region $B_{(\mathrm{II})}$ thus take the form

$$m_i \ddot{x}_i = F_i^x - \frac{m_i}{\tau_{\mathrm{surface}}^{\parallel}} \dot{x}_i + \sqrt{\frac{2 m_i k_{\mathrm{B}} T}{\tau_{\mathrm{surface}}^{\parallel}}} R_i^x \,, \tag{5.7}$$

$$m_i \ddot{y}_i = F_i^y - \frac{m_i}{\tau_{\mathrm{surface}}^{\parallel}} \dot{y}_i + \sqrt{\frac{2 m_i k_{\mathrm{B}} T}{\tau_{\mathrm{surface}}^{\parallel}}} R_i^y \,, \tag{5.8}$$

$$m_i \ddot{z}_i = F_i^z - \frac{m_i}{\tau_{\mathrm{surface}}^{\perp}} \dot{z}_i + \sqrt{\frac{2 m_i k_{\mathrm{B}} T}{\tau_{\mathrm{surface}}^{\perp}}} R_i^z \,. \tag{5.9}$$

Here, R_i^x, R_i^y and R_i^z are independent uncorrelated Gaussian processes for each component. According to Eq. (3.9), the choice of the different damping parameters corresponds to two different diffusion coefficients,

$$D_{\mathrm{surface}}^{\parallel} = \frac{1}{m_i} k_{\mathrm{B}} T \tau_{\mathrm{surface}}^{\parallel} \qquad \text{and} \qquad D_{\mathrm{surface}}^{\perp} = \frac{1}{m_i} k_{\mathrm{B}} T \tau_{\mathrm{surface}}^{\perp} \,, \tag{5.10}$$

for the motion of freely diffusing atoms parallel to the surface and perpendicular to it.

In region $B_{(I)}$, which represents the upper part of the polymer bulk, the diffusion is intended to be isotropic, i. e., the damping parameter τ_{bulk} is the same for all directions. For the equation of motion, we can therefore use the vector notation again:

$$m_i \ddot{\mathbf{r}}_i = \mathbf{F}_i - \frac{m_i}{\tau_{bulk}} \dot{\mathbf{r}}_i + \sqrt{\frac{2m_i k_B T}{\tau_{bulk}}} \mathbf{R}_i .$$

(5.11)

In the following, we will assume that it is sufficient to set $\tau_{bulk} = \tau_{surface}^{\perp}$, and hence

$$D_{bulk} = \frac{1}{m_i} k_B T \tau_{bulk} = D_{surface}^{\perp} .$$

(5.12)

Further, we assume that a reasonable value of $\tau_{surface}^{\perp}$ has already been found (the choice of $\tau_{surface}^{\perp}$ will be discussed in Sec. 5.3 on the acceleration of the dynamics). For the determination of τ_{bulk} it is then practical to reintroduce the parameter $r_{s/b}$ first used in Eq. (4.13) and write

$$\tau_{bulk} = \frac{\tau_{surface}^{\|}}{r_{s/b}} .$$

(5.13)

While values of $r_{s/b}$ between 10 and 100 are estimated to fairly represent the previously discussed differences between surface and bulk diffusion coefficients, the simulations were performed with the fixed value $r_{s/b} = 80$. Nevertheless, just as is the case with KMC simulations, $r_{s/b}$ is a free parameter which may have to be adjusted to match the conditions of a specific experiment.

Detection of transitions between regions and neighborless atoms

For the application of the different equations of motion, the algorithm periodically reassigns all atoms to the regions. The time interval for this task, $t_{detect}^{regions}$, should be so small that delayed detections of transitions from one region into another have no significant effect on the simulation results.

Moreover, some of the mechanisms discussed below require the identification of atoms without neighbors. The condition for being neighborless is that no other atoms are located in the sphere with the radius r_{cut} around the center of the considered atom. For the results in this work, r_{cut} is set to the cut-off distance of the interaction potential. To save computation time, the neighbor analysis is not performed after each time step, but only after larger time intervals $t_{detect}^{neighbors}$ which should provide a compromise between computational efficiency and accuracy.

For the results in this work, both $t_{detect}^{regions}$ and $t_{detect}^{neighbors}$ are set to $300 \times \Delta t$, where Δt is the time step used for the integration. Hence, the check for transitions and the identification of neighborless atoms happen after every 300 steps.

Boundary conditions

Just as in the KMC simulations, periodic boundary conditions are applied to the directions parallel to the surface. As the interaction potential is cut off at a distance which is much less than L_x and L_y, the interaction with particles in a periodic image does not require any special effort.

The bottom plane of the simulation box is treated as a hard wall which reflects all incoming atoms. This is not only a practical solution to prevent atoms from escaping the simulation box, it also has the physical meaning that atoms cannot penetrate deeper into the polymer bulk. It is hence possible to keep the atoms close to the surface by choosing a relatively small value of $z_{\text{surface}}^{\min}$.

To prevent unbound atoms from escaping region $B_{(\text{II})}$ in an uncontrolled way, another hard wall is introduced at the top of region $B_{(\text{II})}$ at the height $z = z_{\text{surface}}^{\max}$. This wall only has an effect on atoms coming from below, i. e., starting at a position with $z < z_{\text{surface}}^{\max}$ at the previous time step—all atoms coming from above will pass through it. Furthermore, the wall only acts on atoms which are neighborless according to the above definition. As the motion of atoms belonging to a cluster remains unaffected, the formation of clusters which protrude beyond the surface region $B_{(\text{II})}$ is not restrained.

The necessity to implement such a mechanism that keeps the atoms in regions $B_{(\text{I})}$ and $B_{(\text{II})}$ arises from the implicit treatment of the polymer using Langevin dynamics: Due to the presence of stochastic forces, all metal atoms are permanently pushed in all directions; without any additional bonding mechanism, neighborless atoms could easily pass through the plane at $z_{\text{surface}}^{\max}$ and then move in a straight line until they reach the top of the simulation box. Even though the re-emission of atoms from the surface is a relevant process in real systems, it is unlikely that such a description relying on atoms randomly passing through the top of region $B_{(\text{II})}$— which is foremost an artifact of the partitioning of the simulation box—properly reflects the desorption behavior of a real system. The introduction of a hard wall effectively suppresses most of these unphysical events, but—as only neighborless atoms are affected by it—it is still possible that the stochastic forces push dimers or larger clusters away from the surface. This, however, happens only very rarely. In such a case, the atoms will move straight towards the top of the simulation box, and after crossing $z = L_z$, they are removed from the system.

Finally, as we can assume that most atoms will not accidentally leave the surface, another mechanism is required to model desorption. The solution used in this work will be explained in the next section.

Re-evaporation of atoms

The re-evaporation of atoms is modeled by a random process which successively attempts to remove every neighborless atoms from region $B_{(\text{II})}$ with the probability p_{re}. The process is repeated at a pre-defined time interval t_{re}. During each execution, a random number between 0 and 1 is drawn for each detected neighborless atom; if the number is below the probability p_{re}, the atom is immediately removed—otherwise, it remains at its current position. Hence, p_{re} is the average fraction of neighborless atoms that is removed each time the process is

called.

The idea to model the re-evaporation with a simple stochastic process was inspired by the similar procedure in KMC simulation model. Although the instantaneous removal of an atom can hardly approximate the real dynamics of a dissociating atom, we can use the process to model the influence of re-evaporating atoms on the net deposition rate: at the beginning of the deposition process, the density of metal atoms on the surface is so low that many atoms do not stick to it for a long time. Later, during the nucleation and growth of more and more clusters, the amount of re-evaporating atoms is continuously reduced.

Again, the drawback of such a simplified model is that it does not come without free parameters. In this case, t_{re} and p_{re} have been introduced and require careful adjustment. For the results in this work, a fixed value of $t_{\mathrm{re}} = t_{\mathrm{detect}}^{\mathrm{neighbors}}$ was used, but p_{re} was varied over several orders of magnitude.

Creation of defects

Due to the absence of explicitly modeled components of the polymer chains, it is clear that surface defects cannot be described on an accurate atomistic level. Nevertheless, we can again take up the idea of the KMC model that atoms and clusters are trapped when they come close to a defect. Roughly speaking, this is realized by making sure that some atoms become immobile when they reach the surface. As these atoms—which we simply call "defects" from now on—still interact with other mobile atoms, there is a high chance that a cluster is formed around them. More precisely, already during creation a pre-defined fraction of atoms is marked as a defect, but these defects will be treated like normal atoms as long as they approach the surface. However, they are always treated microscopically, i. e., without Langevin dynamics, until they eventually reach the lowest region $B_{(\mathrm{I})}$. Once a defect is detected in $B_{(\mathrm{I})}$, its position is fixed for the rest of the simulation.

Evidently, it is also possible that a defect never reaches the point where it becomes immobile, for example, if it is deposited on the top of a large cluster. This corresponds to the situation in an actual experiment when the metal film shelters the polymer from the impact of energetic particles. However, in such a case, re-sputtering of metal atoms might be observed in the experiment. In the simulations, this is very unlikely to happen because the energy of the defect is too small.

For the quantification of the influence of the defects, we will reuse the parameter γ from Eq. (4.8) with a slightly different meaning: here, γ denotes the fraction of deposited atoms which is treated as a defect according to the above description.

5.3. Acceleration of the dynamics: the rescaling method

As mentioned before, the MD simulation scheme was designed with the goal to recreate the conditions of the experiment by Schwartzkopf *et al.* [61] (or similar experiments) in a simulation. The relevant parameters of this experiment are the deposition rate $R^{\mathrm{exp}} = 0.49\,\mathrm{nm/min}$, the diffusion coefficient[1] $D^{\mathrm{exp}} = 7.33 \times 10^{-18}\,\mathrm{m^2/s}$ and the temperature $T^{\mathrm{exp}} =$

---

[1]The diffusion coefficient was obtained with the kinetic freezing model [84].
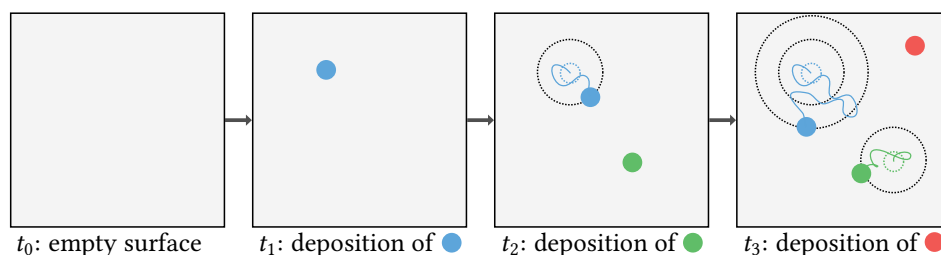
Figure 5.3.: Illustration of the idea used to accelerate the film growth dynamics. The surface is shown from the top at four different times. Starting with an empty surface at t_0, the green atom is deposited at t_1, the red atom at t_2 and the blue atom at t_3. The morphology of the resulting film will crucially depend on how far the particles move away from their origin during the time between successive depositions.

296 K. In Sec. 5.3.1, we discuss in detail how these parameters can be carried over to the simulations. We will see that this procedure leads to an effective acceleration of the growth dynamics. Subsequently, in Sec. 5.3.2, we continue with some remarks on several crucial aspects of the method.

5.3.1. Explanation of the method

In Sec. 3.2.4, it was already stated that the simulations must be performed with a sufficiently small time step. For this reason, we start by setting the time step to $\Delta t = 1$ fs to resolve the vibrations of atoms in clusters. With that, we can assume that it is hardly possible to find a larger time step which significantly reduces of the computation time and, at the same time, maintains the accuracy of the calculations. When we convert the deposition rate R^{exp} from the experiment to the flux of deposited atoms $J_{\text{m}}^{\text{exp}}$ using the density of gold, the large gap between the relevant time scales in experiments and the simulation times accessible with standard MD once more becomes evident: the average time between sequential depositions of atoms on an area of $1\,\text{nm}^2$ is 2 s. Although such a long time is far out of reach of simulations with a time step of 1 fs, we now make an attempt to map the slow dynamics of the experiment onto much shorter times which are within the scope of the present simulation scheme. In addition to the following explanations, an illustration of one of the central ideas is given in Fig. 5.3.

The basic assumption of this approach is that the film growth is essentially determined by *how far* the atoms travel on the surface during successive deposition events, but not *how long* that takes. If this is the case, the simulations can provide a realistic representation of the long-term behavior by setting the simulation parameters as follows: first, the temperature used in all Langevin equations is set to $T = T^{\text{exp}}$. Next, the damping parameter $\tau_{\text{surface}}^{\parallel}$ is set to an appropriate value—in this case, $\tau_{\text{surface}}^{\parallel} = 1$ ps—other values will be considered will be discussed in Sec. 6.1. The other damping parameter for the bulk diffusion, τ_{bulk}, is then calculated according to the ratio defined in Eq. (5.13). By fixing the temperature and the

damping parameters, at the same time, the diffusion coefficients $D_{\text{surface}}^{\parallel}$, $D_{\text{surface}}^{\perp}$ and D_{bulk} are determined according to Eqs. (5.10) and (5.12). With the knowledge of the diffusion coefficients, we can use Eq. (3.8) to calculate the mean squared displacement of a freely diffusing atoms in the simulations. Furthermore, the distance $l_{\parallel}^{\text{sim}}$ an atom moves away from its origin during a certain time t can be estimated by taking the square root of the mean squared displacement for the directions parallel to the surface,

$$l_{\parallel}^{\text{sim}}(t) = \sqrt{4 D_{\text{surface}}^{\parallel} t} \ . \tag{5.14}$$

In the following, we call the average time between successive depositions in the simulations $\Delta t_{\text{deposition}}^{\text{sim}}$. This time is proportional to the inverse of the particle flux,

$$\Delta t_{\text{deposition}}^{\text{sim}} \propto 1/J_{\text{m}}^{\text{sim}} \ . \tag{5.15}$$

For the corresponding distance, we introduce the notation

$$\tilde{l}^{\text{sim}} := l_{\parallel}^{\text{sim}} \left(\Delta t_{\text{deposition}}^{\text{sim}} \right) \ . \tag{5.16}$$

Now, we demand that this distance is the same as the distance $\tilde{l}^{\text{exp}}$ that the atoms travel during the waiting time $\Delta t_{\text{deposition}}^{\text{exp}}$ between successive depositions in the corresponding experiment. At this, $\Delta t_{\text{deposition}}^{\text{exp}}$ refers to a segment of the surface with the same area $L_x L_x$ as the surface area in the simulations. Assuming that we can express the mean traveled distance of an atom in the experiment analogously to Eq. (5.14),

$$l^{\text{exp}}(t) = \sqrt{4 D^{\text{exp}} t} \ , \tag{5.17}$$

the claim

$$\tilde{l}^{\text{sim}} = \tilde{l}^{\text{exp}} = l^{\text{exp}}(\Delta t_{\text{deposition}}^{\text{exp}}) \tag{5.18}$$

yields

$$\sqrt{4 D_{\text{surface}}^{\parallel} \Delta t_{\text{deposition}}^{\text{sim}}} = \sqrt{4 D^{\text{exp}} \Delta t_{\text{deposition}}^{\text{exp}}} \ . \tag{5.19}$$

Converting the experimental deposition rate R^{exp} to a corresponding flux of atoms $J_{\text{m}}^{\text{exp}}$, we arrive at the condition

$$\frac{D_{\text{surface}}^{\parallel}}{D^{\text{exp}}} = \frac{J_{\text{m}}^{\text{sim}}}{J_{\text{m}}^{\text{exp}}} =: \xi \ , \tag{5.20}$$

which allows us to determine the only missing parameter, the flux of atoms in the simulations $J_{\text{m}}^{\text{sim}}$.

Finally, we can use Eq. (5.20) to summarize the procedure to map the experimental growth dynamics to much shorter simulation times: After fixing the time step, the damping parameters and the temperature, a value for the flux $J_{\text{m}}^{\text{sim}}$ is chosen such that the simulations are performed with proportionally rescaled values of the deposition rate and the diffusion coefficient of the experiment. Thereby, the growth dynamics are effectively accelerated by the boost factor ξ which has been introduced in Eq. (5.20). In this case, the above defined values of the parameters yield the scaling factor $\xi = 1.7 \times 10^9$. This implies that the waiting time between

successive depositions on an area with the size $1\,\mathrm{nm}^2$ is only $1.2\,\mathrm{ns}$ in the simulations. This time differs from the above discussed experimental value of $2\,\mathrm{s}$ by 9 orders of magnitude. At the same time, we find that it only takes $20\,\mathrm{ps}$ for the mean displacement $l_\parallel^\mathrm{sim}$ to reach $1\,\mathrm{nm}$ in the simulations, but $0.03\,\mathrm{s}$ for the experimental counterpart l^exp defined in Eq. (5.17).

5.3.2. Remarks on the procedure

The acceleration by a factor of $\sim10^9$ certainly constitutes a drastic modification of the dynamics that one would expect in an actual experiment. While clear criteria exist for the applicability of the other acceleration methods mentioned in Sec. Sec. 3.2.4, there is no rigorous mathematical proof for the correctness of the rescaling method presented above. Besides the rough approximation made by the implicit treatment of the polymer, the derivation of the acceleration method involves three critical points which we discuss in the following:

- For the diffusion, only unbound atoms are considered. However, it is known that that clusters diffuse more slowly than isolated atoms. It is unclear whether the size-dependence of the diffusion coefficients of clusters induced by the Langevin treatment correctly reflects the experimental behavior.

- While only the diffusion of atoms on the polymer surface is accelerated, all kinds of relaxation processes of clusters concerning their shape and internal structure remain unaffected by the acceleration. Hence, the method requires that during the time between sequential additions of atoms to a cluster, the relaxations make the same or at least a similar progress in the simulations and in the experiment. This is likely true for very small clusters, but not for larger clusters whose reordering involves many infrequent events, e. g., hops of atoms on the cluster surface. We can therefore assume that the acceleration method will generate artifacts in the film morphology whose significance will increase with the film thickness.

- In the derivation of the method, we ignored the fact the re-evaporation of atoms from the surface is another process which must be adapted to the time scales in the simulations. Assuming that one can properly describe the experimental behavior in terms of a re-evaporation rate, it would be reasonable to rescale this rate by the factor ξ as well. However, as no such quantity is available for the experiment discussed above, we only rescale the experimental values of D^exp and $J_\mathrm{m}^\mathrm{exp}$, and treat the re-evaporation probability as a free parameter.

Beyond that, another critical point may be that the resulting flux $J_\mathrm{m}^\mathrm{sim}$ in the simulations must be small enough that the agglomeration of atoms *above* the surface is very unlikely. It was checked that this is always the case for the results in this work.

Due to the complexity of the simulations and the model character of some processes, it is difficult to guess in advance at what point the method will fail to give an adequate representation of the dynamics one would observe in an actual experiment. For this reason, the method should be extensively tested against experimental data. In Sec. 5.5, this will be done by comparing with the experimental morphology data from Ref. [61]. In addition to this, a complementary analysis of the main assumptions is given in Chapter 6.
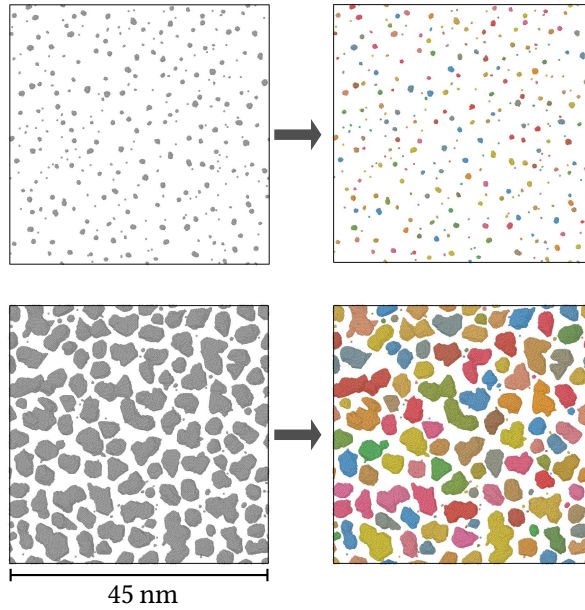
45 nm

Figure 5.4.: Exemplary decomposition of two configurations of atoms into clusters. The right images demonstrate the results from performing the identification of clusters in the configurations shown on the left. All atoms belonging to the same cluster have the same color. The data of these examples have been taken from actual simulation results discussed in Sec. 5.5.

5.4. Evaluation of simulation results

During a simulation run, the positions of all atoms are periodically stored in an output file. For the comparison with experimental results, it is necessary to condense this data to a reduced number of quantities with which one can characterize the morphology of the film. In the following, the definitions of the quantities used in this work are given.

Effective film thickness

For a comfortable comparison with experimental results, most of the MD simulation results in this work will be shown as a function of the effective film thickness

$$\delta = \frac{N_{\mathrm{m}}}{L_x L_y \rho_{\mathrm{m}}} \, , \tag{5.21}$$

where N_{m} is the total number of metal atoms in the film and ρ_{m} is the literature value of the number density of the deposited material. According to this definition, the effective film thickness denotes the height of a rectangular metal film on an area of $L_x L_y$ containing N_{m} atoms which are homogeneously distributed with the density ρ_{m}.

Calculation of distances

For some of the subsequently explained routines, it is necessary to calculate the distance between two atoms. In some of those cases, specific distance functions are used which slightly differ from the tree-dimensional Euclidean metric.

The reason not to use the Euclidean metric is the fact that the simulations are carried out with periodic boundary conditions. Using the Euclidean metric, it might happen that a cluster which has partially crossed the boundaries of the simulation box and reappeared on one or more other sides of the box is not identified as one cluster, but two or more. This problem can be solved by introducing the distance $d(\mathbf{a}, \mathbf{b})$ between two points $\mathbf{a} = (a_1, a_2, a_3)$ and $\mathbf{b} = (b_1, b_2, b_3)$ which is the minimum of the Euclidean distance between $\mathbf{a}$ and $\mathbf{b}$ and the Euclidean distances associated to all combinations of $\mathbf{a}$ and the points corresponding to $\mathbf{b}$ in the eight adjacent periodic images. Mathematically, this definition can be expressed as follows:

$$d(\mathbf{a}, \mathbf{b}) = \min \left\{ \left(\sum_{i=1}^{3} (a_i - (b_i + \beta_i L_i))^2 \right)^{-1/2} \bigg| \beta_1, \beta_2 \in \{-1, 0, 1\}, \beta_3 = 0 \right\}, \quad (5.22)$$

with $L_{1/2/3} := L_{x/y/z}$.

Another distance function is required if only the projection of the distance vector on a plane parallel to the surface is of interest. For that purpose, we define a similar function,

$$d_{\parallel}(\mathbf{a}, \mathbf{b}) = \min \left\{ \left(\sum_{i=1}^{2} (a_i - (b_i + \beta_i L_i))^2 \right)^{-1/2} \bigg| \beta_1, \beta_2 \in \{-1, 0, 1\} \right\}, \quad (5.23)$$

which only involves the first two components of the vectors $\mathbf{a}$ and $\mathbf{b}$.

Number density of clusters

The number density of clusters, n_c, which we will simply call "density of clusters" from now on, is the total number N_c of clusters existing on a surface divided by the area of the surface $L_x L_y$. In order to be able to count the clusters, they must first be identified as such. For that purpose, we define a cluster as a set of particles which is disconnected from any other clusters and cannot be decomposed into smaller clusters. Furthermore, the minimum number of atoms in a cluster is defined to be two. An atom belongs to a cluster if the above defined distance d between the atom and at least one atom in the cluster is below a critical distance r_{cut}. If an atom has no neighbors within the distance r_{cut}, it is identified as an isolated atom, but it will not be counted as a cluster.

For the choice of r_{cut}, it is reasonable to use a value between the nearest neighbor distance and the next-nearest neighbor distance associated to the crystal lattice structure of employed material in the solid state. For the results in this work, $r_{cut} = 0.32\,\text{nm}$ is used. With this value, a reliable identification of clusters during all stages of the growth is possible. It has been checked that one can slightly alter r_{cut} by roughly $\pm 0.05\,\text{nm}$ without significant modification of the results. Two examples of identified cluster structures occurring in actual simulation results are shown in Fig. 5.4.

Cluster radius

The clusters occurring in the simulations exhibit a multitude of different shapes, which may strongly deviate from simple geometric bodies with a high a degree of symmetry. Nevertheless, for the comparison with the experiment, it is useful characterize the spatial dimensions of the cluster shapes with just a few quantities. Therefore, we define a function R_{cluster} to measure how much a cluster C extends over the surface:

$$R_{\text{cluster}}(C) = \max\left\{ d_{\parallel}\left(\mathbf{r}_{\text{center}}(C), \mathbf{r}_i\right) \,\Big|\, \text{atom } i \text{ belongs to } C \right\}. \tag{5.24}$$

This function picks the maximum of all planar distances $d_{\parallel}$ between cluster atoms with coordinates $\mathbf{r}_i$ and the geometric center of the cluster, $\mathbf{r}_{\text{center}}(C)$. For the calculation of $\mathbf{r}_{\text{center}}(C)$, it is again necessary to take the periodic boundary conditions into account. For the results in this work, this is accomplished with the method described in Ref. [148].

With the above definition, R_{cluster} only has a clear meaning if the area of the cluster shape in the projection to a plane parallel to the surface is close to the area of a circle with the radius R_{cluster}. If this is the case, R_{cluster} has the meaning of a cluster radius. However, for clusters with highly asymmetric shapes, which occur, for example, as a result of the branching of a few small islands, R_{cluster} is just a vague indicator of how much space on the surface is covered by the cluster. Despite this restriction, R_{cluster} will be simply called "cluster radius" from now on.

Cluster height

In contrast to the cluster radii, the cluster heights are not calculated individually for each cluster. Instead, a quantity labeled h is extracted from the distribution of the z-coordinates off all atoms in the film. Namely, h is defined to be the length for which the number of cluster atoms with z-coordinates between z_{min} (the z-coordinate of the lowest atom in the film) and $z_{\text{min}} + h$ is equal to a fraction $f_h \leq 1$ of the total number of atoms in the film. As even larger clusters usually have an uneven surface at the top, one might want to compensate for protruding atoms by choosing a value of f_h which is slightly below 1. In fact, the cluster heights shown in this work are always calculated with $f_h = 0.99$, but it has been checked that the dependence of the cluster height on the effective film thickness is similar for any value of $f_h \gtrsim 0.9$.

Distance between clusters

The cluster distances presented in Ref. [61] refer to the distance between the centers of adjacent clusters. For the simulation results, a similar quantity can be estimated as follows: assuming that the clusters are nearly uniformly distributed on the film and have nearly the same sizes, the mean distance between the clusters can be calculated by

$$d_{\text{c}} = \sqrt{\frac{L_x L_y}{N_{\text{c}}}} = n_{\text{c}}^{-1/2}. \tag{5.25}$$

Using this definition, the mean cluster distance is exclusively determined by the density of clusters n_{c} and hence does not contain any information which is independent of n_{c}. Nev-
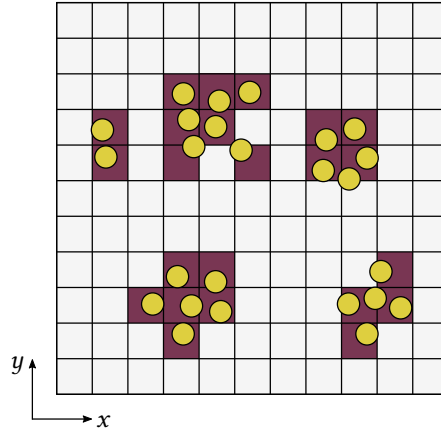
Figure 5.5.: Illustration of the method to calculate the surface coverage. Each square represents a unique set of x- and y-coordinates on the surface. A square is defined to be covered (indicated by the purple color) if the x- and y-coordinates of the center of at least one atom are within it. In this example, the coverage is $23/121 \approx 19.0\,\%$.

ertheless, in order to characterize the film morphology and make comparisons with the experiments, both n_c and d_c will be shown in the results sections.

Surface coverage

The surface coverage, i. e., the fraction of the polymer surface which is covered with metal atoms, is calculated with the following binning procedure. An illustration of this method is given in Fig. 5.5.

First, the surface is divided into equal-sized squares. Each of these squares is defined to be covered with metal if the x- and y-coordinates of at least one metal atom belong to the area enclosed by the square. Finally, the surface coverage is the number of covered squares divided by the total number of squares.

The resulting number of this method is only meaningful if the edge length $l_\square$ of the squares has a reasonable value. If it is too big, the coverage will be overestimated because the resolution is too low; if it is too small, even a completely covered film will have a surface coverage below one because not all squares are covered. As a solution to this problem, the edge length is set half the value of the crystal lattice constant of gold, i. e., $l_\square = a_\mathrm{Au}/2 = 0.204\,\mathrm{nm}$.

5.5. Simulation results

In this section, we discuss the results that have been obtained with the present simulation scheme. All of the results in this chapter were obtained with surface sizes of $L_x = L_y = 45\,\mathrm{nm}$. For the comparison with experimental results, the temperature T, the damping parameters $\tau_\mathrm{surface}^{\parallel/\perp}$ and the flux of atoms to the surface $J_\mathrm{m}^\mathrm{sim}$ were set according to the rescaling method introduced in Sec. 5.3. The fraction of defects γ and the re-evaporation probability p_re were

varied over several orders of magnitude; all other parameters were set to the previously mentioned values.

In Secs. 5.5.1 and 5.5.2, we start with some general remarks and compare the results from a selected simulation run with experimental data to justify the approach and work out some key aspects of the film growth. After that, in Sec. 5.5.3, we investigate the influence of defects and re-evaporation on the basis of a parameter study. In Sec. 5.5.4, we go beyond the fixed combination of $\tau_{\text{surface}}^{\parallel/\perp}$ and $J_{\text{m}}^{\text{sim}}$ by studying the effect of a variation of the deposition rate. Finally, in Sec. 5.5.5, a method is proposed to calculate the intensity of X-rays which are scattered on the simulated structures.

5.5.1. Preliminary remarks

Most of the simulation results cover film thicknesses up to roughly 1 nm. The range of thicknesses between 0 and 1 nm is relatively small compared to the experimentally investigated film thicknesses in Ref. [61] reaching 8.31 nm. Nevertheless, it already covers some of the characteristic changes of the film morphology. Furthermore, several longer simulation runs film thicknesses of roughly 3 nm were also performed to explore the limitations of the method. The results of one of these long runs will be used in Sec. 5.5.2 to describe the typical changes the film morphology undergoes during film growth, make a basic comparison with the experimental results from Ref. [61], and make a first estimation when the simulation method reaches its limit of applicability.

Remarks on Figs. 5.6 and 5.7. All quantities discussed in Sec. 5.5.2 are shown in Fig. 5.6. In addition to this, a visualization of the film growth simulated with the mentioned parameters is provided by Fig. 5.7, where the system configurations are shown from the top and in an auxiliary view for five different values of δ. A color gradient is used to indicate the z-coordinates of all depicted atoms. Furthermore, to complement the quantitative comparison, the left column of Fig. 5.7 also shows an illustration of the hexagonally arranged clusters used for the fit of the GISAXS data. This illustration has the the same scale and the same surface size as the simulated structures in the second column. As the clusters are shown from the top, they appear as circles. The parameters used for the radii of the circles have been taken from the data for the radius shown in Fig. 5.6b. The radial color gradients used to fill the circles represent an increase of the surface height from zero to the maximum which has been extracted from the data for the cluster height shown in Fig. 5.6c.

Time dependence of the effective film thickness. The quantity δ, which we use to characterize the evolution of the film morphology, roughly indicates how much time has passed since the starting point of the deposition. However, even if the interval between successive depositions of atoms is constant, δ will be a non-monotonous function of the deposition time. The reason is that each re-evaporation of an atom leads to a reduction of δ. As the amount of re-evaporated atoms per unit time changes with the coverage of the film, it is difficult to guess the time-dependence of δ in advance.

For example, in a simulations with the parameters $\gamma = 1 \times 10^{-2}$ and $p_{\text{re}} = 1 \times 10^{-1}$, it takes a direct MD simulation time of 78 ns to deposit the first 0.5 nanometers, but only 42 ns to

deposit the second 0.5 nanometers. In contrast, with the same parameter $\gamma = 1 \times 10^{-2}$, but a smaller re-evaporation probability, $p_{\mathrm{re}} = 1 \times 10^{-4}$, the deposition is much faster and it takes nearly the same amount of time to deposit the first two 0.5 nanometers, namely, 36.5 ns and 36.0 ns.

Computation time. It has already been pointed out in Sec. 3.2.3, that the asymptotic scaling of the computation time is $O(N_{\mathrm{m}})$. Beyond that, it is impossible to make an exact statement about the required computation time of the growth simulation because it depends on the employed hardware and a multitude of simulation parameters. Furthermore, the number of evaluations of interparticle forces will increase with the effective film thickness. That means that, the more atoms are deposited, the more computation time is needed to propagate the system in time. Nevertheless, to indicate the order of magnitude of typical computation times, we note that the simulation run discussed in Sec. 5.5.2 took a couple of days on approximately 1000 CPU cores. The hardware for this run was provided by HLRN.

5.5.2. General properties of the film morphology

In this section, we use the morphology data from a simulation run with the parameters $\gamma = 1 \times 10^{-2}$ and $p_{\mathrm{re}} = 1 \times 10^{-4}$ as an example to describe the general behavior one observes in the simulations of Au film growth. The values of γ and p_{re} were chosen because they exhibit relatively close agreement with experimental results over broad ranges of film thickness. In following sections, we will discuss the evolution of each quantity shown in Fig. 5.6 one after another. For each quantity, we will first focus on the simulation results and then make a separate discussion of deviations from the experimental results.

Number density of clusters

We start by considering the number density of clusters n_{c} shown in Fig. 5.6a. When the deposition starts, no clusters are present on the surface, i.e., , $n_{\mathrm{c}}(\delta = 0) = 0$. After the deposition of the first atoms, n_{c} rapidly increases as dimers start to form. This mainly happens as a result of both random nucleation and preferred nucleation at defects; only rarely, atoms are deposited on top of another isolated atom on the surface.

As neighborless atoms do not contribute to n_{c}, the formation of dimers is in fact the only mechanism that leads to an increase of the number density of clusters; all other growth events either leave it unchanged or lead to a reduction of n_{c}. Of particular importance is the coalescence of two clusters, which reduces the total number of clusters by one. As the probability for the coalescence of two clusters increases with n_{c}, it can be expected that the growing film eventually reaches a point where there exist so many clusters on the surface that the coalescence process outweighs the formation of new clusters—the number density of clusters then starts to decrease. In the considered simulation, this point occurs when the film reaches the thickness $\delta \approx 0.05$ nm; the corresponding density then attains a global maximum. This maximum is followed by a monotonous decay reflecting the progressing agglomeration of clusters. Although new clusters can still be formed in the space between other clusters, the chance that they are quickly attached to other existing clusters is already so high that no

further increase of n_c is observed except for small fluctuations. The slope of the decaying part remains nearly constant until the thickness reaches the value $\delta \approx 2\,\text{nm}$. As a logarithmic scaling of the vertical axis is used, this shows that the decay can be approximated by an exponential function with the exponent δ and a constant base.

In the regime between $\delta = 2\,\text{nm}$ and $3\,\text{nm}$—maybe even earlier—noticeable fluctuations build up in the number density. The reason is that the total number of clusters in the simulation box, N_c, becomes so small that the formation of new clusters or coalescence of clusters lead to relatively big changes of N_c. As both mentioned processes are driven by random events, the fluctuations of n_c can be considered as random, too.

Despite the onset of fluctuations, one can also observe that the density starts to level off after the steady decay. This behavior hardly noticeable, but it can be expected because of the following two reasons. First, the agglomeration of clusters happens less frequently because the clusters are already so big that their restricted mobility has an effect. Second, the chance for the merging of two clusters is reduced because the total number of clusters is already relatively small.

Besides these physical reasons, another technical aspect becomes relevant in the regime $\delta > 2\,\text{nm}$, namely, the limitation of the simulation box. The larger a cluster becomes, the more likely it is that it is broken up into several parts at the boundaries of the simulation box. The algorithm explained in Sec. 5.4 consistently defines these parts as one cluster. When the cluster is sufficiently large, it may happen that a second connection of these parts is formed *within* the boundaries of the simulation box. Such an event, the formation of a cluster with an "infinite" size, is a pure artifact of the application of periodic boundary conditions. Even though it may actually happen in real systems that different branches of the same cluster join each other, we can expect that such a process occurs with an increased probability in the simulations—in particular, if the clusters size is on the order of L_x and L_y or slightly lower. At the same time, it is therefore plausible that the system eventually reaches a point where the probability for the coalescence of two *different* clusters is lowered due to the limitations of the simulation box.

Comparison with experimental results. Both the simulation results and the experimental data show the same trends: the density rapidly attains a maximum after the deposition has started, then it slowly decays and, finally, it goes into saturation. Although the two curves in Fig. 5.6 show only small deviations over many values of δ, a few stronger deviations can be observed. This will be discussed in the following.

Even though the experimental data contains strong noise for small values of δ, it is apparent that both curves disagree about the position of the maximum cluster density. With the help of the fit shown in Appendix A, one may roughly estimate that the maximum of the experimental data occurs at $\delta \approx 0.17\,\text{nm}$—in the simulations, however, it already occurs at $\delta \approx 0.05\,\text{nm}$. Beyond that, the values of the maximum density are different, too, but the relative deviation is smaller: the experimental value is $n_c \approx 1.58 \times 10^{13}\,\text{cm}^{-2}$, and the value in the simulations is $n_c \approx 1.2 \times 10^{13}\,\text{cm}^{-2}$.

If we only make a direct quantitative comparison of the positions of the maxima, the simulations might appear to be inaccurate. Nevertheless, one should take into account that
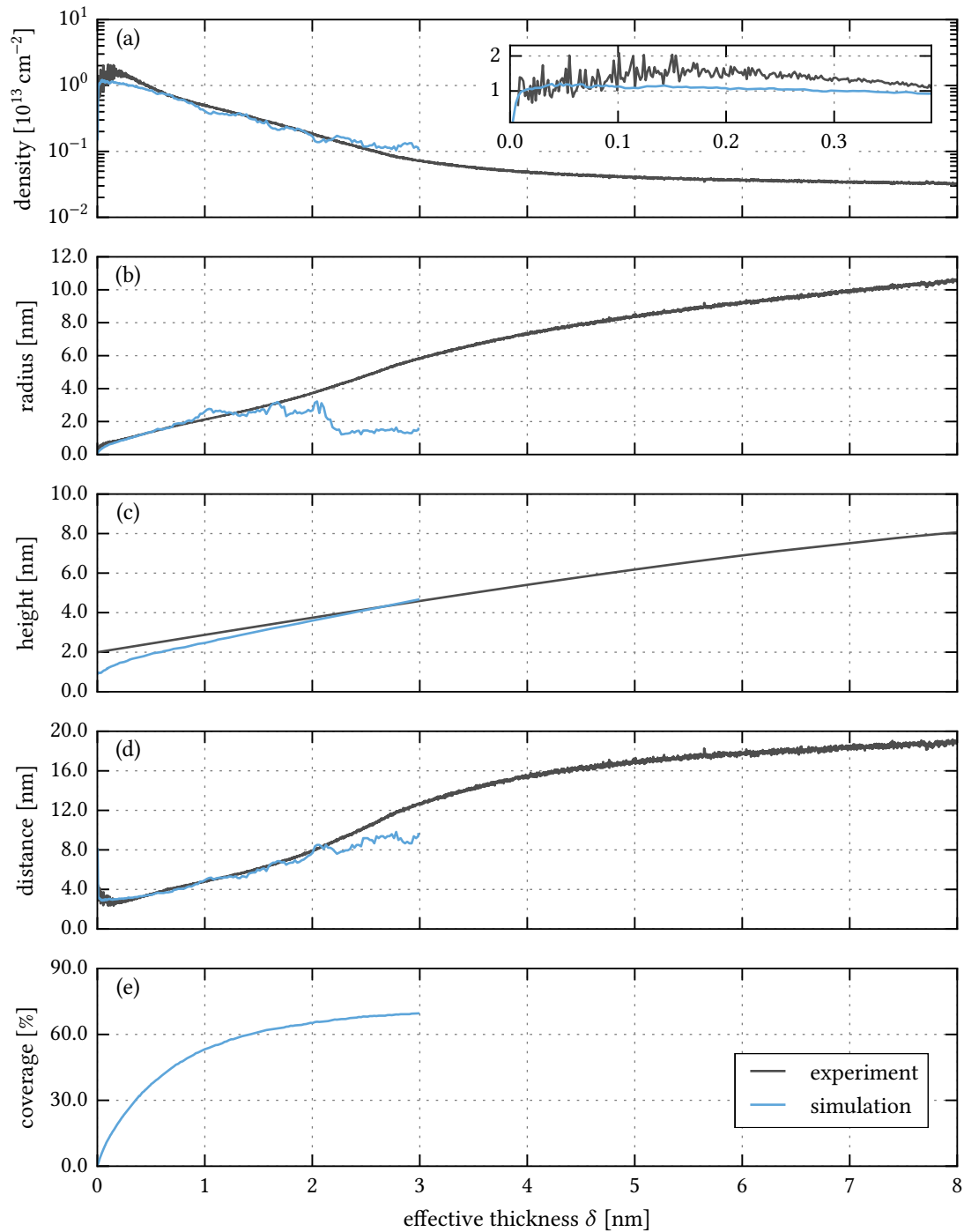
Figure 5.6.: Evolution of the film morphology as a function of the effective film thickness δ. The plots show the experimental data from Ref. [61] and the results from a selected simulation run with the parameters $\gamma = 1 \times 10^{-2}$ for the fraction of defects and $p_{\mathrm{re}} = 1 \times 10^{-4}$ for the re-evaporation probability probability. The inset in the first row is a zoom into the graph shown in (a), but with a linearly scaled vertical axis. Adapted from [145].
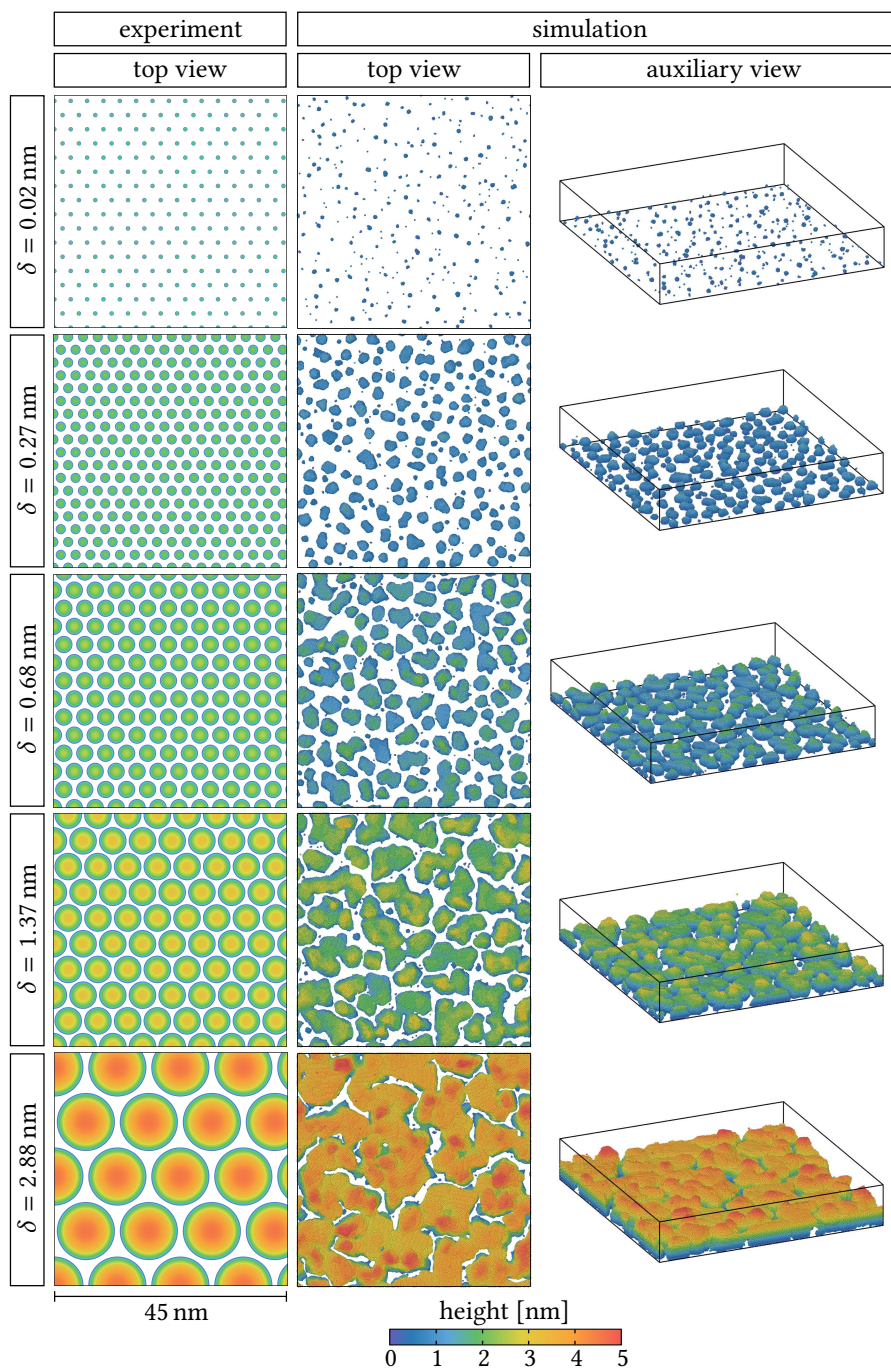
Figure 5.7.: Evolution of the Au film according to the hemispherical cluster model used for the experimental results in Ref. [61] (1st column) and a simulation with $\gamma = 1 \times 10^{-2}$ and $p_{\mathrm{re}} = 1 \times 10^{-4}$ (2nd and 3rd column). The radii and distances of the circles in the 1st column represent the values given in Figs. 5.6b and d for the corresponding values of δ. The colors of the circles represent the increase of the cluster heights until they reach their maximum values shown in Fig. 5.6c. For the simulation results, the colors indicate the z-coordinates of the atoms.

the agreement is much better for the decaying part—in particular, between $\delta = 0.5\,\text{nm}$ and $2\,\text{nm}$. While this part covers a large fraction of all simulated thicknesses, the maximum already occurs after the first $1.7\,\%$ of simulated δ-values. Thus, if the behavior of both curves is compared on a larger scale, the deviation of the maximum cluster densities is appears to be less substantial. In Sec. 5.5.3, we will see that a better agreement of the maxima can be achieved by varying the parameters δ and p_{re}—however, this will lead to greater deviations for other ranges of δ.

Cluster radii

In Fig. 5.6b, the δ-dependence of the cluster radius is shown. The curve represents the average of the cluster radii which have been calculated for each cluster according to the definition in Eq. (5.24).

For $\delta < 1\,\text{nm}$, the radius monotonously increases until it reaches approximately $2\,\text{nm}$. The slope of the curve has its largest value in the early phase of the nucleation. It becomes smaller and nearly constant around the δ-value of maximum cluster density. For $\delta \gtrsim 1\,\text{nm}$, the values exhibit increasingly strong fluctuations. These can be explained by the steadily decreasing total number of clusters which are involved in the averaging procedure. Furthermore, the simulation snapshots in Fig. 5.7 indicate that many clusters have already obtained a non-spherical shape. We can therefore expect that, with increasing film thickness, the values calculated with the present definition of the cluster radius can only be a rough indication of the actual lateral dimensions of the cluster. For $\delta \gtrsim 2\,\text{nm}$, it becomes particularly clear that the quantity is no longer useful for practical investigation of the film morphology: the value rapidly drops by roughly $2\,\text{nm}$, but the existing clusters do not become smaller. The reason for this drop is that all previously existing large clusters have merged and are thus counted as just one cluster. At the same time, however, various very small clusters are present in the space between the branches of the big cluster; the radii of those clusters enter in the averaging procedure with the same weight as the big cluster. Examples for the occurrence of small clusters alongside a few or just one big cluster can be found in the fourth and in the fifth row of Fig. 5.7.

It would certainly be possible to find another definition of the cluster radius that would not exhibit this drop. Nevertheless, this has not been done because, in the regime of the drop, which is characterized by the limitations of the simulation box and the existence of many clusters without a radial symmetry, it is meaningless to speak of an average cluster radius anyway. Instead, the drop of the cluster radius can be considered as an indicator that the limitations of the simulation become relevant.

Comparison with experimental results. For $\delta \lesssim 0.7\,\text{nm}$, it is hardly possible to make out any differences of both curves in Fig. 5.6b—merely at the beginning of the deposition, one can recognize that the experimental values of the radius are slightly higher. Compensating for the onset of fluctuations for larger values of δ, we may even assume that both systems behave similarly until the thickness reaches $1.5\,\text{nm}$.

While the fluctuations and the drop of the simulation data have already been explained, it remains to discuss why the experimentally obtained cluster radius continues to increase

monotonously. Therefore, we recall that the hemispherical cluster model is used throughout the whole range of thicknesses. That means that the experimental procedure cannot be hampered by any difficulties related to different particle shapes. Hence, the method always yields a value of the cluster radius, and it can be expected that it permanently increases as a consequence of the increasing amount of deposited atoms.

To conclude the analysis of the cluster radii, a final remark on the cluster size distribution is made in the following. For that purpose, it is again referred to Fig. 5.7 as the comparison between the monodisperse hemispherical model and the simulated structures with different shapes and sizes underlines the following reasoning.

The experimental fit relies on the assumption that the size distribution is monodisperse—even though it is not generally impossible to make a fit to GISAXS data with particles of different sizes. For this reason, the occurrence of branched structures can only be related to the point when the hemispheres start to intersect each other. However, this point—which the authors of Ref. [61] has identified as the percolation threshold—occurs not before 5.2 nm and is thus out of reach of the current scope of the simulations. Despite the agreement of the average cluster radii, the incapability of the method used in Ref. [61] to describe the distributions of cluster sizes and shapes makes it difficult to judge the quality of the simulations in full detail. With additional reference data for the evolution of cluster shapes, the assumptions of the acceleration method could be checked more precisely. While the rescaling procedure only affects the diffusion of atoms and clusters but no internal cluster relaxation processes, it remains unclear to what degree the neglect of the latter processes has an effect on the simulation results. In fact, one can expect that the relevance of relaxation processes increases with the film thickness because larger clusters need more time to transform their shape, e. g., by diffusion processes on the cluster surface. With the currently available reference data, however, a quantitative comparison of the film morphology can only be made with the averaged quantities shown in Fig. 5.6.

Cluster heights

The evolution of the cluster height is shown in Fig. 5.6c. The curve exhibits a monotonous increase that is very similar to the behavior of the cluster radius, but it is almost free of fluctuations. In fact, one can expect that—except for the space between the clusters—a relatively even height profile of the film should evolve. This can be understood as follows: the more parts of the surface are covered with gold, the more atoms are deposited on top of the clusters. Once the clusters are sufficiently large, the most frequent growth event is the direct deposition of atoms on top of existing clusters. As the flux of deposited atoms is isotropic, the roughness of the surface at the top of each cluster should be low compared to the total height of the clusters. Indeed, the distribution of the colors in Fig. 5.7 confirms this trend.

At the end of the simulation, the height reaches a value of 4.7 nm. The fact that this value is much higher than the corresponding effective film thickness of 3 nm shows that the film still exhibits a significant amount of space between the clusters.

Comparison with experimental results. For very small values values of δ, the experimentally obtained cluster heights are roughly two times as large as the simulated values.

Concerning this discrepancy, we may assume that the experimental values are too large because it is unlikely that the cluster height is 2 nm right after the beginning of the deposition process. A reason for the occurrence of too large cluster heights might be the fact that all depicted experimental values below $\delta < 0.38$ nm stem from an extrapolation procedure, see Ref. [61] for further details. At the same time, we also note that the simulation data is probably also too large at the beginning because the employed quantity defined in Sec. 5.4 does not compensate for fluctuations of the vertical cluster positions.

For larger values of δ, the difference between the curves steadily vanishes until the film reaches a thickness of 2.5 nm. Then, however, the simulation results even become slightly larger. If we just extrapolate the simulation data with the nearly constant slope in the range between $\delta = 2$ nm and $\delta = 3$ nm, we may expect that the deviations between both curves would increase if we performed longer simulations. However, we cannot resolve this with the present data.

Distances between clusters

The δ-dependence of the particle distances is shown in Fig. 5.6d. While the quantitative values of the distances may be of interest, we can refrain from discussing specific characteristics of the curve because we have defined the considered quantity in Eq. (5.25) in a way that it is equal to the inverse of the square root of the density of clusters. That is to say that all discussed features and uncertainties of the density of clusters can be directly translated to the distance between the clusters. For the experimental results, there also exists a similar relation between the density and the distance. However, the authors of Ref. [61] first obtained the distance from the scattering patterns, and then used it to calculate the density. As a comprehensive comparison between the results for the density has already been made, we skip a similar analysis for the distance.

Surface coverage

The surface coverage shown in Fig. 5.6e monotonously increases from zero to the final value of 70 %. The curve has the shape of a concave function, which reflects that the increase of the coverage becomes smaller the more parts of the surface are already covered. As the re-evaporation probability remains constant during the simulations, no deviations from the monotonous behavior are expected.

Comparison with experimental results. For the surface coverage, no experimental data is available in Ref. [61]. Nevertheless, we can at least find that the shape of the curve is similar to the corresponding curve shown in Ref. [32], where the deposition of gold on a silicon oxide layer was studied; in that work, the coverage increases to approximately 80 % at an effective thickness of 3 nm, and then proceeds more slowly to 100 % at $\delta \approx 9$ nm.

5.5.3. Influence of defects and re-evaporation

In this section, we turn towards the influence of the fraction of deposited defects, γ, and the re-evaporation probability, p_{re}. While both parameters affect the sticking of atoms to
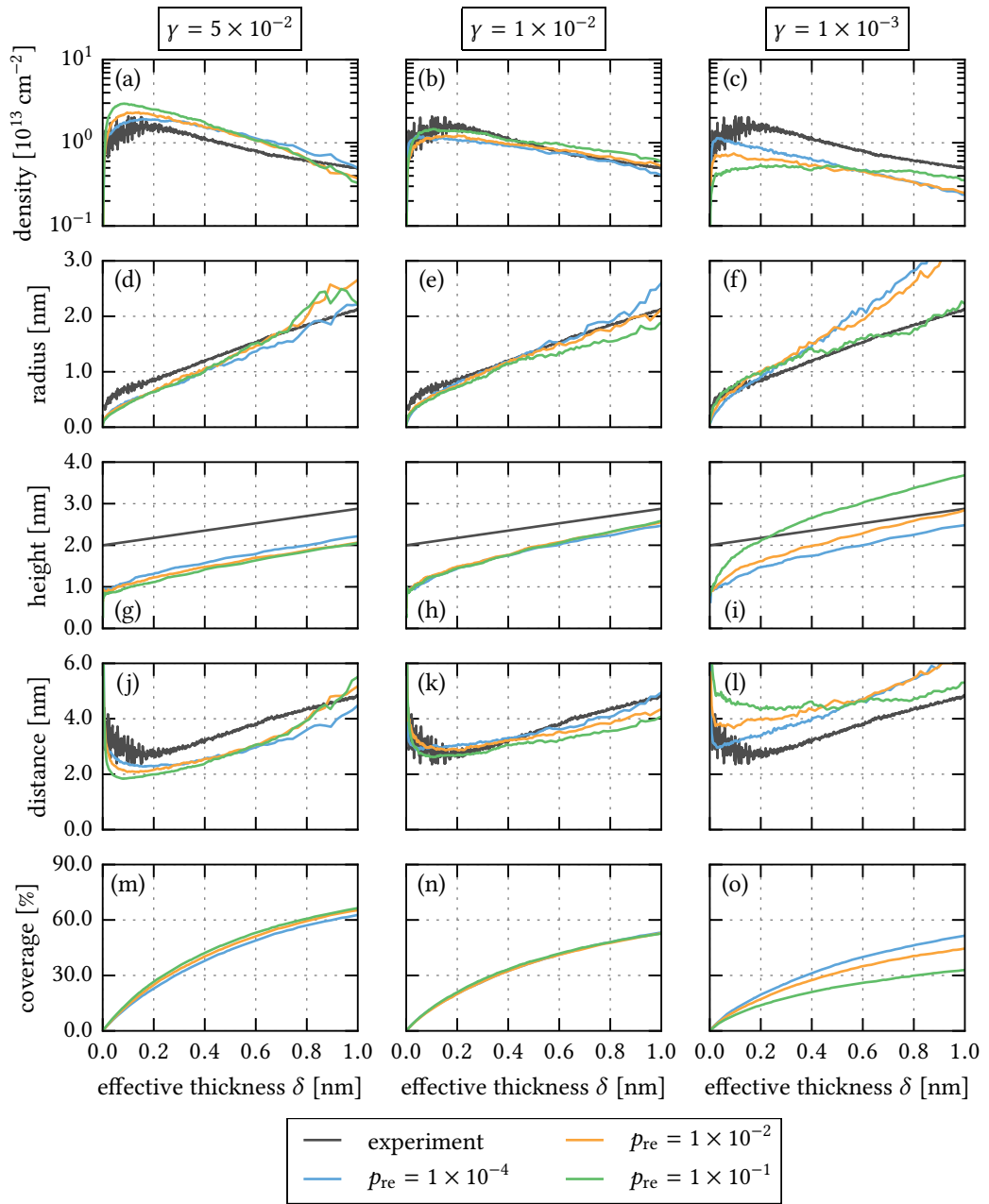
Figure 5.8.: Evolution of the number density of clusters, the cluster radius, the cluster height, the distance between adjacent clusters and the surface coverage as a function of the effective film thickness δ. Each column shows the results of the calculations with a fixed fraction of defects γ, but three different re-evaporation probabilities p_{re}. For comparison, the experimental data from Ref. [61] is also shown. Adapted from [145].

the surface, γ also has an effect on the mobility of atoms and clusters on the surface. It is thus reasonable to consider both parameters in a joint parameter study. The analysis is limited to the range of effective thicknesses between zero and 1 nm. This range covers the non-monotonic behavior of the cluster density and the first stage of its decay. Beyond that, the fluctuations are still small enough to make reliable quantitative comparisons.

In the following, we refer to the simulation results shown in Fig. 5.8. This figure shows the same morphological quantities as Fig. 5.6, but three columns are used to represent different values of γ. For each γ, namely $\gamma = 5 \times 10^{-2}$, 1×10^{-2} and 1×10^{-3}, the data for the re-evaporation probabilities $p_{re} = 1 \times 10^{-4}$, 1×10^{-2} and 1×10^{-1} is shown. Furthermore, the experimental data from Ref. [61] is shown again to allow for additional comparisons. For all employed combinations of γ and p_{re}, the behavior of the morphological parameters is qualitatively the same as discussed in the previous section. We may therefore skip a discussion of the general trends and proceed by investigating the influence of γ and p_{re} in detail.

To begin with, we only describe the influence of the defects, i.e., we first ignore any additional effects caused by a variation of p_{re}. Nevertheless, we remark that the following aspects are particular noticeable for the largest re-evaporation probability $p_{re} = 1 \times 10^{-1}$. Considering the peak position of the density of clusters shown in the first row of Fig. 5.8, we find that a reduction of γ leads to an increase of the maximum density and a shift of the peak position to larger values of the effective film thickness. At the same time, the cluster radii and cluster heights shown in the second and third row reveal that this trend comes along with an increase of the cluster size. When we look at the coverage of the surface shown in the fifth row, we find that the increased particle size does not compensate for the decreased density: the reduction of γ leads to a decrease of the coverage. Finally, the just described trends can also be observed in Fig. 5.9, where the film morphology of two simulation runs with different values of γ is shown for two selected values of the effective thickness.

The dependence on the fraction of deposited defects can be understood by recapitulating that the defects not only impel the preferred nucleation of clusters, but also make clusters adhere to the point where they have nucleated. That means that a large number of defects is related to many small clusters whose coalescence is primarily caused by lateral attachments of atoms. When a smaller amount of defects is present on the surface, clusters are mainly formed by random nucleation. The increased mobility of the clusters promotes their agglomeration as a result of their diffusion on the surface. Furthermore, when the number of defects is low, there is a high chance that neighborless atoms re-evaporate before they are attached to another cluster. Hence, a relatively large fraction of atoms in the system has been directly deposited on top of already existing clusters. This explains the observation of larger cluster heights.

Now we extend the analysis by taking the re-evaporation probabilities into account. First, we concentrate on the density of clusters in the range of effective thicknesses in which the maximum can be located. It turns out that the dependence on p_{re} for $\gamma = 1 \times 10^{-3}$ is reversed to the dependence for $\gamma = 5 \times 10^{-2}$. The reversal of these trends takes place around $\gamma = 1 \times 10^{-2}$. To understand this behavior, let us first assume that both the number of defects and the re-evaporation probability are large. In this case, many clusters nucleate in the vicinity of a defect, but the formation of connections between these clusters is aggravated. If we keep the same value of γ, but we decrease p_{re}, connections between the clusters are

formed more easily, and, thus, the maximum density of clusters becomes lower. This behavior can be observed in Fig. 5.8a. For a much lower number of defects, we find the opposite: if p_{re} is high, only a small fraction of all deposited atoms sticks to the surface, and the formation of clusters is strongly hampered. As a result of this, the density of clusters remains very low. Yet, it can be increased by raising p_{re}—this is the behavior that we find for $\gamma = 1 \times 10^{-3}$ in Fig. 5.8c.

So far, we restricted the consideration of the p_{re}-dependence to the regime around the maximum density of clusters. In fact, the above described trends do not hold for larger values of δ: despite the onset of weak fluctuations, we find intersections of the curves near $\delta = 0.6\,\text{nm}$. The present results do not allow a detailed analysis, but we can roughly state that the larger the maximum of the density of clusters is, the steeper is its subsequent decay.

Besides those trends of the density of clusters, we find again that the cluster sizes—described by the radii and the heights—are closely related to the density of clusters: similarly to what we stated about the dependence on γ, the clusters are large when the density of clusters is low, and vice versa. However, this is not generally true as shown, for example, for $\delta \gtrsim 0.6\,\text{nm}$ in the third columns of Fig. 5.8: not only the largest densities of clusters occur for $p_{re} = 1 \times 10^{-1}$, but also the largest values of the cluster heights; only the cluster radii are minimal in that regime.

We conclude this analysis with a final remark on the comparison with the experimental results. For the detailed comparison in the previous section, we used the simulation results from a run with the parameters $\gamma = 1 \times 10^{-2}$ and $p_{re} = 1 \times 10^{-4}$ because the deviations of the results are relatively small. However, this statement mainly refers to the regime of effective thicknesses that covers the decaying part of the density of clusters. For other values of δ, some of the results obtained with other parameters show better agreement, see, for example, the maximum density of clusters for the parameters $\gamma = 1 \times 10^{-2}$ and $p_{re} = 1 \times 10^{-1}$. So far, no parameter set has been found that removes all discrepancies at once. With the currently available data, we can neither rule out that the experimental data is inaccurate nor that the simulation model is incomplete or flawed. However, the overall agreement is good enough to make it plausible that the conditions of the growth process described by the simulations are at least very similar to those in the experiment we compare with.

5.5.4. Influence of the deposition rate

We conclude the investigation of the morphology with a brief analysis the influence of the deposition rate. That means that we allow the deposition rate to be different from the value of $J_{\text{m}}^{\text{sim}}$ that we obtained with the rescaling method described in Sec. 5.3. For that purpose, we define a new flux of atoms to the surface $\tilde{J}_{\text{m}}^{\text{sim}}$ which we express as a multiple of the flux $J_{\text{m}}^{\text{sim}}$,

$$\tilde{J}_{\text{m}}^{\text{sim}} = \beta J_{\text{m}}^{\text{sim}} \ . \tag{5.26}$$

In Fig. 5.10 the film morphology data is shown that has been obtained in simulations with the same parameters $\gamma = 1 \times 10^{-2}$ and $p_{re} = 1 \times 10^{-4}$, but different value of β, namely $\beta = 0.5$, 1 and 30. The experimental data from Ref. [61] also shown to allow once more for comparison.

The curves for $\beta = 1$ have already been discussed—we will thus concentrate on the changes induced by using higher and lower deposition rates. For $\beta = 30$, the maximum density of
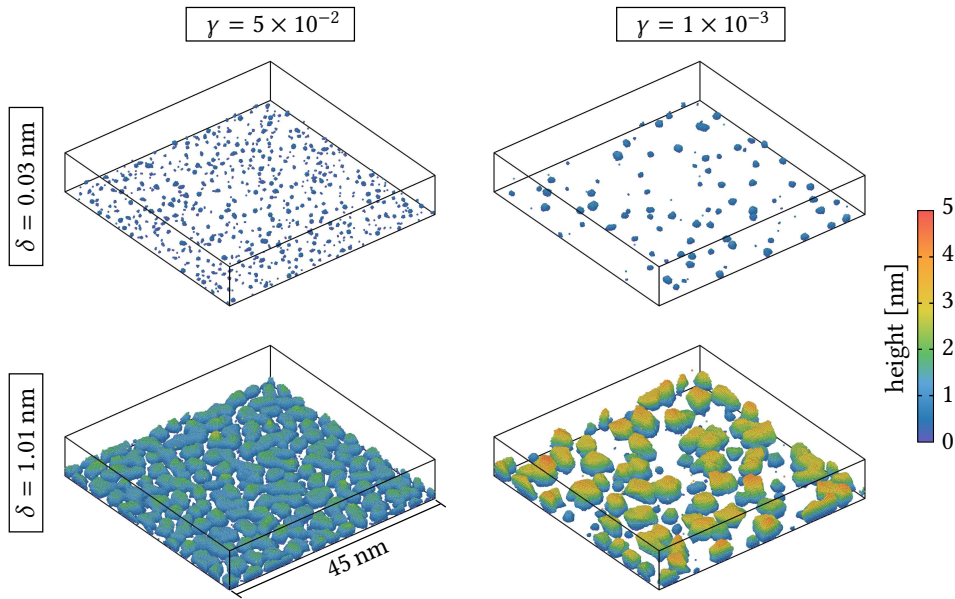
Figure 5.9.: Influence of the amount of defects on the film morphology. Both columns represent two different simulation runs with the same re-evaporation probability $p_{\text{re}} = 1 \times 10^{-1}$, but different fractions of defects, $\gamma = 5 \times 10^{-2}$ and $\gamma = 1 \times 10^{-3}$. Both configurations in each row correspond to the same effective film thickness δ.

clusters is more than three times larger than for $\beta = 1$, but the decaying part of the density has nearly the same slope. Again, we can find that an increase of the density leads to a decrease of the cluster size. This is clearly observable for the cluster radii—the cluster heights are only weakly affected. The fluctuations of the cluster radii indicate again the limitations of the simulation box between $\delta = 1\,\text{nm}$ and $\delta = 2\,\text{nm}$. Nevertheless, the simulation run has been continued until an effective thickness of $4.5\,\text{nm}$ was reached. As the computation time roughly scales with the inverse of the deposition rate, this run has only consumed a relatively small amount of time.

For $\beta = 0.5$, only a short period has been simulated because the computation time is very long. Since the deposition is slowed down, diffusion processes in the time between successive depositions of atoms become more important. The clusters thus have more time to undergo relaxation processes and agglomerate with other clusters. As a result of this, the density of clusters is slightly lowered as compared to the case $\beta = 1$, and the radii are larger. However, in contrast to some previously discussed cases, this does not come along with an elevation of the cluster heights—instead, the heights are even below the heights for $\beta = 30$.

So far, the influence of the deposition rate has not been studied in more detail. An experimental investigation has been carried out recently [149] for the sputter deposition of gold on a polystyrene film [149]. This investigation, which is an extension of the work presented in Ref. [61], confirms that an increase of the deposition rate leads to smaller particles and
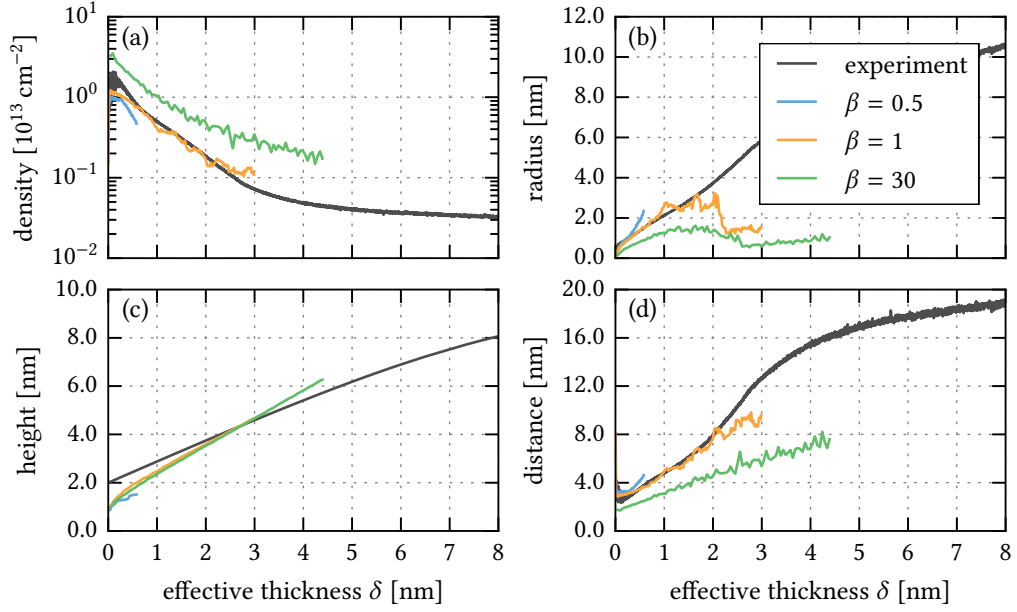
Figure 5.10.: Influence of the deposition rate on the film morphology. $\beta = \tilde{J}_{\mathrm{m}}^{\mathrm{sim}} / J_{\mathrm{m}}^{\mathrm{sim}}$ is the ratio of the flux of atoms to the surface used in the flux used for the results in Secs. 5.5.2 and 5.5.3. The experimental data is again from Ref. [61]. Adapted from [145].

higher densities. In the future, it might be of interest to extend the present simulation results and make a quantitative comparison.

5.5.5. X-ray scattering on clusters

In this section, we consider the possibility to calculate X-ray scattering patterns for the simulated film morphology. If we want use Eq. (2.3) to calculate the scattering cross section, we need to calculate the form factors F for all clusters. Remaining on the level of the Born approximation, the form factor of a cluster can be obtained from the Fourier transform of the shape functions, S. This idea is based on the assumption that the particle can be approximated by a continuous geometric shape that allows one to distinguish between the region inside the particle and the region outside. Thus, in order to use Eq. (2.4) to calculate the form factor of an atomistic cluster obtained in a simulations, it is necessary to construct a suitable geometric shape from the positions of the atoms. The volume of such a shape is supposed to contain all atoms of the corresponding cluster, and the surface of the shape must be aligned with the surface of the cluster. Furthermore, the cluster should be big enough that such a coarse and continuous description is justified. In the following, we examine one way to express the shape of a cluster in terms of adjacent rectangular cuboids. An illustration of the method is provided by Fig. 5.11.

We start with a procedure that is similar to the method described in Sec. 5.4 to calculate the
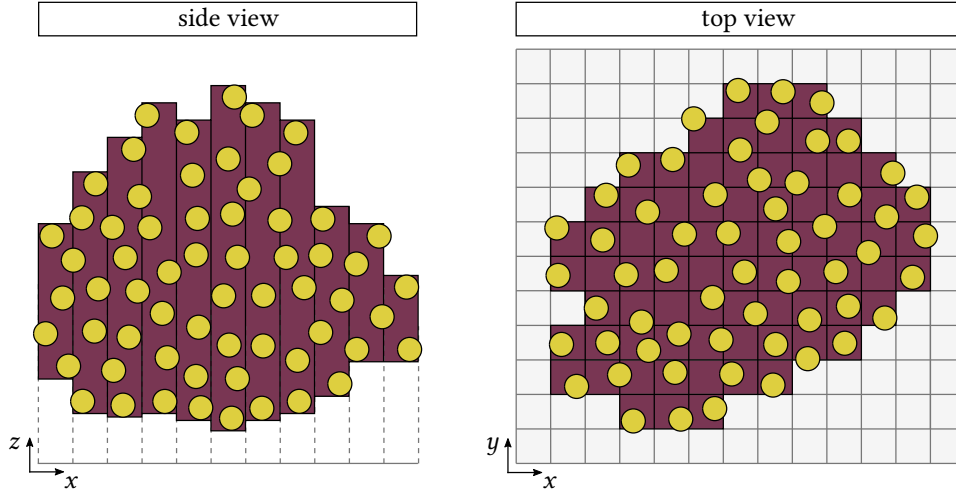
Figure 5.11.: Illustration of the binning procedure to represent the atoms of a cluster (yellow) with rectangular cuboids (purple).

surface coverage: at first, we construct a two-dimensional grid of squares in the x-y-plane, i. e., parallel to the surface. This grid will enable us to obtain a coarsened description of the lateral dimensions of the cluster. As a next step, we search for all grid cells which are covered by atoms of the clusters. More precisely, that means that the ranges of x- and y-values associated with the area of the cell contain the x- and y-coordinates of at least one atom of the cluster.

For each covered grid cell, we construct one rectangular cuboid which is supposed to approximate a defined part of the cluster. The top and bottom faces of the cuboid shall be parallely aligned with the grid cell, i. e., the other four faces shall be perpendicular to the surface. If we let z^{low} be the z-coordinate of the atom which is the lowest of all atoms that cover the cell under consideration, and we let z^{high} be the z-coordinate of the highest atom, we set the lower end of the cuboid to the height $z^{\text{low}} - r_{\text{atom}}$ and the upper end to $z^{\text{high}} + r_{\text{atom}}$. The additional parameter r_{atom} is supposed to account for the spatial extent of an atom. For the example discussed below, r_{atom} is set to $0.14\,\text{nm}$, which is on the order of a typical atomic radius. Nevertheless, the quantity r_{atom} does not have to be determined very accurately as long as the aforementioned assumption of sufficiently large cluster holds.

Assuming that the total number of cuboids is M and the k-th cuboid is represented by the set

$$\mathcal{S}_k = \left\{ (x, y, z) \mid x_k^{\text{min}} \leq x < x_k^{\text{max}}, y_k^{\text{min}} \leq y < y_k^{\text{max}}, z_k^{\text{min}} \leq z < z_k^{\text{max}} \right\}, \tag{5.27}$$

the shape function can be defined as

$$S(x, y, z) = \begin{cases} 1, & \text{if } (x, y, z) \in \bigcup_{k=1}^{M} \mathcal{S}_k \\ 0, & \text{otherwise} . \end{cases} \tag{5.28}$$

83

With this, we find the following analytical expression for the form factor:

$$
\begin{aligned}
F(q_x, q_y, q_z) &= \int_{-\infty}^{\infty} \int_{-\infty}^{\infty} \int_{-\infty}^{\infty} S(x, y, z) \exp\left(-i\left[q_x x + q_y y + q_z z\right]\right) \, dx \, dy \, dz \\
&= \sum_{k=1}^{M} \int_{x_k^{\min}}^{x_k^{\max}} dx \, \exp(-iq_x x) \int_{y_k^{\min}}^{y_k^{\max}} dy \, \exp(-iq_y y) \\
&\quad \times \int_{z_k^{\min}}^{z_k^{\max}} dz \, \exp(-iq_z z) \\
&= \sum_{k=1}^{M} \frac{i}{q_x} \left\{ \exp(-iq_x x_k^{\max}) - \exp(-iq_x x_k^{\min}) \right\} \\
&\quad \times \frac{i}{q_y} \left\{ \exp(-iq_y y_k^{\max}) - \exp(-iq_y y_k^{\min}) \right\} \\
&\quad \times \frac{i}{q_z} \left\{ \exp(-iq_z z_k^{\max}) - \exp(-iq_z z_k^{\min}) \right\} \,.
\end{aligned}
\tag{5.29}
$$

However, this expression only holds as long as q_x, q_y and q_z are different from zero. If any of these values becomes zero, Eq. (5.29) has to be replaced by the corresponding limiting value.

When the form factors F_i of all clusters have been obtained, we can insert them into Eq. (2.3) to calculate the scattering cross section. However, it has turned out that the system sizes of the present simulation data are still too small to allow for a meaningful comparison with the experimental GISAXS data. To briefly demonstrate this, we first rewrite Eq. (2.3) for N_c clusters with positions $\mathbf{R}_1, \ldots, \mathbf{R}_{N_c}$, and we isolate the terms with $i = j$ on the right-hand side [74]:

$$
N_c \frac{d\sigma}{d\Omega}(\mathbf{q}) = \sum_{i=1}^{N_c} |F_i(\mathbf{q})|^2 + \sum_{\substack{i,j=1 \\ j \neq i}}^{N_c} F_i(\mathbf{q}) F_j^*(\mathbf{q}) \exp\left[-i\mathbf{q} \cdot \left(\mathbf{R}_i - \mathbf{R}_j\right)\right] \,.
\tag{5.30}
$$

This form allows us to distinguish between the contributions from all individual clusters—which scale with N_c—and the contributions from all pairs of clusters—which scale with N_c^2. It is thus clear that N_c should be large to obtain broad distributions of form factors and distances between the particles, and also to obtain the correct statistical weights of both terms in Eq. (5.30). With the present simulation data, the second term Eq. (5.30) is insufficiently represented to reproduce the dominant features of the experimental data, e. g., the prominent side peak in q_y-direction from which the distance between the clusters can be obtained [61]. Another difficulty of the calculation is, again, the limitation of the simulation box which may cause artifacts in the form factors of large clusters and in the distributions of distances.

Despite these difficulties, the unique contribution from the form factor of just one cluster is singled out for demonstration in Fig. 5.12: on the left, the quantity $|F(q_y, q_z)|^2$ is shown, which has been calculated for the cluster depicted on the right. For that calculation, $q_x = 0$ was set to zero, in accordance with the introductory explanation in Sec. 2.1.2. The size of the grid cells was set to $0.4\,\text{nm} \times 0.4\,\text{nm}$ because the value $0.4\,\text{nm}$ is close to the lattice constant of gold; if one takes much smaller values, the resulting shape function may contain holes.
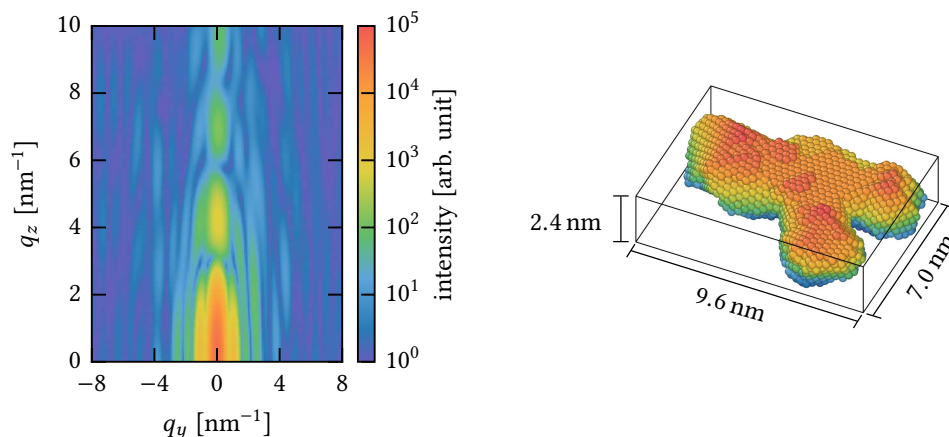
Figure 5.12.: Exemplary scattering pattern (left) calculated in Born approximation for a single cluster that occurred in a simulation (right). Adapted from [145].

Since the scattering pattern of single clusters are not detected in the relevant experiments, we will not pursue this type of calculations in the remainder of this work. Nevertheless, we conclude by making two remarks: first, the method presented in this section might open up new perspectives on the comparison between simulations and experiment once sufficiently big simulation boxes can be simulated. second, even if the scattering cross section cannot be calculated accurately, another utilization of the present data is conceivable: instead of using simpler geometric shapes, e. g., hemispheres, one may use the form factors of selected cluster structures to make a fit to experimental GISAXS data. For example, this can be done with the software program *BornAgain* [76], which already offers the functionality to implement custom form factors.

5.6. Summary

In this chapter, we established an MD simulation scheme to simulate the growth of gold clusters on a polymer surface. While all gold atoms were treated in full atomistic detail, a rather simple model was used to describe the diffusion of atoms in and on the polymer, the re-evaporation of atoms and the creation of surface defects. In order to mimic the behavior on experimental time scales, the simulations were carried out with proportionally rescaled values of the deposition rate and the diffusion coefficient presented in Ref. [61]. This procedure resulted in an effective acceleration of the growth dynamics by a factor of on the order of 10^9. Although such a strong shift of the time scales entails the risk of introducing artificial effects in the description, the comparison with the experimental morphology data was largely in support of the method. In Chapter 7, we will therefore take up these results and apply the method to a more complex situation, namely the deposition of two metallic species, silver and copper. Beforehand, however, we insert a chapter to make a further examination of the assumptions behind the rescaling procedure.

Chapter 6

Complementary Analysis of the MD Simulation Scheme

The derivation we made in Sec. 5.3 was based on the assumption that all δ-dependent functions to describe the morphology remain invariant under a rescaling of the deposition rate and the diffusion coefficient by an arbitrary factor. More precisely, we also remarked that the rate at which atoms re-evaporate from the surface must be rescaled as well, but due to the lack of experimental reference data, the quantities p_{re} and t_{re} were treated as free parameters in the simulations. In fact, the necessity to carry out the MD simulations with several free parameters makes it difficult to judge the accuracy of the method on a purely theoretical basis. The checks in the the last chapter were therefore restricted to comparisons with experimental data, and indeed, the results displayed at least partial agreement. In this chapter, we will go beyond such a comparison and make a further analysis which allows us to discuss some assumptions behind the rescaling method in greater detail. In Sec. 6.1, we will start by showing how the results are affected if the simulations are performed with another scaling factor ξ, see Eq. (5.20). Then, in Sec. 6.2, we will establish another approach to describe the cluster growth on surfaces in terms of rate equations. This will allow us to make the above mentioned invariance more plausible.

6.1. Variation of the scaling factor

In the derivation we made in Sec. 5.3 to motivate the rescaling of the deposition rate and the diffusion coefficients, we started by fixing the values of the temperature T and the time step Δt; only then we set the damping parameter $\tau_{surface}^{\parallel}$ to the typical value of $1\,ps$, which was chosen in respect of the time step. In doing so, the diffusion coefficient $D_{surface}^{\parallel}$ was fixed at the same time, and this allowed us to calculate the scaling factor ξ. One of the main assumptions made in Sec. 5.3 was that the problem of cluster growth remains similar on any time scale as long as the deposition rate, the diffusion coefficients (and the re-evaporation rates) are proportionally rescaled. Hence, one might argue that the MD simulations should yield the same film morphology even if they are performed for other ratios ξ. However, we will see in the next two sections that this is not exactly true because the behavior in the simulations
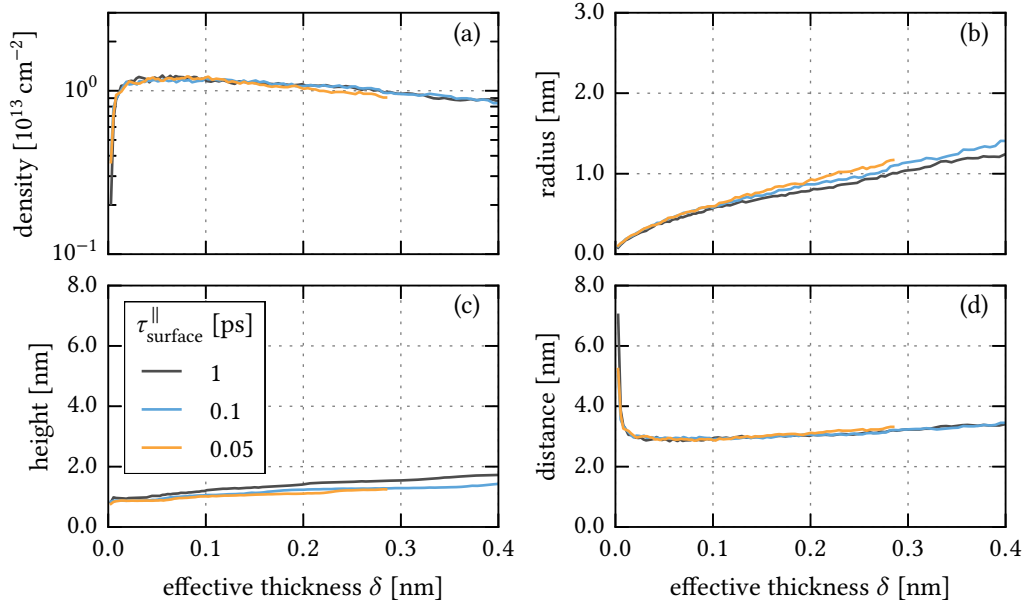
Figure 6.1.: Influence of the damping parameter $\tau_{\mathrm{surface}}^{\parallel}$ on the film morphology. The results were obtained from three simulations with $p_{\mathrm{re}} = 0$ and $\gamma = 1 \times 10^{-2}$.

is more complicated than the simplified picture on which the idea of the rescaling is based. Before we undertake this a closer examination in Sec. 6.1.2, we discuss possible choices of $\tau_{\mathrm{surface}}^{\parallel}$ and present exemplary simulation results in Sec. 6.1.1.

6.1.1. Simulation results

A practical way to perform the simulations with other values of ξ is to modify the damping parameter $\tau_{\mathrm{surface}}^{\parallel}$ and raise or lower the deposition rate and the re-evaporation rate accordingly. However, $\tau_{\mathrm{surface}}^{\parallel}$ can only be varied within a relatively small range. In the limit $\tau_{\mathrm{surface}}^{\parallel} \to \infty$, the friction force and the stochastic force in Eq. (5.7) vanish, i.e., the relaxation and the formation of clusters is strongly hampered. Consequently, there exists a regime of too large $\tau_{\mathrm{surface}}^{\parallel}$-values for which the simulations do not yield a reasonable behavior. In contrast, if $\tau_{\mathrm{surface}}^{\parallel}$ is lowered, both the diffusion and the deposition become slower because the system is strongly damped. Although the time scale of the simulation becomes closer to experimental time scales in that case, there are two reasons why the value of $\tau_{\mathrm{surface}}^{\parallel}$ should not be very small: first, this may lead to numerical problems as both appearances of $\tau_{\mathrm{surface}}^{\parallel}$ in Eq. (5.7) are in the denominators of the force terms. Second, a reduction of $\tau_{\mathrm{surface}}^{\parallel}$ by a certain factor leads to an increase of the simulation time by nearly the same factor. For many applications, it is therefore highly impractical to use values below roughly 0.1 ps.

For this study, we restrict ourselves to considering only small damping parameters as they shift the time scales to more realistic values. Despite the mentioned limitations, a comparison

for small film thicknesses below 0.3 nm is already possible employing the reduced values $\tau_{\text{surface}}^{\parallel} = 0.1\,\text{ps}$ and 0.05 ps. The corresponding morphology data from three simulations with those values of the damping parameter and $\tau_{\text{surface}}^{\parallel} = 1\,\text{ps}$ is shown in Fig. 6.1. To make this investigation less complex, the re-evaporation probability p_{re} was set to zero in the simulations. The parameter γ was set to 1×10^{-2}, and all other parameters—except the adjusted flux $J_{\text{m}}^{\text{sim}}$—were the same as for the simulations discussed in Sec. 5.5.2.

Considering the cluster density and the mean cluster distance first, one can hardly find any deviations between the results for the three values of $\tau_{\text{surface}}^{\parallel}$. Only for $\delta > 0.2\,\text{nm}$, it is apparent that the densities are slightly lowered for $\tau_{\text{surface}}^{\parallel} = 0.05\,\text{ps}$. More obvious deviations can be found for the cluster radius and the cluster height: apart from small fluctuations, the reduction of $\tau_{\text{surface}}^{\parallel}$ leads to larger radii, but smaller heights.

6.1.2. Discussion

The data in figure Fig. 6.1 is apparently not invariant under changes of the scaling factor ξ. As only a relatively small range of damping parameters was considered in this analysis, it remains open how strong the deviations will become if $\tau_{\text{surface}}^{\parallel}$ is reduced even further. However, we must stress that the behavior does not necessarily become more realistic just by decreasing $\tau_{\text{surface}}^{\parallel}$—even though the simulated times approach experimental time scales. Whilst it is indeed the case that the time evolution of the mean squared displacement of single atoms on the surface becomes more realistic if $\tau_{\text{surface}}^{\parallel}$ is decreased, it remains unclear to what degree the formation and relaxation of cluster structures is hampered. This, however, could put limitations on the range of possible damping parameters because one main assumption was that cluster processes must be sufficiently fast. The results for the radius and the height shown in Figs. 6.1b and c can be taken as an indication that the relaxation times of clusters are not rescaled in the same way as the diffusion coefficients and the deposition rate. The fact that a reduction of $\tau_{\text{surface}}^{\parallel}$ leads to larger radii but lower heights might be caused by the strong damping as it keeps the atoms in the surface layer and thus impedes clusters from expanding perpendicularly to the surface. However, further work would be required to analyze this in greater detail, because it is still unclear whether certain other parameters such as the detection time $t_{\text{detect}}^{\text{regions}}$ should also be modified if $\tau_{\text{surface}}^{\parallel}$ is changed.

Against this backdrop, we gain a more detailed view on the concept of the rescaling procedure: As the system is driven by Langevin dynamics, there is no other possibility than using a time step on the order of 1 fs and adjusting the damping parameter with respect to the time step. These parameters may only be varied within a small range. The deposition rate used in the simulations must be sufficiently large and adequately reflect the desired experimental conditions. In order to fulfill both requirements, it seems natural to make use of the assumption that certain processes are invariant under a rescaling of the process times—this aspect will be subject to the next section. Nevertheless, that does not mean the conditions in the simulations are the same for any chosen value of $\tau_{\text{surface}}^{\parallel}$. For that reason, the choice of the simulation parameters is to some extent always made by trial and error. Even then, there is no guarantee that we can reproduce the conditions of any deposition experiment with the rather simple simulation model.

6.2. Comparison with rate equations for cluster growth

In this section, we try to make it more plausible that the simulated behavior can indeed be mapped to other time scales. For that purpose, we introduce a set of rate equations with the following properties:

- The equations describe a cluster growth process on a surface. The solutions allow us to express the δ-dependence of the same morphological quantities that we investigated in Chapter 7.

- The δ-dependence of the morphological quantities remains unaffected by a linear rescaling of the deposition rate, all involved diffusion coefficients and the re-evaporation rate.

Finally, if it is possible to reproduce the simulated behavior with rate equation of this kind, this may be an indicator that the simulated behavior indeed remains invariant if it is shifted to other time scales according to the rescaling procedure.

In Sec. 6.2.1, we start this investigation by introducing a simple model for cluster growth on surfaces, and in Sec. 6.2.2, we analyze a set of rate equations which governs the time evolution of this model. Finally, in Sec. 6.2.3, we compare the results from the rate equations with results from the previous chapter.

6.2.1. Description of the model

We begin by giving a brief description of the components of the model and the considered processes. While some parts of the model are based on similar assumptions as the ones made for the definition of the KMC model presented in Chapter 4, it is also referred to the model on the growth of clusters in a magnetron-based gas aggregation source by Fujioka [39], because it provided the ideas for some other parts of the model. Furthermore, it is also referred to a similar study concerned with the growth of islands on a surface in Ref. [150].

The model system contains two different particle which represent atoms and clusters. The atoms are taken to have a spherical shape with the fixed radius r_a, and the clusters have a hemispherical shape whose radius r_c may grow over time. We assume that both species are located on a two-dimensional plane according to the illustration shown in Fig. 6.2. To avoid a description with explicit particle coordinates, we only use number densities (with dimensions $[\text{length}]^{-2}$) to describe the amounts of both species on the surface; in particular, we assume that these densities are spatially homogeneous, but time-dependent. Later, it will also be necessary to distinguish between isolated atoms on the surface and atoms that belong to a cluster. For the number densities of both atom types, we therefore introduce the labels n_a and n_a^*; for the number density of clusters, we write n_c.

Now we move to describe the processes that lead to changes of the three densities. An additional graphical illustration of these processes is provided by Fig. 6.3. For the sake of convenience, both the figure and the following explanations always refer to *individual* particles; nevertheless, it is still the case that the mathematical description will be in terms of number densities.
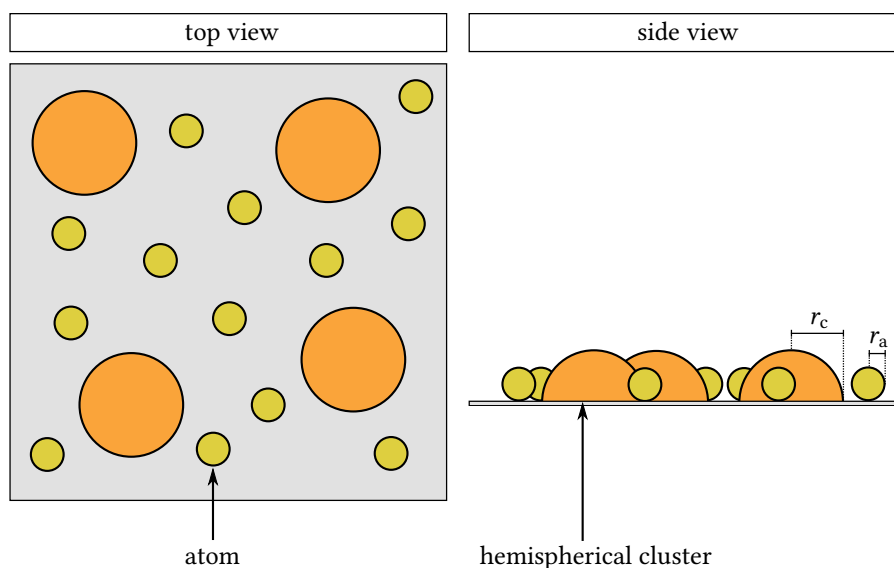
Figure 6.2.: Representation of atoms and clusters in the model which is used for the formulation of rate equations. It is stressed that this illustration may be misleading with regard to the positions of atoms and clusters: rather than taking account of any explicit particle coordinates, the model only makes statements about the number densities of atoms and cluster, and these densities are assumed to be homogeneous.

At the beginning, the surface is empty, but atoms are added to the system right after the beginning and throughout the whole time. The associated flux of atoms to the surface, J_m, is assumed to be constant and homogeneous. Just like in the MD simulations, it is also possible that isolated atoms are removed to represent incomplete condensation. The associated re-evaporation rate will be defined below. The formation of clusters is only possible when two isolated atoms join each other or when an atom is deposited on top of an isolated atom. The following three processes may lead to the growth of already existing clusters: an isolated atom is attached to a cluster as a result of surface diffusion, an atom is deposited on top of a cluster, or two clusters coalesce. It is assumed that all mentioned cluster formation and growth processes happen instantaneously. Furthermore, we simplify the problem by making the restriction that all clusters on the surface must have the same sizes. That means that whenever clusters are formed or clusters grow, we obtain a new value of the radius r_c, which can be understood as a mean value referring to *all* clusters. In fact, this approximation is only justified for systems with narrow cluster size distribution. As we have found that the size distributions resulting from the MD simulations become broader with increasing film thickness, we can already expect that both methods yield discrepancies for large values of δ.
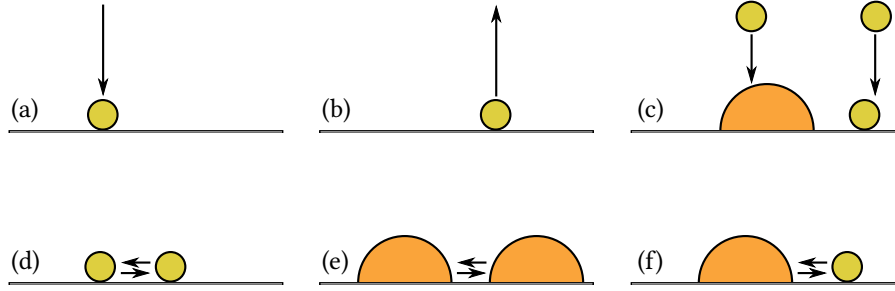
Figure 6.3.: Illustration of the processes described by the rate equations for cluster growth: deposition of an atom on the surface (a), re-evaporation of an atom (b), deposition of an atom on top of a cluster or another atom (c), merging of two diffusing atoms into the smallest possible cluster (d), merging of two diffusing clusters into a larger cluster (e), merging of a diffusing cluster and a diffusing atom (f).

6.2.2. Formulation of the equations

We proceed by putting the above behavior of the model in mathematical terms. Before we formulate three rate equations describing the time evolution of n_a, n_a^* and n_c, we briefly turn towards the calculation of several quantities which later enter the final equations.

Required quantities

Atomic radius   The specific choice of the atomic radius used in this model has an effect on the calculation of the surface coverage and the diffusion coefficient of atoms. For this study, r_a is set to the Wigner-Seitz radius of gold, $r_a = 0.165\,\text{nm}$ [142]. Nevertheless, it was checked that there exists a range of other reasonable values for which the solutions of the rate equations are nearly the same.

Cluster radius.   As all clusters are defined to have the same shape and size, the knowledge of n_a^* and n_c allows us to calculate the volume of each cluster from the expression

$$V_c = \frac{n_a^* m_{\text{Au}}}{n_c \varrho_{\text{Au}}} \ ,$$
(6.1)

where we reused the atomic mass m_{Au} and the density of gold ϱ_{Au}. Since the clusters are hemispherical, their radius can be obtained from

$$r_c = \left(\frac{6V_c}{4\pi}\right)^{-1/3} \ .$$
(6.2)

Hence, r_c unambiguously depends on the densities n_a^* and n_c in this model.

Surface coverage. In order to calculate the amount of atoms which is deposited on top of another atom or a cluster on the surface, it is required to calculate the fraction of the surface area which is covered with isolated atoms or clusters. At that, it is required to make separate calculations for each species, namely

$$c_\mathrm{a} = n_\mathrm{a} \cdot 4\pi r_\mathrm{a}^2 \qquad \text{and} \qquad c_\mathrm{c} = n_\mathrm{c} \cdot 4\pi r_\mathrm{c}^2 \ . \tag{6.3}$$

As the method puts no limitations on the amount of atoms and clusters in the system, the sum $c_\mathrm{a} + c_\mathrm{c}$ may, in principle, become larger than one. Therefore, we introduce another function for the total coverage which is always less than or equal to one,

$$c_\mathrm{total} = \begin{cases} c_\mathrm{a} + c_\mathrm{c}, & \text{if } c_\mathrm{a} + c_\mathrm{c} \leq 1 \\ 1, & \text{otherwise} \ . \end{cases} \tag{6.4}$$

Diffusion coefficients. For the calculation of collision rates, the diffusion coefficients of atoms and clusters will be required. Aiming at a reproduction of the MD simulation results, the diffusion coefficients of atoms, D_a, is set to the same value of $D_\mathrm{surface}^{\parallel}$ as in the simulations, see Eq. (5.10). For the diffusion coefficients of clusters, we make the ansatz

$$D_\mathrm{c}(r) = \frac{D_\mathrm{a}}{N(r)} \ , \tag{6.5}$$

where $N(r)$ is the number of atoms per cluster with radius r. This ansatz has been taken from the KMC simulation scheme which treats the size dependence of surface diffusion coefficients in the same fashion, see Eq. (4.6). For the determination of the collision rates, we summarize D_a and D_c using the notation

$$D(r) = \begin{cases} D_\mathrm{a}, & \text{if } r = r_\mathrm{a} \\ D_\mathrm{c}(r), & \text{otherwise} \ . \end{cases} \tag{6.6}$$

Coagulation rates. A crucial step in the explicit formulation of the rate equations is the determination of coagulation rates for all possible combinations of the involved particles. A typical approach to do this is based on an ansatz by Smoluchowski, which expresses the coagulation rate of two particle species A and B as the product of the associated densities n_A, n_B and a coagulation kernel $\kappa_{\mathrm{A,B}}$ [151]. In doing so, the problem is reduced to finding a kernel which appropriately describes the problem of interest. A commonly used kernel for systems whose particles move diffusively between collisions, is the so-called diffusion kernel [39, 152]. If we let r_A and r_B be the radii of particle species A and B, and D_A and D_B be their diffusion coefficients, the diffusion kernel takes the form

$$\kappa_{\mathrm{A,B}} = 4\pi \left(D_\mathrm{A} + D_\mathrm{B} \right) \left(r_\mathrm{A} + r_\mathrm{B} \right) \ . \tag{6.7}$$

Although the diffusion kernel is usually applied to three-dimensional systems, here, we will also use it for particles which grow on two-dimensional surfaces. For that purpose, we introduce the factor $\eta = 1\,\mathrm{nm}^{-1}$ to obtain correct units and write

$$\kappa(r_\mathrm{A}, r_\mathrm{B}) = 4\pi\eta \left(D(r_\mathrm{A}) + D(r_\mathrm{B}) \right) \left(r_\mathrm{A} + r_\mathrm{B} \right) \tag{6.8}$$

for two atoms or clusters with radii r_A and r_B.

It is stressed that the ansatz in Eq. (6.8) for the coagulation kernel involves a certain amount of guessing. However, as we do not need very accurate results for the purpose of this consideration, we make no attempt to find a strict derivation of a more appropriate coagulation kernel in this work. The primarily important assumption concerning the scale invariance is the fact that the dependence on both diffusion coefficients in Eq. (6.8) is linear.

Re-evaporation. In order to account for the re-evaporation of isolated atoms, we introduce the re-evaporation rate v_{re}, which denotes the fraction of isolated atoms that is removed per unit time. To achieve similarity between the MD simulations and this model, we reuse the quantities from Sec. 5.2 and write $v_{re} = p_{re}/t_{re}$. For the results of this study, the parameters $p_{re} = 0.9$ and $t_{re} = 300\,\text{fs}$ were used.

Rate equations for the densities of atoms and clusters

Making use of the above considerations, we proceed by formulating three differential equations for the dependence of n_a, n_a^* and n_c on the time t. We will do this by writing down and explaining each equation one after the other.

First rate equation: number density of isolated atoms. The first equation describes the change of the density of isolated atoms, n_a,

$$\frac{\mathrm{d}}{\mathrm{d}t}n_a = (1 - c_{total})\,J_m - \kappa(r_a, r_c)n_a n_c - \kappa(r_a, r_a)n_a n_a - c_a J_m - v_{re} n_a \,. \tag{6.9}$$

The first term on the right side, $(1 - c_{total})\,J_m$ accounts for the addition of isolated atoms due to deposition. As atoms may also be deposited on top of other atoms or clusters, the contribution is limited to the fraction $1 - c_c$ of the flux J_m. The two terms $-\kappa(r_a, r_c)n_a n_c$ and $-\kappa(r_a, r_a)n_a n_a$ express a reduction of n_a due to the coagulation of atoms and clusters or atoms and atoms. The term $-c_a J_m$ accounts for a reduction as a consequence of immediate cluster formation right after deposition on top of isolated atoms, and the last term $-v_{re} n_a$ describes a reduction due to re-evaporation.

Second rate equation: number density of atoms in clusters. The second equation, referring to the density of atoms in clusters, reads

$$\frac{\mathrm{d}}{\mathrm{d}t}n_a^* = 2c_a J_m + c_c J_m + \kappa(r_a, r_c)n_a n_c + \kappa(r_a, r_a)n_a n_a \,. \tag{6.10}$$

Again, $2c_a J_m$, describes the cluster formation after the deposition of an atom on top of an isolated atom; the factor two takes into account that two atoms contribute to this process. For the second term, $c_c J_m$, this factor is not required because just one atom is added to a cluster. The last two terms, $\kappa(r_a, r_c)n_a n_c$ and $\kappa(r_a, r_a)n_a n_a$, represent the same amount of atoms which has been removed from n_a in Eq. (6.9).

Third rate equation: number density of clusters. Finally, we let the density of clusters be governed by the equation

$$\frac{d}{dt}n_c = \frac{1}{2}\kappa(r_a, r_a)n_a n_a - \frac{1}{2}\kappa(r_c, r_c)n_c n_c + c_a J_m \ . \tag{6.11}$$

The first two terms on the right side describe an increase due to the coagulation of atoms and a decrease due to the coagulation of clusters. The factor $1/2$ occurring in each of the terms arises from the assumption that only half of the involved particles make an effective contribution. The last term, $c_a J_m$, represents an increase due to immediate cluster formation after the deposition of an atom.

Discussion of the solutions

The present set of rate equations has the property that the solutions for two different parameter sets $\{D_a, J_m, \nu_{re}\}$ and $\left\{\tilde{D}_a, \tilde{J}_m, \tilde{\nu}_{re}\right\}$ can be transformed into each other according to

$$\tilde{n}_a(t) = n_a(\xi t) \ , \tag{6.12}$$

$$\tilde{n}_a^*(t) = n_a^*(\xi t) \ , \tag{6.13}$$

$$\tilde{n}_c(t) = n_c(\xi t) \tag{6.14}$$

if the relation

$$\tilde{D}_a = \xi D_a \ , \tag{6.15}$$

$$\tilde{J}_m = \xi J_m \ , \tag{6.16}$$

$$\tilde{\nu}_{re} = \xi \nu_{re} \tag{6.17}$$

holds. That immediately follows from the fact that each term on the right sides of Eqs. (6.9), (6.10) and (6.11) has a linear dependence on either D_a, J_m or ν_{re}. Furthermore, we can also deduce

$$f(n_a(t), n_a^*(t), n_c(t)) = f(\tilde{n}_a(\xi t), \tilde{n}_a^*(\xi t), \tilde{n}_c(\xi t)) \ . \tag{6.18}$$

for any function f that depends on the three densities. In particular, we find

$$\delta(n_a(t), n_a^*(t)) = \delta(\tilde{n}_a(\xi t), \tilde{n}_a^*(\xi t)) \tag{6.19}$$

for the effective film thickness as it only depends on the amount of atoms in the system. Consequently, we can use δ as a joint reference quantity and find that the morphological quantities which only depend on any combination of the three densities have the same δ-dependence for both parameter sets.

6.2.3. Results

In Fig. 6.4, the MD results for $p_{re} = 1 \times 10^{-4}$ and $\gamma = 1 \times 10^{-2}$ and the experimental results, which were first presented in Fig. 5.6, can be compared with the results obtained from a numerical solution of the three rate equations. The curves belonging to the rate equations

represent the following quantities: For the density of clusters in Fig. 6.4a, the quantity n_c is shown. For the curves of both the radius and the height in Figs. 6.4b and c, the cluster radius r_c defined in Eq. (6.2.2) is shown. The curve for the cluster distance in Fig. 6.4d represents the term $n_c^{-1/2}$, i. e., the distance is again derived from the cluster density. Finally, in Fig. 6.4e, the quantity c_{total} from Eq. (6.4) indicates the total coverage of the surface.

The data in the figure reveals that the results from the rate equations are indeed similar to the simulation results, but there are also strong deviations, in particular for large values of δ. While the rising part and the maximum of the cluster density are accurately captured, the decay is clearly weaker than in the simulations and in the experiment. The curve for the height always remains below the other two curves, which might be a systematic weakness of the model as it enforces the equality of the cluster radius and the cluster height. Finally, also the coverage obtained from the rate equations displays clear deviations from the MD results; for example, it already reaches a value of 100 % for $\delta = 2$ nm while the value from MD is still around 65 %.

Since the model used for the rate equations is based on several estimations and approximations with unknown accuracy, we could have expected that no perfect agreement with the simulation results is achieved. The fact that the strongest deviations occur for large values of δ can be explained by the following two reasons: On the one hand, the shape of the hemispherical clusters clearly deviates from the branched structures occurring in the MD simulations. On the other hand, we can expect that the inaccuracies resulting from the choice of the coagulation kernel mainly affect the δ-regime containing the decay of the cluster density; this is the part where the coagulation process dominates the behavior of the system. Furthermore, the choice of a diffusion kernel is only appropriate if the motion of the involved particles is diffusive before they coagulate; however, this requirement becomes violated when the surface coverage becomes so large that the space between the clusters is very small. In this work, all those flaws of the model for the rate equations are not eradicated. Nevertheless, that does not mean that the results cannot be significantly improved, e. g., by spending further theoretical work on the establishment of a coagulation kernel which is more appropriate for this problem. For the purpose of this study, it is sufficient that the rate equations and the MD simulations show at least partial agreement for $\delta \lesssim 0.4$ nm. We have thus found another reason to justify the approximation that the δ-dependence of the film morphology remains invariant under linear rescaling of the flux of atoms to the surface, the involved diffusion coefficients and the re-evaporation rate.
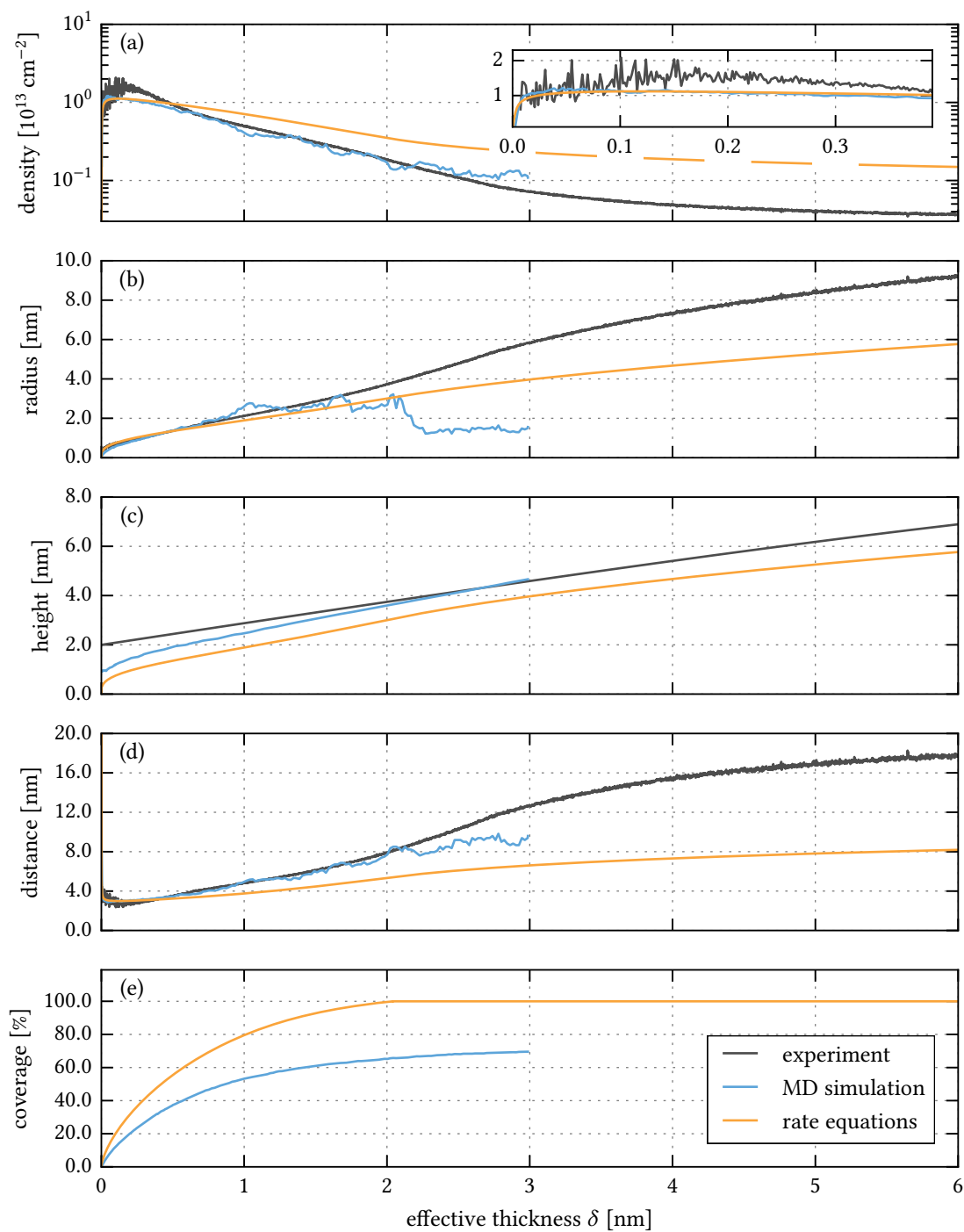
Figure 6.4.: Comparison of the film morphology data obtained from a solution of the rate equations with MD simulation results and experimental results. The MD results and the experimental results are the same as the ones shown before in Fig. 5.6.

Chapter 7

Growth of Silver–Copper Clusters on a Polymer Surface

The MD simulation scheme presented in Chapter 5 allows for a simple exchange of the metallic particle species. For the most part, the technical realization only requires to replace the interaction potential and a few material constants. Therefore, it is even just a small effort to integrate more than one metallic species. In fact, we will do this in this chapter: we will reuse the simulation scheme from Chapter 5 and apply it to the growth of silver–copper (Ag–Cu) nanoparticles.

Before we start this investigation, we make a few remarks to motivate the specific choice of silver and copper. First of all, there is a general interest in combining different materials because of the potential to discover nanoparticles with new properties. This especially holds for intermatallic compound particles, which have been in the focus of many studies during the last few years [62, 153, 154]. The specific interest in Ag–Cu nanoparticles arises from the fact that the Ag–Cu bulk system possesses a well-known miscibility gap over wide temperature and concentration ranges [155], but only little is known about the miscibility of both materials on the nanoscale. In particular, it is not known how the separation of Ag and Cu atoms in a cluster behaves during the growth on polymer surfaces. On the one hand, it has been shown that a segregated structure with silver on the surface and copper in the core is the energetically favorable structure of clusters with radii of up to several nanometers [63, 156]. On the other hand, however, it has also been reported that the final configuration of the particles is quite sensitive to the way the particles are created; in many cases, one thus observes metastable configurations rather than core–shell geometries.

One reason why MD simulation results might provide valuable insights is that even the most recent experimental findings concerning the phase separation in Ag–Cu nanoparticles still lack full atomistic detail and a high time resolution. Although there already exist various computational studies—e. g., on the ground states of very small Ag–Cu clusters [156, 157], on the formation of Ag shells on Cu clusters [155], and on the coalescence of Ag and Cu clusters [63, 158]—the complex mechanisms involving a multitude of clusters on a surface during film growth have not yet been taken into account.

A common experimental technique to study the composition of bi- or polymetallic nanopar-

ticles draws upon spectroscopic ultraviolet-visible (UV-vis) extinction measurements [62, 159, 160]. For example, it has been observed for nanocomposites composed of Ag–Cu nanoparticles in a Teflon AF matrix that an increase of the particle size is associated with the occurrence of double plasmon resonances [62]. The authors presume that this is attributed to the formation of core–shell structures, but the nature of the experimental method does not permit a direct observation. Another approach that draws on electron microscopy was followed by Radnóczi *et al.* who tried to infer structural details of co-deposited Ag–Cu nanoparticles on a carbon film by calculating the Fourier transform of high-resolution real-space images [161]. Studying different compositions with an Ag content varying in the range from 15 to 80 at.%, the authors have found that particles with sizes below 5 nm grow as a solid solution for all compositions; for larger particles, they have observed a composition-dependent unmixing of both phases by spinodal decomposition.

Due to the recent interest in the phase separation of Ag–Cu clusters, exactly this aspect will be in the focus of this chapter; the morphology, which we extensively studied for gold in Chapter 5, will only play a minor role. In Secs. 7.1 and 7.2, we will explain how the simulation scheme can be adapted to the Ag–Cu system and define the distribution functions to characterize the phase separation. In Sec. 7.3, we will first make a brief comparison with the results for gold and then study the phase separation for four different ratios of the fluxes of Ag and Cu atoms towards the surface.

7.1. Adjustment of simulation parameters

The MD simulation scheme contains several parameters whose values cannot be derived from a rigorous methodology. Instead, they are guessed under rather general physical assumptions or they are optimized such that specific experimental data can be reproduced. While the simulations for the growth of gold films were intended to reflect the experimental behavior observed in Ref. [61], similar reference data is lacking for the Ag–Cu system. Therefore, the adjustment of the parameters for the simulations discussed in this chapter introduces some additional uncertainties. Nevertheless, we can expect to capture the characteristic behavior at least on a qualitative level. In the following, we will concern ourselves with the modifications of the simulation parameters that have been made to simulate the deposition silver and copper instead of gold.

Material constants. All involved material constants for gold are replaced by the corresponding values for silver and copper. Hence, the masses of Ag and Cu atoms are set to $m_{\text{Ag}} = 63.55\,\text{u}$ and $m_{\text{Cu}} = 107.87\,\text{u}$, and the respective densities are set to $\varrho_{\text{Ag}} = 10.49\,\text{g/cm}^3$ and $\varrho_{\text{Cu}} = 8.96\,\text{g/cm}^3$.

Dimensions of the simulation box. The partitioning of the simulation box is the same as the one for gold. However, most of the results in this chapter have been obtained with larger simulation boxes, namely $L_x = L_y = 60\,\text{nm}$. The only exception are the simulations for two curves shown in Fig. 7.1, which have been performed with surface sizes of $40\,\text{nm} \times 40\,\text{nm}$.

Diffusion and deposition. The main difficulty imposed by the lack of experimental reference data lies in finding reasonable values for the deposition rates and the damping parameters. The simulations for the results in this chapter have been carried out with guessed values. In the following, we look closer at the assumptions under which these guesses have been made.

The equations of motion introduced in Sec. 5.2 have been written for particles with different masses, but the employed damping parameters have been the same for all particles. A generalization of the equations of motion for the particles in the surface region $B_{(II)}$ can be written as follows:

$$m_i \ddot{x}_i = F_i^x(\mathbf{r}_i) - \frac{m_i}{\tau_{\text{surface}, i}^{\parallel}} \dot{x}_i + \sqrt{\frac{2 m_i k_B T}{\tau_{\text{surface}, i}^{\parallel}}} R_i^x \ , \tag{7.1}$$

$$m_i \ddot{y}_i = F_i^y(\mathbf{r}_i) - \frac{m_i}{\tau_{\text{surface}, i}^{\parallel}} \dot{y}_i + \sqrt{\frac{2 m_i k_B T}{\tau_{\text{surface}, i}^{\parallel}}} R_i^y \ , \tag{7.2}$$

$$m_i \ddot{z}_i = F_i^z(\mathbf{r}_i) - \frac{m_i}{\tau_{\text{surface}, i}^{\perp}} \dot{z}_i + \sqrt{\frac{2 m_i k_B T}{\tau_{\text{surface}, i}^{\perp}}} R_i^z \tag{7.3}$$

Likewise, we can write

$$m_i \ddot{\mathbf{r}}_i = \mathbf{F}_i(\mathbf{r}_i) - \frac{m_i}{\tau_{\text{bulk}, i}} \dot{\mathbf{r}}_i + \sqrt{\frac{2 m_i k_B T}{\tau_{\text{bulk}, i}}} \mathbf{R}_i \tag{7.4}$$

for the bulk region $B_{(I)}$. For both regions, we added the index i to all occurring damping parameters, which allows us to define individual damping parameters for each particle. In particular, if we are restricted to two particle species, the index i is used to distinguish between both species Ag or Cu. In principle, this formulation allows us to assign different values to the damping parameters of Ag and Cu so that any required diffusion coefficient can be realized. However, as it is unknown which diffusion coefficients are most appropriate for both species, the damping parameters $\tau_{\text{surface}, i}^{\parallel}$ are again set to the standard value $\tau_{\text{surface}}^{\parallel} = 1\,\text{ps}$ for all i. Just as in the case of gold, the remaining parameters $\tau_{\text{surface}, i}^{\perp}$ and $\tau_{\text{bulk}, i}$ are then set to the same values according to

$$\tau_{\text{bulk}, i} = \tau_{\text{surface}, i}^{\perp} = \frac{\tau_{\text{surface}}^{\parallel}}{r_{\text{s/b}}} \tag{7.5}$$

for all i with $r_{\text{s/b}} = 80$. As a result of this method, both atom species are assigned the same sets of damping parameters, but the resulting diffusion coefficients still different because of the different atomic masses. In this case, the diffusion of Ag atoms will be faster because m_{Ag} is less than m_{Cu}.

While the proper choice of diffusion coefficients is crucial to represent specific materials, the choice of deposition rate is less critical because it can be varied over a broad range in the experiments. The total flux of atoms towards the surface, $J_{\text{m}}^{\text{sim}}$, is therefore set to the same value as the value used for the deposition of gold. This flux is the some of the fluxes of Ag and Cu atoms, i. e., it can be written as

$$J_{\text{m}}^{\text{sim}} = J_{\text{Ag}}^{\text{sim}} + J_{\text{Cu}}^{\text{sim}} \ . \tag{7.6}$$

However, we will not explicitly name the values of J_{Ag}^{sim} and J_{Cu}^{sim} in the results section, but rather employ the ratios

$$\epsilon_{Ag} = \frac{J_{Ag}^{sim}}{J_{m}^{sim}} \qquad \text{and} \qquad \epsilon_{Cu} = \frac{J_{Cu}^{sim}}{J_{m}^{sim}} \ . \tag{7.7}$$

These ratios are not necessarily equal to the fractions of Ag and Cu atoms in the deposited film because the amount of re-evaporated atoms may be different for both species. In this case, however, the re-evaporation probability is set to the same value for both species (see below); thus, the fractions ϵ_{Ag} and ϵ_{Cu} indeed apply to the amount of Ag and Cu atoms in the film, too.

Finally, it is remarked that the lack of material-specific diffusion coefficients makes it impossible to specify the boost factor ξ the same way as for gold, using Eq. (5.20). Nevertheless, we may assume that a similar boost factor on the order of 10^9 is also be achieved for silver and copper.

Interaction potentials.   The interatomic interactions are again treated in the framework of the embedded-atom method. The specific potential for Ag–Cu alloys was taken from the work by Williams *et al.* in Ref. [162]. This choice was motivated by the fact that similar MD simulations for Ag–Cu nanoparticles described in Refs. [63, 158] were performed with the same potentials.

Surface defects and re-evaporation.   Just as in the case for gold, the parameters γ and p_{re} used to control the creation of surface defects and the re-evaporation of atoms should be adjusted to experimental data. Yet, due to the lack of appropriate reference data, it is again uncertain what the values of these parameters should be for the simulations with silver and copper. The values are therefore guessed on the basis of the simulations for gold. Such being the case, the re-evaporation probability was set to $p_{re} = 1 \times 10^{-4}$ for all simulations discussed in this chapter. The fraction of deposited defects γ was varied between 1×10^{-3} and 1×10^{-1} for the results on the morphology in Sec. **??**; for the study of phase separation in Sec. 7.3.2, however, only the value $\gamma = 1 \times 10^{-2}$ was considered because the use of $p_{re} = 1 \times 10^{-4}$ and $\gamma = 1 \times 10^{-2}$ for gold led to good agreement with experimental data.

7.2. Calculation of distribution functions

To study the degree of phase separation, we will characterize both species in terms of the following distribution functions: one for the z-coordinates of all atoms in the film, and one for the radial distances of atoms in clusters. Both distributions functions are approximately determined from corresponding histograms of atom positions with bins of equal size.

In the following, we let X represent the atom species, i. e., Ag or Cu. The vertical distribution for X is obtained at positions z_i from the expression

$$f_X(z_i) = \frac{N_{X,i}}{N_m \Delta z} \ , \tag{7.8}$$

where Δz is the bin width, N_{m} is the total number of both Ag and Cu atoms in the system, and $N_{\mathrm{X},i}$ is the number of Ag/Cu atoms in the i-th bin ranging from $z_i - \Delta z/2$ to $z_i + \Delta z/2$. According to this definition, the distribution function of species X is normalized to its relative amount ϵ_{X}. We can thus write

$$\int_0^\infty f_{\mathrm{X}}(z) \, \mathrm{d}z = \epsilon_{\mathrm{X}} \tag{7.9}$$

and

$$\int_0^\infty \left(f_{\mathrm{Ag}}(z) + f_{\mathrm{Cu}}(z) \right) \, \mathrm{d}z = 1 \, . \tag{7.10}$$

While we do not distinguish between different clusters for the calculation of the vertical distribution function, the radial distribution function is defined to be the pointwise average of the radial distribution functions of all clusters. This quantity is only meaningful as long as all clusters have nearly the same shapes and sizes. Similarly to the vertical distribution function, the radial distribution function of the k-th clusters is obtained from

$$\chi_{\mathrm{X},k}(r_i) = \frac{N_{\mathrm{X},k,i}}{N_{\mathrm{m},k} \Delta r} \, , \tag{7.11}$$

where Δr is the bin width, $N_{\mathrm{m},k}$ is the total number of atoms in the cluster, and $N_{\mathrm{X},k,i}$ is the number of Ag/Cu atoms whose planar distance d from the center of the cluster (see Eq. (5.23)) lies in the range from $r_i - \Delta r/2$ to $r_i + \Delta r/2$. According to this definition, we obtain the integrals

$$\int_0^\infty \chi_{\mathrm{X},k}(r) \, \mathrm{d}r = \epsilon_{\mathrm{X}} \tag{7.12}$$

and

$$\int_0^\infty \left(\chi_{\mathrm{Ag},k}(r) + \chi_{\mathrm{Cu},k}(r) \right) \, \mathrm{d}r = 1 \, . \tag{7.13}$$

Finally, the average radial distribution function is calculated from

$$\overline{\chi}_{\mathrm{X}}(r) = \frac{1}{N_{\mathrm{c}}} \sum_{k=1}^{N_{\mathrm{c}}} \chi_{\mathrm{X},k}(r) \, , \tag{7.14}$$

where N_{c} is the number of clusters in the system. This definition consistently yields

$$\int_0^\infty \overline{\chi}_{\mathrm{X}}(r) \, \mathrm{d}r = \epsilon_{\mathrm{X}} \tag{7.15}$$

and

$$\int_0^\infty \left(\overline{\chi}_{\mathrm{Ag}}(r) + \overline{\chi}_{\mathrm{Cu}}(r) \right) \, \mathrm{d}r = 1 \, . \tag{7.16}$$

It is remarked that the above definition of the radial distribution function may be considered uncommon in so far as the integrand of the integral (7.12) does not contain an additional factor r^2. Nevertheless, this aspect is uncritical because the behavior of the relevant intersections of the Ag and Cu distribution curves remains unaffected from the normalization procedure.
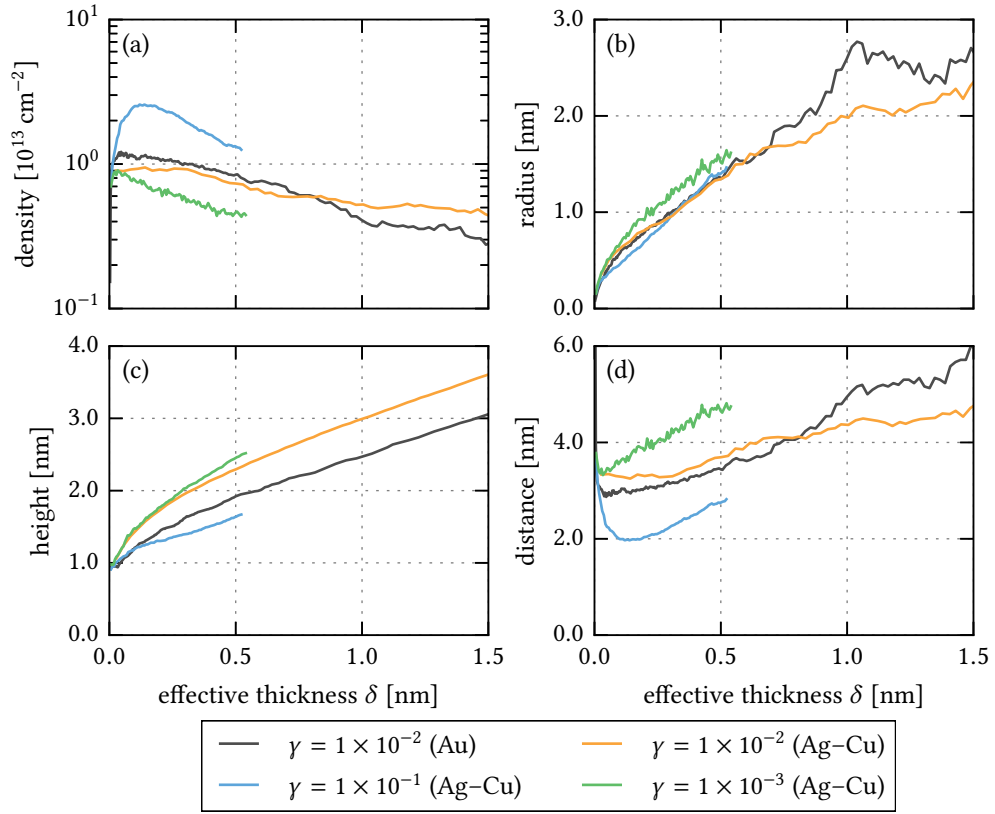
Figure 7.1.: Evolution of the Ag–Cu film morphology as a function of the effective film thickness δ for different fractions of deposited defects γ. The Ag content is 50 at.%. For comparison, the data for gold with $\gamma = 1 \times 10^{-2}$ and $p_{\text{re}} = 1 \times 10^{-4}$ from the previous chapter is also shown. The simulation runs for Ag–Cu films with $\gamma = 1 \times 10^{-1}$ and 1×10^{-3} have been performed with a reduced surface size of $40\,\text{nm} \times 40\,\text{nm}$. Adapted from [163].

7.3. Simulation results

We proceed by discussing the simulation results. In Sec. 7.3.1, we briefly consider the film morphology, and in Sec. 7.3.2, we study the phase separation.

7.3.1. Film morphology

Just to show the similarity to the simulations for gold, the morphological quantities which have been in the focus of the previous chapter are also shown for the deposition of silver and copper. In Fig. 7.1, the number density of clusters, the cluster heights, radii and distances are depicted as a function of the effective film thickness δ for three values of γ and $\epsilon_{\text{Ag}} = 0.5$. For $\gamma = 1 \times 10^{-3}$ and $\gamma = 1 \times 10^{-1}$, the simulations have been restricted to film thicknesses below

$\delta \approx 0.5$ nm; this is sufficient to show the peaks of the cluster density. A longer simulation run has only been performed for $\gamma = 1 \times 10^{-2}$ because this is the value which is used for the study of phase separation. In addition to the data for silver and copper, the results for gold with the parameters $\gamma = 1 \times 10^{-2}$ and $p_{re} = 1 \times 10^{-4}$ are shown as well, but one has to take into account that that any value of δ for Ag and Cu corresponds to a total number of atoms which is different from the total number of gold atoms that belongs to the same value of δ. The reason for this is the difference of the corresponding densities.

For all three values of γ the behavior of the Ag–Cu film morphology displays the same characteristic features as discussed in Secs. 5.5.2 and 5.5.3 for gold. In particular, it is again the case that an increase of the amount of defects leads to a larger number of clusters, but the cluster sizes are reduced. Apart from that, we will refrain from an additional description of the morphology in this section. Instead, we restrict ourselves to noticing that the Ag–Cuclusters, whose phase separation is considered in the next section, have similar shapes as the gold clusters. This is also true for other values of ϵ_{Ag}, but the corresponding data is not shown here.

7.3.2. Phase separation

We now move to the investigation of phase separation. It is mentioned in advance that all simulations displayed the expected trend that more Ag atoms than Cu atoms can be found in the vicinity of the cluster surface. However, a perfect core–shell structure, i. e., complete phase separation, occurred in none of the simulations.

Results for equal fluxes of Ag and Cu

We start the discussion by referring to the simulation results for $\epsilon_{Ag} = 0.5$ presented in Fig. 7.2. The figure shows the evolution of the arrangement of Ag and Cu atoms in the cluster by depicting the cluster configurations and the distribution functions $\overline{\chi}$ and f for four different values of δ ranging from 0.07 nm (1.7×10^4 atoms) to 1.8 nm (4.4×10^5 atoms). In the first row, the clusters are shown as seen from a top view. The dominating blue color already indicates the presence of Ag atoms on top of the clusters—not only for large effective thicknesses, but already for $\delta = 0.07$ nm, which is more difficult to recognize. In order to reveal more information on the arrangement of atoms inside the cluster, the same clusters as in the first row are also shown in the second row, but all atoms with z-coordinates larger than 1 have been removed. In these images, the red color dominates, i. e., the preferred region of Cu atoms is the core of the cluster. A detailed look at the clusters also reveals that nearly all clusters are surrounded by a thin shell of Ag atoms. In most cases, the thickness of these shells does not exceed that of roughly one monolayer. A similar observation was also made in the aforementioned MD simulations of Ag–Cu cluster formation [63, 158], but an experimental confirmation is still required. Besides the formation of the outer layer of silver, a significant amount of Ag atoms can also be found in the whole inner volume of the cluster. While some of these atoms appear to be randomly distributed amidst the surrounding copper atoms, other Ag atoms tend to from structures that connect the outer parts of the clusters like a network. These structures are formed when two or more clusters with Ag shells agglomerate because
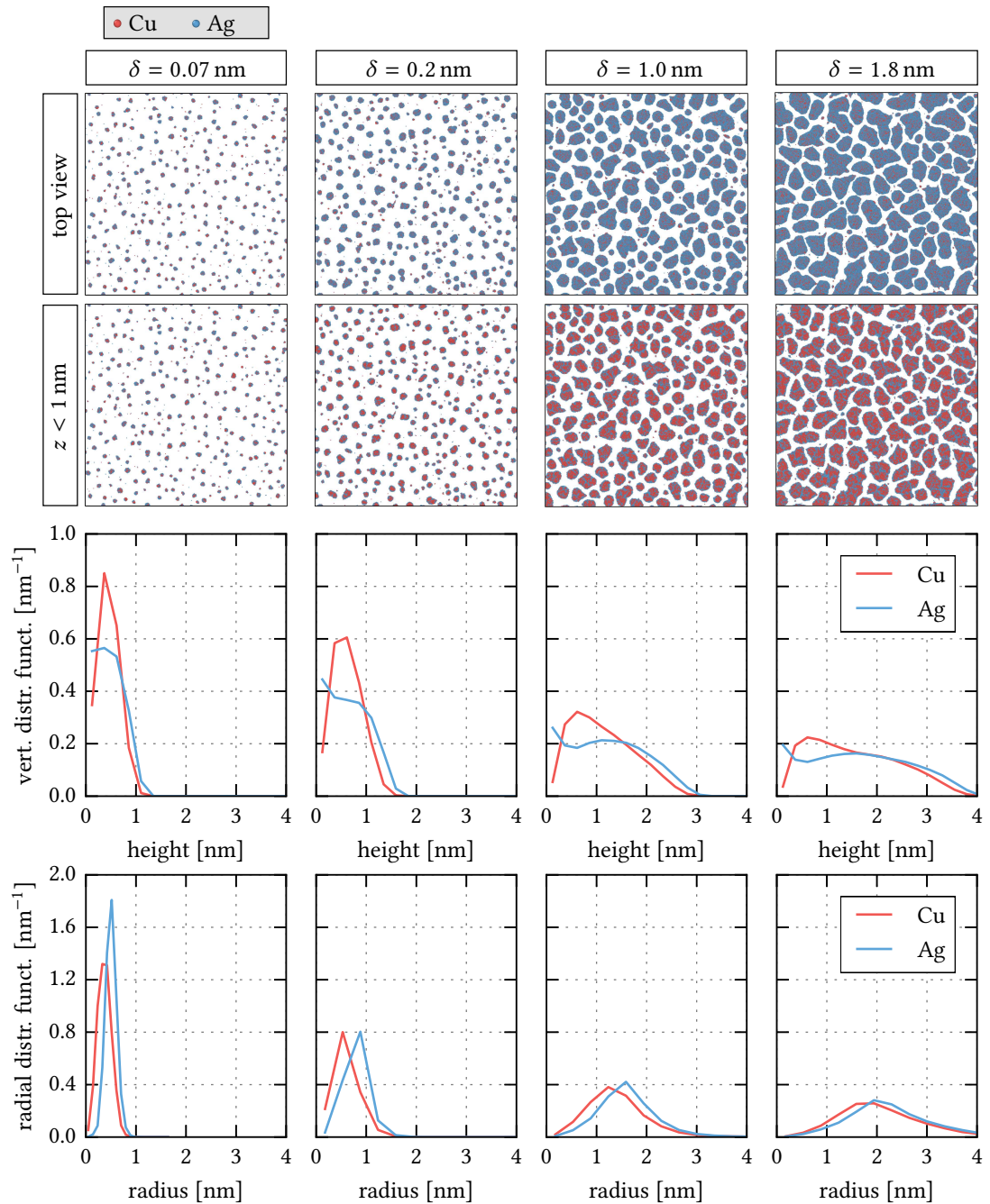
Figure 7.2.: Illustration of film growth and phase separation for different values of the effective thickness δ according to a simulation with 50 at.% Ag content. The first row shows the evolution of the morphology as seen in a top view; the size of the surface is 60 nm × 60 nm. The second row shows the same configurations, but all atoms with z-coordinates larger than 1 nm are excluded. The third and fourth rows show the distribution of Cu and Ag in a cluster for vertical and radial directions. Adapted from [163].
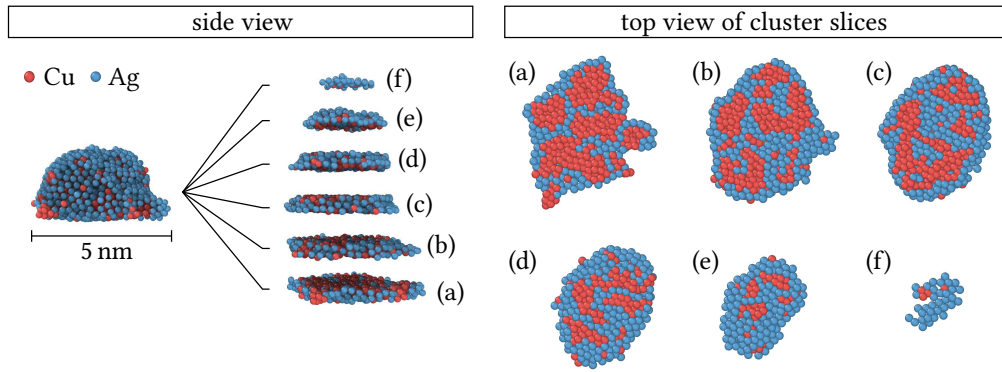
Figure 7.3.: Arrangement of Ag and Cu atoms in an exemplary cluster which occurred in a simulation with 50 at.% Ag content. On the left, the cluster is has been cut into six slices of thickness 0.5 nm. On the right, the same slices are shown from the top. Adapted from [163].

some atoms, which were previously on the surfaces of both clusters, are moved to the bulk of the resulting cluster. As the internal rearrangement of atoms is a very slow process, the network structures remain stable for a long time. Because it may be difficult to recognize these details in Fig. 7.2, it is also referred to Fig. 7.3, which shows the same effects for an exemplary cluster. The figure demonstrates the internal structure of cluster by prov ding a look at six slices of equal thickness which have resulted from dissecting the cluster several times parallely to the surface.

In addition to the above qualitative statements on the basis of the visualized cluster structures, we now turn towards the distribution functions shown in the third and fourth rows of Fig. 7.2. Both the redial and the vertical distribution function confirm that the clusters exhibit Cu-rich regions, which are formed at an early stage and then persist throughout the remaining time of the deposition. The heights at which the largest relative differences between the numbers of Ag and Cu atoms occur have relatively stable positions between 0.4 nm and 0.6 nm; Beyond that, we find that these heights are very close to the maxima of functions for Cu and—for $\delta = 1.0$ nm and 1.8 nm— also to the local minima of the curves for Ag. The transitions between Cu-rich and Ag-rich regions are indicated by intersections of the distribution functions: while the each pair of vertical distributions functions exhibit two such intersections—marking the transitions at the top and the bottom of the cluster—the corresponding radial distributions exhibit just one intersection, which refers to all radial directions. Furthermore, the tails of all presented Ag distribution functions lie above the tails of the functions for Cu, but the difference is only small as it is mainly caused by the thin layer of Ag atoms on the cluster surface. In fact, the distributions reveal that a large fraction of Ag and Cu atoms remains mixed with each other. Simulation snapshots such as the ones in the first two rows therefore provide valuable additional information on the structural details of both phases.

Evolution of characteristic points

To complement the above analysis, we now summarize the δ-dependence of the vertical distribution functions. For that purpose, we introduce the following characteristic points:

1. $z_{\mathrm{max,Cu}}$ is the height at which the local maximum of f_{Cu} occurs.

2. $z_{\mathrm{min,Ag}}$ is the height at which the local minimum of f_{Ag} occurs. As mentioned before, such a minimum can only be found for sufficiently large values of δ.

3. $z_{\mathrm{max,Ag}}$ is the height at which the local maximum of f_{Ag} occurs. Again, only sufficiently large values of δ are considered for which local maxima with $z_{\mathrm{max,Ag}} > z_{\mathrm{min,Ag}}$ exist.

4. Δz_{Ag} is the difference of the height larger than $z_{\mathrm{max,Ag}}$ at which the value of f_{Ag} falls below $0.5 \cdot f_{\mathrm{Ag}}(z_{\mathrm{max,Ag}})$ and $z_{\mathrm{min,Ag}}$. Hence, Δz_{Ag} is only defined if the second and third points exist. Δz_{Ag} can be understood as a measure for the peak width of the function f_{Ag}.

In Fig. 7.4, it is shown how the values of these points depend on the film thickness δ. The curves for $z_{\mathrm{max,Cu}}$ and $z_{\mathrm{min,Ag}}$ confirm that the Cu-rich regions maintain a relatively stable height throughout the whole deposition process. The characteristic peak of the function f_{Cu} already appears for small values of δ because the clusters rapidly form a Cu core. Before the corresponding value of $z_{\mathrm{max,Cu}}$ remains nearly constant at $0.6\,\mathrm{nm}$ for $\delta > 0.4\,\mathrm{nm}$, it slowly increases from an initial value of $0.36\,\mathrm{nm}$. In contrast, a minimum of the function f_{Ag} can only be found for slightly larger film thicknesses, $\delta > 0.37\,\mathrm{nm}$; however, the associated value of $z_{\mathrm{min,Ag}}$ remains nearly constant from the beginning.

Stronger changes are only exhibited by the curves for $z_{\mathrm{max,Ag}}$ and Δz_{Ag}. As a maximum of the function f_{Ag} can only be found for $\delta > 0.7\,\mathrm{nm}$, these curves set in for larger thicknesses than the other curves. For $\delta < 1\,\mathrm{nm}$, $z_{\mathrm{max,Ag}}$ only weakly increases from $1.1\,\mathrm{nm}$ to $1.2\,\mathrm{nm}$. A stronger increase of $z_{\mathrm{max,Ag}}$ to the value $1.5\,\mathrm{nm}$ follows in the range between $\delta = 1\,\mathrm{nm}$ and $\delta = 1.4\,\mathrm{nm}$. Only for larger values of δ, $z_{\mathrm{max,Ag}}$ levels off again. Lastly, the most apparent increase is exhibited by the curve for the width Δz_{Ag}, whose slope is nearly constant for all values of δ. Although the peak of f_{Ag} becomes broader, we have already seen in the third row of Fig. 7.2 that the tail of f_{Cu} broadens as well; thus, we cannot take the rise of Δz_{Ag} as an indicator for an ongoing phase separation. As mentioned before, rather the opposite is the case, namely that both phases persistently display a considerable overlap. It remains to be discussed to which extent this behavior can be considered realistic.

Results for other ratios of the fluxes

To conclude this investigation, we now turn towards other values of ϵ_{Ag}, namely 0.3, 0.7 and 0.9. Here, we restrict ourselves to considering the vertical distribution functions f_{Ag} and f_{Cu} for $\delta = 0.05\,\mathrm{nm}$, $0.3\,\mathrm{nm}$ and $0.6\,\mathrm{nm}$ shown in Fig. 7.5; the radial distributions are not shown because they exhibit a very similar behavior.

The behavior for $\epsilon_{\mathrm{Ag}} = 0.3$, which is displayed by the graphs in the first row, has a strong similarity to the behavior for $\epsilon_{\mathrm{Ag}} = 0.5$: the clusters have a Cu-rich core, and the Ag atoms
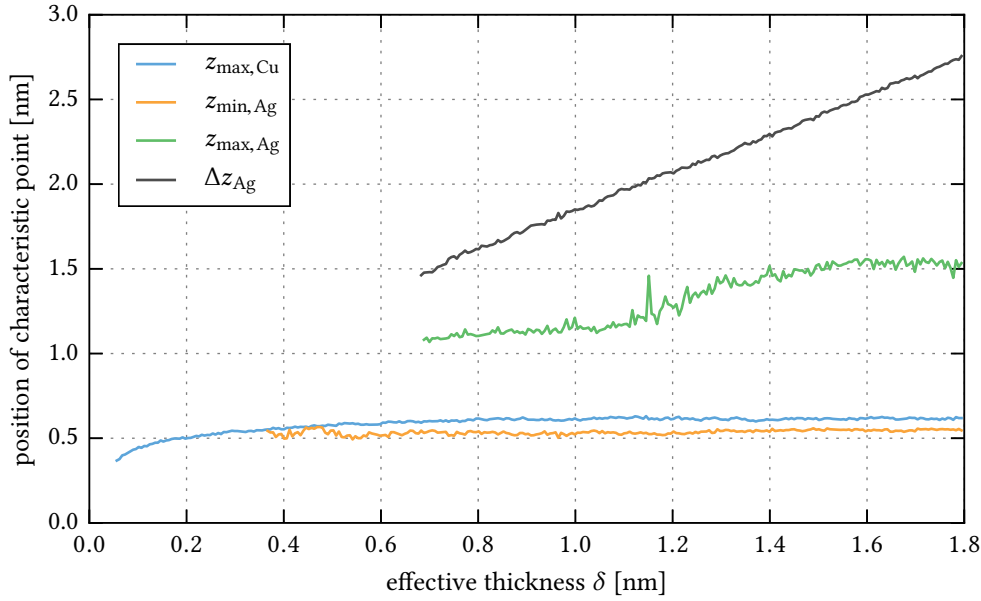
Figure 7.4.: Dependence of the values of the characteristic points $z_{\mathrm{max,Cu}}$, $z_{\mathrm{min,Ag}}$, $z_{\mathrm{max,Ag}}$ and Δz_{Ag} (defined in the body text) on the effective film thickness δ. To obtain greater accuracy, the points of the corresponding distribution functions $f_{\mathrm{Ag/Cu}}$ were interpolated with a cubic spline prior to the determination of the characteristic points.

tend to accumulate on the cluster surface; however, as compared to $\epsilon_{\mathrm{Ag}} = 0.5$, the latter effect is less pronounced and we cannot find the distinct intersections between the functions f_{Ag} and f_{Cu}. Instead, the tails of the functions are overlapping, and for all three δ-values, we still find more Cu atoms than Ag atoms at the bottoms of the clusters.

The other two rows of the figure reveal that the behavior discussed so far becomes different for large Ag contents. While the previous cases allow us to identify at least a weak separation of both phases, this becomes difficult or impossible for $\epsilon_{\mathrm{Ag}} = 0.7$ and 0.9. The amount of Ag atoms is so large that their presence dominates over the entire volume of the cluster. Instead of making out a distinct Cu-rich region in the cores of the clusters, we rather observe that the cluster states change over to a solid solution. However, we cannot attribute this transition to a specific value of ϵ_{Ag}. For example, the small drop of the function f_{Ag} at a height of 0.5 nm for $\epsilon_{\mathrm{Ag}} = 0.7$ and $\delta = 0.6$ nm still reveals a very weak depletion of Ag atoms in the center of the cluster; for the lower film thickness $\delta = 0.05$ nm, however, such a drop cannot be found.

7.4. Summary

In this chapter, we have shown how the MD simulations for the deposition of gold can be extended to the co-deposition of silver and copper. Making use of distribution functions and
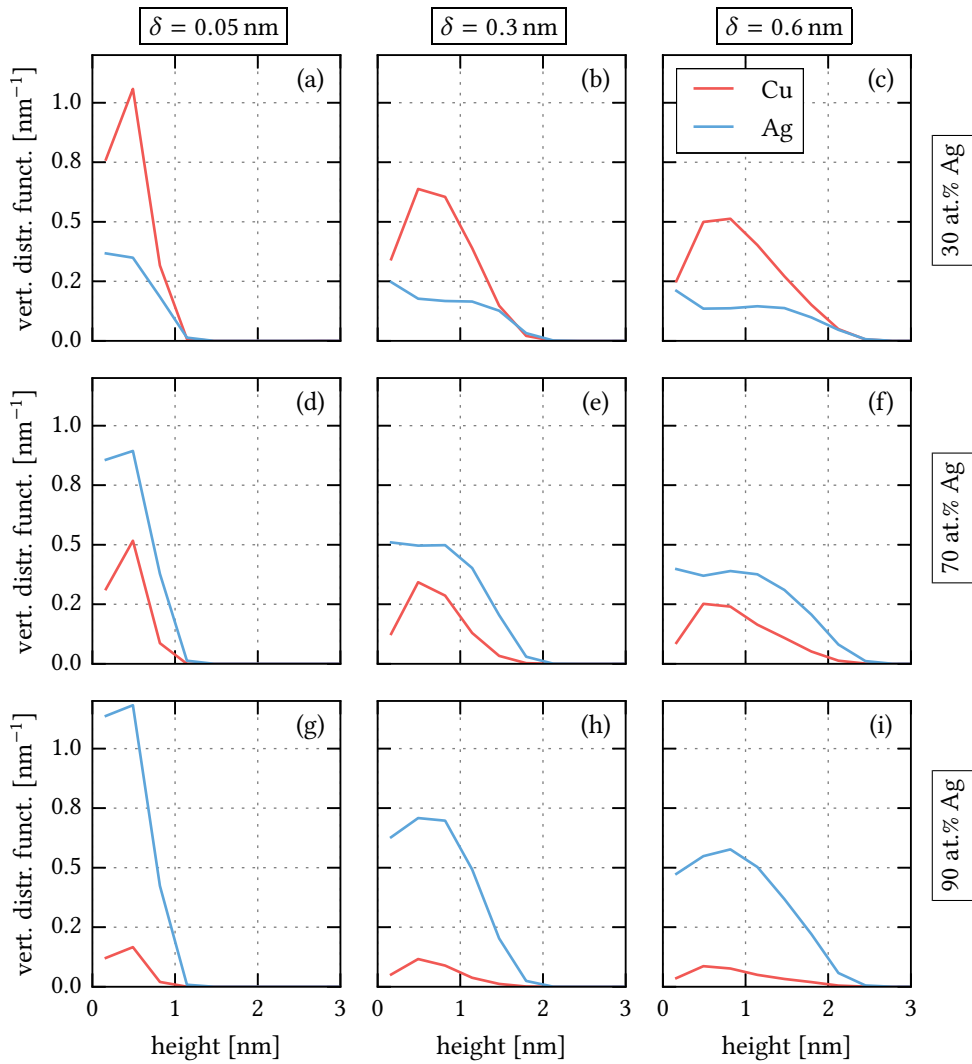
Figure 7.5.: Vertical distribution functions (perpendicular to the surface) of Ag and Cu atoms for three different values of the effective thickness δ. The data in each row has been obtained from one simulation run with Ag contents of 30 at.%, 70 at.% and 90 at.%, respectively. Adapted from [163].

graphical visualization of cluster configurations, we confirmed the expectation that silver atoms are preferentially located near the surface of the cluster. In particular, for an Ag content of 50 at.%, at least one monolayer of silver atoms was always present on the cluster surface. Nevertheless, the cluster configurations remained in all cases far from a perfect core–shell arrangement. In the following, we briefly discuss why further work is required to find out if and to what extent the simulations underestimate the degree of phase separation.

In Sec. 5.3, we have already explained that the rescaling procedure only affects the deposition

rate and the diffusion on the polymer surface (and in the polymer bulk). For small liquid clusters, all internal cluster processes should be sufficiently fast so that at least a weak separation is possible. For large solid clusters, however, we can expect that the rearrangement of the atoms is mainly driven by infrequent events, e. g., hops of atoms on the cluster surface or vacancy diffusion in the cluster bulk. As these very slow processes are not accelerated, it seems likely that the simulations underestimate the degree of phase separation—even though it has been reported that under certain conditions Ag–Cu clusters indeed remain in a metastable state [158]. Nevertheless, further work would be required to obtain reliable reference data that helps to answer the question how much stronger the phase separation would be in in actual experiment.

Chapter 8

Conclusions

The present work was concerned with computational investigations of the plasma-based formation of metal–polymer nanocomposites. In particular, two different experimental scenarios were covered: the first was the growth of metallic clusters and nanocolumns in a polymer host matrix during co-deposition of metal and polymer. The other scenario was the growth of a nanogranular metal film on a polymer substrate during the exclusive deposition of metal.

Even though different simulation techniques—kinetic Monte Carlo (KMC) and molecular dynamics (MD) simulations—were applied to treat both cases, one common goal of the approaches was to establish a model which describes the creation of surface defects during the deposition process. Such a model is required to account for highly energetic plasma particles which may impinge on the substrate during sputter deposition. In fact, the interaction of a plasma with the substrate may lead to other effects as well, e. g., the charging of clusters or the emission of secondary electrons, but none of the present models is currently able to describe them. In accordance with experimental findings, the surface defects were intended to limit the diffusion of atoms and clusters; yet, the respective implementations in the KMC and MD simulations schemes differed due to the nature of the methods. Presently, both presented KMC and MD models are still incapable of giving an exact microscopic representation of the way the defects are created, their appearance and their property to trap particles. For that reason, the treatment in the simulations must be understood as a rough approximation of the actual behavior. The advantage of the employed techniques is that the amount of defects can be easily varied in a broad range. Hence, there is a high chance that a realistic amount of trapped clusters can be achieved in the simulations. However, the choice of the defect parameters still requires a certain amount of guessing. Due to the lack of detailed experimental reference data, it remains so far impossible to map the simulation parameters to specific experimental conditions such as plasma parameters.

In the following, we separately recapitulate the findings from both employed simulation methods, and we point out several critical aspects that are specific to either KMC or MD.

Kinetic Monte Carlo simulations.   The work on KMC was performed to incorporate the creation of surface defects into the nanocolumnar growth model by Rosenthal *et al.* [34].

Concerning the question if the previously observed growth of nanocolumns [30] is also possible if sputter deposition is applied, the results give a comprehensive answer: a general trend displayed by many simulations was that an increase of the amount of defects leads to an increased amount of columns. At that, it was observed that the columns typically become thinner if a fixed amount of metal had to be distributed to a larger amount of columns. As opposed to this, however, the simulations also showed that very large amounts of defects may also lead to a reduction of even a complete suppression of columnar growth. If this is the case, the composite typically exhibits a large amount of trapped spherical clusters which have not reached the critical size that enables the columnar growth mode.

Another effect studied in this work was that of allowing clusters to diffuse in the polymer bulk. As the ratio between the surface and bulk diffusion coefficients of metal atoms must be guessed, this parameter was varied in a broad range. Even though it turned out that bulk diffusion may indeed have a strong influence—e. g., it generally leads to an increase of the number of columns—it was shown that the significance of the effects is restricted to very small ratios of the diffusion coefficients, which are expected to be far below realistic values. The neglect of bulk diffusion is thus justified for many practical applications.

All new aspects considered in this work could be easily integrated into the previous simulation model from Ref. [34]. In fact, such a flexibility, which pertains to many KMC models, is an important advantage of the method. In some cases, the flexibility to make quick changes to the model might even compensate for the uncertainties of the required parameters—for example, when the influence of certain processes can be assessed by performing comprehensive parameter scans. Even then, however, substantial improvements of the model usually require detailed comparisons with reliable reference data. Although the simulation model by Rosenthal *et al.* could be used to explain several effects that occurred in actual experiments [34–36], it still involved some approximations and guesses that have not yet been subject to detailed checks. Before further extensions of the model are made, it would thus be reasonable to make new comparisons with experiments. For example, the treatment of the defects in this work is consistent with the previous version of the model, but so far, no experimental work has been done to assess the specific findings.

Molecular dynamics simulations. Complementing the KMC simulations, the MD simulation scheme was developed because the atomistic treatment of the metal atoms allows one to dispense with the initial assumptions about possible cluster shapes. In fact, the step towards a microscopic treatment of the metal atoms is the main advantage over the KMC model; the description of the polymer, the surface defects and the re-evaporation of atoms relies on similarly simple models. The experimental scenario under consideration was the formation of a nanogranular metal film on a polymer substrate during sputter deposition.

In one part of this investigation, the focus was put on the time evolution of the film morphology resulting from the deposition of gold (Au) atoms. Although several aspects of the simulation model are based on rough assumptions, it was possible to bring the results into good agreement with experimental reference data from Ref. [61]. However, for none of the investigated parameter sets, all considered quantities agreed equally well. Furthermore, it was argued that the simulations may accumulate certain artifacts whose significance increases

with growing film thickness (see also below).

Another application of MD based on the simulation model for gold was the investigation of the phase-separation of silver–copper (Ag–Cu) clusters growing on a polymer surface during sputter deposition. Considering four different ratios of Ag and Cu deposition rates, a weak tendency of phase separation could be found in all cases. In particular, for an Ag content of 50 at.%, very small clusters already formed a thin Ag shell which persisted during the whole growth process. In the cores of the clusters, a small majority of Cu atoms was found, but both species remained largely intermixed.

The technical novelty of the MD simulation scheme is the treatment of the polymer substrate as a continuous medium in which and on which the metal atoms perform Langevin dynamics. It was claimed that the simulated behavior—which happens on time scales of nanoseconds—corresponds to the much slower behavior of an actual experiment if the simulations are performed with proportionally increased values of the diffusion coefficient and the deposition rate measured in that experiment. As a result of this, an effective boost factor of roughly 10^9 was achieved. It was explained that the rescaling method fails if it is inappropriate to assume that internal cluster processes happen instantaneously. Therefore, the treatment of large solid clusters, whose structure takes a long time to relax, is likely to introduce artifacts in the morphology. It still requires further work to determine accurate limits of the applicability of the method. For example, it would be particularly insightful if the atomic arrangement of individual clusters could be tracked on a long time scales, but the common experimental approaches still lack the ability to reach sufficiently high spatial and temporal resolutions at the same time. Alternatively, one could also resort the problem to complementary computational studies, but these have to overcome several challenges as well. On the one hand, one could try to apply one of the MD acceleration techniques mentioned in Sec. 3.2.4 to enforce the execution of infrequent events. Yet, it is still uncertain if all required processes can be accelerated and if a sufficiently long simulation time can be reached. On the other hand, it would also be possible to describe internal cluster processes with atomistic KMC simulations. As is typical of KMC studies, the main difficulty of such an approach lies in the acquirement of all required atomistic processes and the associated rates. First attempts in this direction have already been made, see, e. g., Refs. [164, 165], but the employed models are still very simple.

Appendix A

Curve Fitting Results

It is difficult to identify the maximum of the number density of clusters in the noisy experimental data from Ref. [61]. For this reason, the parameters a, b and δ_0 of the function

$$f(\delta) = a(\delta - \delta_0)^2 + b \tag{A.1}$$

have been fitted with the method of least squares so that f approximates the experimental data. For the fit, only the data with δ-values in the range $[0.02\,\text{nm}, 0.25\,\text{nm}]$ has been taken into account. The resulting curve f and the experimental data are shown in Fig. A.1. The maximum of the function f occurs at the point $(0.17\,\text{nm}, 1.58 \times 10^{13}\,\text{cm} - 2)$.
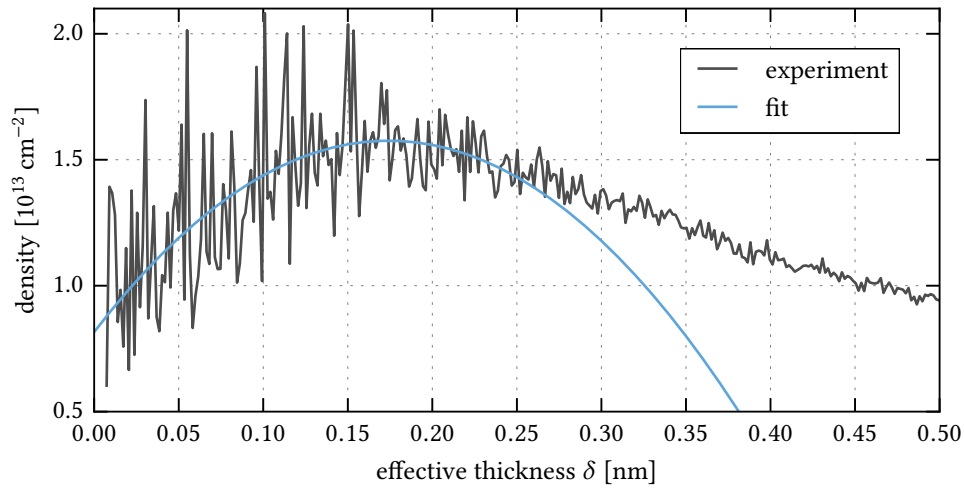

Figure A.1.: Number density of clusters from the experiment presented in Ref. [61], and the fitted curve f (Eq. (A.1)).

Bibliography

[1] R. P. Feynman, *There's plenty of room at the bottom [data storage]*, Journal of Micro-electromechanical Systems **1**, 60 (1992) (cit. on p. 1).

[2] A. D. Pomogailo, and V. N. Kestelman, *Metallopolymer Nanocomposites*, edited by R. Hull, R. M. Osgood, Jr., J. Parisi, and H. Warlimont, Springer Series in Materials Science (Springer Berlin Heidelberg, 2006) (cit. on pp. 1, 6).

[3] P. Ball, *Roll-up for the revolution*, Nature **414**, 60 (2001) (cit. on p. 1).

[4] S. Kaskel, *The Chemistry of Metal-Organic Frameworks: Synthesis, Characterization, and Applications* (Wiley, 2016) (cit. on p. 1).

[5] G. Guisbiers, S. Mejía-Rosales, and F. L. Deepak, *Nanomaterial Properties: Size and Shape Dependencies*, Journal of Nanomaterials **2012**, 1 (2012) (cit. on p. 1).

[6] I. Khan, K. Saeed, and I. Khan, *Nanoparticles: Properties, applications and toxicities*, Arabian Journal of Chemistry (in press) (2017) (cit. on p. 1).

[7] B. Calderón-Jiménez, M. E. Johnson, A. R. M. Bustos, K. E. Murphy, M. R. Winchester, and J. R. V. Baudrit, *Silver Nanoparticles: Technological Advances, Societal Impacts, and Metrological Challenges*, Frontiers in Chemistry **5**, 6 (2017) (cit. on p. 1).

[8] J. Mielke, S. Rades, E. Ortel, T. Salge, and V.-D. Hodoroaba, *Improved Spatial Resolution of EDX/SEM for the Elemental Analysis of Nanoparticles*, Microscopy and Microanalysis **21**, 1713 (2015) (cit. on p. 1).

[9] L. Rosenthal, *Kinetic Monte Carlo Simulations of Metal-Polymer Nanocomposite Formation*, PhD thesis (University of Kiel, 2013) (cit. on pp. 1, 2, 5, 6, 10–13, 15, 18, 19, 27, 28, 30, 32, 33, 35, 36, 38, 54).

[10] S. Khan, and L. Lorenzelli, *Recent advances of conductive nanocomposites in printed and flexible electronics*, Smart Materials and Structures **26**, 083001 (2017) (cit. on p. 1).

[11] M. K. Hedayati, M. Javaheri, A. U. Zillohu, H. J. El-Khozondar, M. S. Bawa'aneh, A. Lavrinenko, F. Faupel, and M. Elbahri, *Photo-driven Super Absorber as an Active Meta-material with a Tunable Molecular-Plasmonic Coupling*, Advanced Optical Materials **2**, 705 (2014) (cit. on p. 1).

[12] M. Karttunen, P. Ruuskanen, V. Pitkänen, and W. M. Albers, *Electrically Conductive Metal Polymer Nanocomposites for Electronics Applications*, English, J. Electron. Mater. **37**, 951 (2008) (cit. on p. 1).

[13] H. Takele, S. Jebril, T. Strunskus, V. Zaporojtchenko, R. Adelung, and F. Faupel, *Tuning of electrical and structural properties of metal-polymer nanocomposite films prepared by co-evaporation technique*, Appl. Phys. A **92**, 345 (2008) (cit. on p. 1).

[14] H. Graf, J. Vancea, and H. Hoffmann, *Single-electron tunneling at room temperature in cobalt nanoparticles*, Applied Physics Letters **80**, 1264 (2002) (cit. on p. 1).

[15] T. A. Fulton, and G. J. Dolan, *Observation of single-electron charging effects in small tunnel junctions*, Physical Review Letters **59**, 109 (1987) (cit. on p. 1).

[16] M. Hedayati, F. Faupel, and M. Elbahri, *Review of Plasmonic Nanocomposite Metamaterial Absorber*, Materials **7**, 1221 (2014) (cit. on p. 1).

[17] C. Etrich, S. Fahr, M. Hedayati, F. Faupel, M. Elbahri, and C. Rockstuhl, *Effective Optical Properties of Plasmonic Nanocomposites*, Materials **7**, 727 (2014) (cit. on p. 1).

[18] A. Biswas, O. Aktas, J. Kanzow, U. Saeed, T. Strunskus, V. Zaporojtchenko, and F. Faupel, *Polymer–metal optical nanocomposites with tunable particle plasmon resonance prepared by vapor phase co-deposition*, Mater. Lett. **58**, 1530 (2004) (cit. on p. 1).

[19] A. Biswas, O. Aktas, U. Schürmann, U. Saeed, V. Zaporojtchenko, F. Faupel, and T. Strunskus, *Tunable multiple plasmon resonance wavelengths response from multicomponent polymer-metal nanocomposite systems*, Applied Physics Letters **84**, 2655 (2004) (cit. on p. 1).

[20] M. Carbone, D. T. Donia, G. Sabbatella, and R. Antiochia, *Silver nanoparticles in polymeric matrices for fresh food packaging*, Journal of King Saud University - Science **28**, 273 (2016) (cit. on p. 1).

[21] A. Emamifar, *Applications of Antimicrobial Polymer Nanocomposites in Food Packaging*, edited by A. Haschim, Advances in Nanocomposite Technology (InTech, 2011) (cit. on p. 1).

[22] H. M. C. de Azeredo, *Nanocomposites for food packaging applications*, Food Research International **42**, 1240 (2009) (cit. on p. 1).

[23] R. Benzaid, J. Chevalier, M. Saâdaoui, G. Fantozzi, M. Nawa, L. A. Diaz, and R. Torrecillas, *Fracture toughness, strength and slow crack growth in a ceria stabilized zirconia–alumina nanocomposite for medical applications*, Biomaterials **29**, 3636 (2008) (cit. on p. 1).

[24] F. Faupel, V. Zaporojtchenko, H. Greve, U. Schürmann, V. S. K. Chakravadhanula, C. Hanisch, A. Kulkarni, A. Gerber, E. Quandt, and R. Podschun, *Deposition of Nanocomposites by Plasmas*, Contributions to Plasma Physics **47**, 537 (2007) (cit. on pp. 1, 6).

[25] F.-R. F. Fan, and A. J. Bard, *Chemical, Electrochemical, Gravimetric and Microscopic Studies on Antimicrobial Silver Films*, The Journal of Physical Chemistry B **106**, 279 (2002) (cit. on p. 1).

[26] F. Faupel, V. Zaporojtchenko, T. Strunskus, and M. Elbahri, *Metal-Polymer Nanocomposites for Functional Applications*, Advanced Engineering Materials **12**, 1177 (2010) (cit. on pp. 1, 5, 6).

[27] L. Nicolais, and G. Carotenuto, eds., *Metal-Polymer Nanocomposites* (John Wiley & Sons, Inc., Nov. 2004) (cit. on p. 1).

[28] F. Faupel, V. Zaporojtchenko, T. Strunskus, J. Erichsen, K. Dolgner, A. Thran, and M. Kiene, *Fundamental Aspects of Polymer Metallization*, in *Metallization of Polymers 2* (Springer, Boston, MA, 2002), pp. 73–96 (cit. on p. 1).

[29] G. V. Ramesh, S. Porel, and T. P. Radhakrishnan, *Polymer thin films embedded with in situ grown metal nanoparticles*, Chem. Soc. Rev. **38**, 2646 (2009) (cit. on p. 1).

[30] H. Greve, A. Biswas, U. Schürmann, V. Zaporojtchenko, and F. Faupel, *Self-organization of ultrahigh-density Fe–Ni–Co nanocolumns in Teflon® AF*, Applied Physics Letters **88**, 123103, (2006) (cit. on pp. 1, 2, 6, 11, 27, 30, 114).

[31] Q. Wang, and L. Zhu, *ACS Symposium Series 1034, Functional polymer nanocomposites for energy storage and conversion* (American Chemical Society, Washington D.C., 2010) (cit. on p. 1).

[32] M. Schwartzkopf, A. Buffet, V. Körstgens, E. Metwalli, K. Schlage, G. Benecke, J. Perlich, M. Rawolle, A. Rothkirch, B. Heidmann, G. Herzog, P. Müller-Buschbaum, R. Röhlsberger, R. Gehrke, N. Stribeck, and S. V. Roth, *From atoms to layers: in situ gold cluster growth kinetics during sputter deposition*, Nanoscale **5**, 5053 (2013) (cit. on pp. 1, 9, 56, 77).

[33] C.-C. Chen, C. Zhu, E. R. White, C.-Y. Chiu, M. C. Scott, B. C. Regan, L. D. Marks, Y. Huang, and J. Miao, *Three-dimensional imaging of dislocations in a nanoparticle at atomic resolution*, Nature **496**, 74 (2013) (cit. on p. 1).

[34] L. Rosenthal, H. Greve, V. Zaporojtchenko, T. Strunskus, F. Faupel, and M. Bonitz, *Formation of magnetic nanocolumns during vapor phase deposition of a metal-polymer nanocomposite: Experiments and kinetic Monte Carlo simulations*, Journal of Applied Physics **114**, 044305 (2013) (cit. on pp. 1, 2, 5, 6, 11, 19, 23, 27, 30, 35, 36, 38, 54, 113, 114).

[35] M. Bonitz, L. Rosenthal, K. Fujioka, V. Zaporojtchenko, F. Faupel, and H. Kersten, *Towards a Particle Based Simulation of Complex Plasma Driven Nanocomposite Formation*, Contributions to Plasma Physics **52**, 890 (2012) (cit. on pp. 1, 2, 6, 12, 19, 54, 114).

[36] L. Rosenthal, A. Filinov, M. Bonitz, V. Zaporojtchenko, and F. Faupel, *Diffusion and Growth of Metal Clusters in Nanocomposites: A Kinetic Monte Carlo Study*, Contributions to Plasma Physics **51**, 971 (2011) (cit. on pp. 1, 2, 5, 12, 19, 33, 35, 54, 114).

[37] R. Rozas, and T. Kraska, *Formation of metal nano-particles on and in polymer films investigated by molecular dynamics simulation*, Nanotechnology **18**, 165706 (2007) (cit. on pp. 1, 3).

[38] A. Thran, and F. Faupel, *Computer Simulation of Metal Diffusion in Polymers*, Defect and Diffusion Forum (Trans Tech Publications) **143**, 903 (1997) (cit. on pp. 1, 2, 11, 12).

[39] K. Fujioka, *Kinetic Monte Carlo Simulations of Cluster Growth in Magnetron Plasmas*, PhD thesis (University of Kiel, 2015) (cit. on pp. 1, 6, 11, 90, 93).

[40] D. M. Mattox, *Handbook of Physical Vapor Deposition (PVD) Processing* (Elsevier, Amsterdam, 2010) (cit. on p. 1).

[41] M. Bonitz, N. Horing, and P. Ludwig, eds., *Introduction to Complex Plasmas*, Vol. 59, Springer Series on Atomic, Optical and Plasma Physics (Springer Berlin Heidelberg, 2010) (cit. on pp. 2, 20, 21).

[42] M. Bonitz, J. Lopez, K. Becker, and H. Thomsen, eds., *Complex Plasmas: Scientific Challenges and Technological Opportunities*, Vol. 82, Springer Series on Atomic, Optical and Plasma Physics (Springer, Cham, 2014) (cit. on p. 2).

[43] P. Kratzer, "Monte Carlo and Kinetic Monte Carlo Methods – A Tutorial", in *Multiscale Simulation Methods in Molecular Sciences, Lecture Notes*, Vol. 42, NIC series (John von Neumann Institute for Computing, Jülich, 2009), pp. 51–76 (cit. on pp. 2, 15, 16, 18).

[44] W. Brenig, and E. Pehlke, *Reaction dynamics of H2 on Si. Ab initio supported model calculations*, Progress in Surface Science **83**, 263 (2008) (cit. on p. 2).

[45] N. Schlünzen, and M. Bonitz, *Nonequilibrium Green Functions Approach to Strongly Correlated Fermions in Lattice Systems*, Contributions to Plasma Physics **56**, 5 (2016) (cit. on p. 2).

[46] K. Balzer, N. Schlünzen, and M. Bonitz, *Stopping dynamics of ions passing through correlated honeycomb clusters*, Physical Review B **94**, 245118 (2016) (cit. on p. 2).

[47] M. Bonitz, *Quantum Kinetic Theory* (Springer International Publishing, Cham, 2016) (cit. on p. 2).

[48] L. Rosenthal, T. Strunskus, F. Faupel, J. W. Abraham, and M. Bonitz, "Kinetic Monte Carlo Simulations of Cluster Growth and Diffusion in Metal-Polymer Nanocomposites", in *Complex Plasmas: Scientific Challenges and Technological Opportunities*, Vol. 82, edited by M. Bonitz, J. Lopez, K. Becker, and H. Thomsen, Springer Series on Atomic, Optical and Plasma Physics (Springer, Cham, 2014), pp. 321–370 (cit. on pp. 2, 6, 10, 12, 13, 27, 28).

[49] *Blender - a 3D modelling and rendering package*, Blender Foundation (Blender Institute, Amsterdam, http://www.blender.org) (cit. on p. 2).

[50] E. C. Neyts, and P. Brault, *Molecular Dynamics Simulations for Plasma-Surface Interactions*, Plasma Processes and Polymers **14**, 1600145 (2016) (cit. on pp. 2, 3, 20, 23, 24).

[51] D. Perez, B. P. Uberuaga, Y. Shim, J. G. Amar, and A. F. Voter, in *Chapter 4 Accelerated Molecular Dynamics Methods: Introduction and Recent Developments*, Vol. 5, edited by R. A. Wheeler, Annu. Rep. Comput. Chem. (Elsevier, Amsterdam, 2009), pp. 79–98 (cit. on pp. 2, 24).

[52] A. Filinov, M. Bonitz, and D. Loffhagen, *Microscopic modeling of gas-surface scattering. I. A combined molecular dynamics-rate equation approach*, submitted to Plasma Sources Science and Technology, preprint available under arXiv:1802.03466 [cond-mat.stat-mech] (2018) (cit. on pp. 3, 25).

[53] A. Filinov, M. Bonitz, and D. Loffhagen, *Microscopic modeling of gas-surface scattering. II. Application to argon atom adsorption on a platinum (111) surface*, submitted to Plasma Sources Science and Technology, preprint available under arXiv:1802.01985 [physics.plasm-ph] (2018) (cit. on pp. 3, 25).

[54] K. M. Bal, and E. C. Neyts, *Merging Metadynamics into Hyperdynamics: Accelerated Molecular Simulations Reaching Time Scales from Microseconds to Seconds*, Journal of Chemical Theory and Computation **11**, 4545 (2015) (cit. on pp. 3, 23, 24).

[55] A. F. Voter, F. Montalenti, and T. C. Germann, *Extending the Time Scale in Atomistic Simulation of Materials*, Annual Review of Materials Research **32**, 321 (2002) (cit. on pp. 3, 20, 23–25).

[56] J. C. Tully, G. H. Gilmer, and M. Shugard, *Molecular dynamics of surface diffusion. I. The motion of adatoms and clusters*, The Journal of Chemical Physics **71**, 1630 (1979) (cit. on p. 3).

[57] A. Patti, *Molecular Dynamics of Spherical Nanoparticles in Dense Polymer Melts*, The Journal of Physical Chemistry B **118**, 3731 (2014) (cit. on p. 3).

[58] C. Luo, and J.-U. Sommer, *Coding coarse grained polymer model for LAMMPS and its application to polymer crystallization*, Computer Physics Communications **180**, 1382 (2009) (cit. on p. 3).

[59] J. G. D. Ochoa, K. Binder, and W. Paul, *Molecular dynamics simulations of the embedding of a nano-particle into a polymer film*, Journal of Physics: Condensed Matter **18**, 2777 (2006) (cit. on p. 3).

[60] L. Xie, P. Brault, C. Coutanceau, J.-M. Bauchire, A. Caillard, S. Baranton, J. Berndt, and E. C. Neyts, *Efficient amorphous platinum catalyst cluster growth on porous carbon: A combined molecular dynamics and experimental study*, Applied Catalysis B: Environmental **162**, 21 (2015) (cit. on p. 3).

[61] M. Schwartzkopf, G. Santoro, C. J. Brett, A. Rothkirch, O. Polonskyi, A. Hinz, E. Metwalli, Y. Yao, T. Strunskus, F. Faupel, P. Müller-Buschbaum, and S. V. Roth, *Real-Time Monitoring of Morphology and Optical Properties during Sputter Deposition for Tailoring Metal–Polymer Interfaces*, ACS Applied Materials & Interfaces **7**, 13547 (2015) (cit. on pp. 3, 5, 9, 11, 12, 55, 56, 62, 65, 68, 70, 73, 74, 76–82, 84, 85, 100, 114, 117).

[62] H. T. Beyene, V. S. K. Chakravadhanula, C. Hanisch, T. Strunskus, V. Zaporojtchenko, M. Elbahri, and F. Faupel, *Vapor Phase Deposition, Structure, and Plasmonic Properties of Polymer-Based Composites Containing Ag–Cu Bimetallic Nanoparticles*, Plasmonics **7**, 107 (2012) (cit. on pp. 3, 99, 100).

[63] M. Chandross, *Energetics of the formation of Cu–Ag core–shell nanoparticles*, Modelling and Simulation in Materials Science and Engineering **22**, 075012 (2014) (cit. on pp. 3, 99, 102, 105).

[64] V. Zaporojtchenko, T. Strunskus, K. Behnke, C. Bechtolsheim, A. Thran, and F. Faupel, *Formation of metal–polymer interfaces by metal evaporation: influence of deposition parameters and defects*, Microelectronic Engineering **50**, 465 (2000) (cit. on pp. 5, 12, 13).

[65] H. Greve, *Magnetische Metall/Polymer Nanokomposite für Hochfrequenzanwendungen*, PhD thesis (University of Kiel, 2007) (cit. on pp. 5, 6).

[66] O. Polonskyi, P. Solař, O. Kylián, M. Drábik, A. Artemenko, J. Kousal, J. Hanuš, J. Pešička, I. Matolínová, E. Kolíbalová, D. Slavínská, and H. Biederman, *Nanocomposite metal/plasma polymer films prepared by means of gas aggregation cluster source*, Thin Solid Films **520**, 4155 (2012) (cit. on p. 6).

[67] H. Urbassek, *Sputtering of molecules*, Nuclear Instruments and Methods in Physics Research Section B: Beam Interactions with Materials and Atoms **18**, 587 (1986) (cit. on p. 6).

[68] D. Depla, and S. Mahieu, eds., *Reactive sputter deposition*, Springer Series in materials science (Springer-Verlag Berlin Heidelberg, 2008) (cit. on p. 6).

[69] H. Biederman, *RF sputtering of polymers and its potential application*, Vacuum **59**, Proceedings of the Fifth International Symposium on Sputtering and Plasma Processes, 594 (2000) (cit. on p. 6).

[70] H. Biederman, *Nanocomposites and nanostructures based on plasma polymers*, Surface and Coatings Technology **205**, PSE 2010 Special Issue, S10 (2011) (cit. on p. 6).

[71] K. Norrman, A. Ghanbari-Siahkali, and N. B. Larsen, *6 Studies of spin-coated polymer films*, Annual Reports Section "C" (Physical Chemistry) **101**, 174 (2005) (cit. on p. 7).

[72] M. Schwartzkopf, and S. Roth, *Investigating Polymer–Metal Interfaces by Grazing Incidence Small-Angle X-Ray Scattering from Gradients to Real-Time Studies*, Nanomaterials **6**, 239 (2016) (cit. on pp. 7, 8).

[73] J. R. Levine, J. B. Cohen, Y. W. Chung, and P. Georgopoulos, *Grazing-incidence small-angle X-ray scattering: new tool for studying thin film growth*, Journal of Applied Crystallography **22**, 528 (1989) (cit. on p. 7).

[74] R. Lazzari, *IsGISAXS: a program for grazing-incidence small-angle X-ray scattering analysis from supported islands*, Journal of Applied Crystallography **35**, 406 (2002) (cit. on pp. 7–10, 84).

[75] P. Müller-Buschbaum, *Grazing incidence small-angle X-ray scattering: an advanced scattering technique for the investigation of nanostructured polymer films*, Analytical and Bioanalytical Chemistry **376**, 3 (2003) (cit. on p. 7).

[76] C. Durniak, M. Ganeva, G. Pospelov, W. V. Herck, and J. Wuttke, *BornAgain – Software for simulating and fitting X-ray and neutron small-angle scattering at grazing incidence*, http://www.bornagainproject.org/ (2015) (cit. on pp. 9, 85).

[77] M. Volmer, and A. Weber, *Keimbildung in übersättigten Gebilden*, Zeitschrift für Physikalische Chemie **119U**, 277 (1926) (cit. on p. 10).

[78] V. Zaporojtchenko, K. Behnke, A. Thran, T. Strunskus, and F. Faupel, *Condensation coefficients and initial stages of growth for noble metals deposited onto chemically different polymer surfaces*, Applied Surface Science **144-145**, 355 (1999) (cit. on p. 11).

[79] K. K. Nanda, *Size-dependent melting of nanoparticles: Hundred years of thermodynamic model*, Pramana **72**, 617 (2009) (cit. on p. 11).

[80]   B. M. Smirnov, *Cluster processes in gases and plasmas* (John Wiley & Sons, 2009) (cit. on p. 11).

[81]   G. Antczak, and G. Ehrlich, *Surface Diffusion: Metals, Metal Atoms, and Clusters* (Cambridge University Press, Cambridge, 2010) (cit. on p. 11).

[82]   F. Faupel, V. Zaporojtchenko, A. Thran, T. Strunskus, and M. Kiene, *Metal Diffusion in Polymers and on Polymer Surfaces*, in *Diffusion Processes in Advanced Technological Materials*, edited by D. Gupta, (Springer Berlin Heidelberg, 2005), pp. 333–363 (cit. on p. 12).

[83]   A. Thran, T. Strunskus, V. Zaporojtchenko, and F. Faupel, *Evidence of noble metal diffusion in polymers at room temperature and its retardation by a chromium barrier*, Applied Physics Letters **81**, 244 (2002) (cit. on p. 12).

[84]   G. Jeffers, M. Dubson, and P. Duxbury, *Island-to-percolation transition during growth of metal films*, Journal of Applied Physics **75**, 5016 (1994) (cit. on pp. 12, 62).

[85]   M. H. Cohen, and D. Turnbull, *Molecular Transport in Liquids and Glasses*, The Journal of Chemical Physics **31**, 1164 (1959) (cit. on pp. 12, 33).

[86]   J. S. Vrentas, and J. L. Duda, *Diffusion in polymer–solvent systems. I. Reexamination of the free-volume theory*, Journal of Polymer Science: Polymer Physics Edition **15**, 403 (1977) (cit. on pp. 12, 33).

[87]   J. S. Vrentas, and J. L. Duda, *Diffusion in polymer–solvent systems. II. A predictive theory for the dependence of diffusion coefficients on temperature, concentration, and molecular weight*, Journal of Polymer Science: Polymer Physics Edition **15**, 417 (1977) (cit. on pp. 12, 33).

[88]   J. S. Vrentas, and J. L. Duda, *Diffusion in polymer–solvent systems. III. Construction of Deborah number diagrams*, Journal of Polymer Science: Polymer Physics Edition **15**, 441 (1977) (cit. on pp. 12, 33).

[89]   J. Vrentas, and C. Vrentas, *Predictive methods for self-diffusion and mutual diffusion coefficients in polymer–solvent systems*, European Polymer Journal **34**, 797 (1998) (cit. on pp. 12, 33).

[90]   V. Zaporojtchenko, K. Behnke, T. Strunskus, and F. Faupel, *Condensation coefficients of noble metals on polymers: a novel method of determination by x-ray photoelectron spectroscopy*, Surface and Interface Analysis **30**, 439 (2000) (cit. on p. 12).

[91]   A. P. J. Jansen, *An Introduction to Kinetic Monte Carlo Simulations of Surface Reactions*, Lecture notes in physics (Springer, Berlin, Heidelberg, 2012) (cit. on pp. 15, 17, 18).

[92]   A. Chatterjee, and D. G. Vlachos, *An overview of spatial microscopic and accelerated kinetic Monte Carlo methods*, Journal of Computer-Aided Materials Design **14**, 253 (2007) (cit. on p. 15).

[93]   C. C. Battaile, *The Kinetic Monte Carlo method: Foundation, implementation, and application*, Computer Methods in Applied Mechanics and Engineering **197**, 3386 (2008) (cit. on p. 15).

[94]   A. F. Voter, "Introduction to the Kinetic Monte Carlo Method", in *Radiation effects in solids*, edited by K. E. Sickafus, E. A. Kotomin, and B. P. Uberuaga, (Springer Netherlands, Dordrecht, 2007), pp. 1–23 (cit. on pp. 15, 17, 20).

[95]   A. B. Bortz, M. H. Kalos, and J. L. Lebowitz, *A new algorithm for Monte Carlo simulation of Ising spin systems*, Journal of Computational Physics **17**, 10 (1975) (cit. on p. 17).

[96]   D. T. Gillespie, *A general method for numerically simulating the stochastic time evolution of coupled chemical reactions*, Journal of Computational Physics **22**, 403 (1976) (cit. on p. 18).

[97]   D. T. Gillespie, *Exact stochastic simulation of coupled chemical reactions*, The Journal of Physical Chemistry **81**, 2340 (1977) (cit. on p. 18).

[98]   D. T. Gillespie, *Monte Carlo simulation of random walks with residence time dependent transition probability rates*, Journal of Computational Physics **28**, 395 (1978) (cit. on p. 18).

[99]   S. Plimpton, C. Battaile, M. Chandross, L. Holm, A. Thompson, V. Tikare, G. Wagner, E. Webb, X. Zhou, C. G. Cardona, et al., *Crossing the mesoscale no-man's land via parallel kinetic Monte Carlo*, Sandia Report SAND2009-6226 (2009) (cit. on pp. 19, 23).

[100]   M. Leetmaa, and N. V. Skorodumova, *KMCLib: A general framework for lattice kinetic Monte Carlo (KMC) simulations*, Computer Physics Communications **185**, 2340 (2014) (cit. on p. 19).

[101]   R. Marcelin, *Contribution à l'étude de la cinétique physico-chimique*, Annales de physique **3**, 120 (1915) (cit. on pp. 19, 24).

[102]   H. Eyring, *The Activated Complex in Chemical Reactions*, J. Chem. Phys. **3**, 107 (1935) (cit. on pp. 19, 24).

[103]   K. Pötting, W. Schmickler, and T. Jacob, *Self-Diffusion on Au(100): A Density Functional Theory Study*, ChemPhysChem **11**, 1395 (2010) (cit. on p. 19).

[104]   S. Maeda, T. Taketsugu, and K. Morokuma, *Exploring transition state structures for intramolecular pathways by the artificial force induced reaction method*, Journal of Computational Chemistry **35**, 166 (2013) (cit. on p. 20).

[105]   B. J. Alder, and T. E. Wainwright, *Phase Transition for a Hard Sphere System*, The Journal of Chemical Physics **27**, 1208 (1957) (cit. on p. 20).

[106]   B. J. Alder, and T. E. Wainwright, *Studies in Molecular Dynamics. I. General Method*, The Journal of Chemical Physics **31**, 459 (1959) (cit. on p. 20).

[107]   M. Griebel, S. Knapek, and G. Zumbusch, *Numerical Simulation in Molecular Dynamics, Numerics, Algorithms, Parallelization, Applications*, Vol. 5, Texts in Computational Science and Engineering (Springer-Verlag, Berlin, Heidelberg, 2007) (cit. on p. 20).

[108]   H. Kählert, *Dynamics of a spherically confined Yukawa plasma: shell formation and collective excitations*, PhD thesis (University of Kiel, 2011) (cit. on pp. 20, 23).

[109]   Y. K. Shin, T.-R. Shan, T. Liang, M. J. Noordhoek, S. B. Sinnott, A. C. van Duin, and S. R. Phillpot, *Variable charge many-body interatomic potentials*, MRS Bulletin **37**, 504 (2012) (cit. on p. 21).

[110] T. Liang, Y. K. Shin, Y.-T. Cheng, D. E. Yilmaz, K. G. Vishnu, O. Verners, C. Zou, S. R. Phillpot, S. B. Sinnott, and A. C. van Duin, *Reactive Potentials for Advanced Atomistic Simulations*, Annual Review of Material Science **43**, 109 (2013) (cit. on pp. 21, 22).

[111] P. Ballone, *Modeling Potential Energy Surfaces: From First-Principle Approaches to Empirical Force Fields*, Entropy **16**, 322 (2013) (cit. on p. 21).

[112] K. Farah, F. Müller-Plathe, and M. C. Böhm, *Classical Reactive Molecular Dynamics Implementations: State of the Art*, ChemPhysChem **13**, 1127 (2012) (cit. on p. 21).

[113] A. D. Mackerell, *Empirical force fields for biological macromolecules: Overview and issues*, Journal of Computational Chemistry **25**, 1584 (2004) (cit. on p. 21).

[114] S. Nosé, *A unified formulation of the constant temperature molecular dynamics methods*, The Journal of Chemical Physics **81**, 511 (1984) (cit. on p. 21).

[115] W. G. Hoover, *Canonical dynamics: Equilibrium phase-space distributions*, Physical Review A **31**, 1695 (1985) (cit. on p. 21).

[116] H. J. C. Berendsen, J. P. M. Postma, W. F. van Gunsteren, A. DiNola, and J. R. Haak, *Molecular dynamics with coupling to an external bath*, The Journal of Chemical Physics **81**, 3684 (1984) (cit. on p. 21).

[117] P. Langevin, *Sur la théorie du mouvement brownien*, Comptes rendus de l'Académie des sciences (Paris) **146**, 530 (1908) (cit. on p. 21).

[118] T. Schneider, and E. Stoll, *Molecular-dynamics study of a three-dimensional one-component model for distortive phase transitions*, Physical Review B **17**, 1302 (1978) (cit. on p. 21).

[119] B. Dünweg, and W. Paul, *Brownian dynamics simulations without Gaussian random numbers*, International Journal of Modern Physics C **02**, 817 (1991) (cit. on p. 21).

[120] J. L. García-Palacios, *Introduction to the theory of stochastic processes and Brownian motion problems*, arXiv:cond-mat/0701242 [cond-mat.stat-mech] (2007) (cit. on p. 21).

[121] M. S. Daw, and M. I. Baskes, *Semiempirical, Quantum Mechanical Calculation of Hydrogen Embrittlement in Metals*, Physical Review Letters **50**, 1285 (1983) (cit. on p. 21).

[122] M. S. Daw, and M. I. Baskes, *Embedded-atom method: Derivation and application to impurities, surfaces, and other defects in metals*, Physical Review B **29**, 6443 (1984) (cit. on p. 21).

[123] M. S. Daw, S. M. Foiles, and M. I. Baskes, *The embedded-atom method: a review of theory and applications*, Materials Science Reports **9**, 251 (1993) (cit. on p. 22).

[124] M. I. Baskes, *Application of the Embedded-Atom Method to Covalent Materials: A Semiempirical Potential for Silicon*, Physical Review Letters **59**, 2666 (1987) (cit. on p. 22).

[125] S. M. Foiles, M. I. Baskes, and M. S. Daw, *Embedded-atom-method functions for the fcc metals Cu, Ag, Au, Ni, Pd, Pt and their alloys*, Physical Review B **33**, 7983 (1986) (cit. on pp. 22, 59).

[126] H. Thomsen, *Melting Processes and Laser Manipulation of Strongly Coupled Yukawa Systems*, PhD thesis (University of Kiel, 2015) (cit. on p. 23).

[127] W. C. Swope, H. C. Andersen, P. H. Berens, and K. R. Wilson, *A computer simulation method for the calculation of equilibrium constants for the formation of physical clusters of molecules: Application to small water clusters*, The Journal of Chemical Physics **76**, 637 (1982) (cit. on p. 23).

[128] L. Verlet, *Computer "Experiments" on Classical Fluids. I. Thermodynamical Properties of Lennard-Jones Molecules*, Physical Review **159**, 98 (1967) (cit. on p. 23).

[129] J. W. Hewage, *Core/shell formation and surface segregation of multi shell icosahedral silver-palladium bimetallic nanostructures: A dynamic and thermodynamic study*, Materials Chemistry and Physics **174**, 187 (2016) (cit. on p. 23).

[130] E. C. Neyts, and A. Bogaerts, *Combining molecular dynamics with Monte Carlo simulations: implementations and applications*, Theoretical Chemistry Accounts **132**, 2 (2012) (cit. on pp. 23, 24).

[131] A. F. Voter, *Hyperdynamics: Accelerated Molecular Dynamics of Infrequent Events*, Physical Review Letters **78**, 3908 (1997) (cit. on p. 24).

[132] K. A. Fichthorn, R. A. Miron, Y. Wang, and Y. Tiwary, *Accelerated molecular dynamics simulation of thin-film growth with the bond-boost method*, Journal of Physics: Condensed Matter **21**, 084212 (2009) (cit. on p. 24).

[133] A. Laio, and M. Parrinello, *Escaping free-energy minima*, Proceedings of the National Academy of Sciences of the United States of America **99**, 12562 (2002) (cit. on p. 24).

[134] A. Laio, and F. L. Gervasio, *Metadynamics: a method to simulate rare events and reconstruct the free energy in biophysics, chemistry and material science*, Reports on Progress in Physics **71**, 126601 (2008) (cit. on p. 24).

[135] K. M. Bal, and E. C. Neyts, *Direct observation of realistic-temperature fuel combustion mechanisms in atomistic simulations*, Chemical Science **7**, 5280 (2016) (cit. on p. 24).

[136] M. R. Sørensen, and A. F. Voter, *Temperature-accelerated dynamics for simulation of infrequent events*, J. Chem. Phys. **112**, 9599 (2000) (cit. on p. 24).

[137] A. F. Voter, *Parallel replica method for dynamics of infrequent events*, Physical Review B **57**, R13985 (1998) (cit. on p. 25).

[138] B. P. Uberuaga, S. J. Stuart, and A. F. Voter, *Parallel replica dynamics for driven systems: Derivation and application to strained nanotubes*, Physical Review B **75**, 014301 (2007) (cit. on p. 25).

[139] S. Plimpton, *Fast Parallel Algorithms for Short-Range Molecular Dynamics*, J. Comp. Phys. **117**, 1 (1995) (cit. on p. 26).

[140] A. Stukowski, *Visualization and analysis of atomistic simulation data with OVITO–the Open Visualization Tool*, Modelling and Simulation in Materials Science and Engineering **18**, 015012 (2010) (cit. on p. 26).

[141] J. W. Abraham, N. Kongsuwan, T. Strunskus, F. Faupel, and M. Bonitz, *Simulation of nanocolumn formation in a plasma environment*, Journal of Applied Physics **117**, 014305 (2015) (cit. on pp. 28, 37, 44–46, 48, 52).

[142] B. M. Smirnov, *Clusters and Small Particles*, Vol. 1, Graduate Texts in Contemporary Physics (Springer-Verlag New York, 2000) (cit. on pp. 30, 92).

[143] A. Thran, M. Kiene, V. Zaporojtchenko, and F. Faupel, *Condensation Coefficients of Ag on Polymers*, Physical Review Letters **82**, 1903 (1999) (cit. on p. 33).

[144] E. Main, T. Karabacak, and T. M. Lu, *Continuum model for nanocolumn growth during oblique angle deposition*, Journal of Applied Physics **95**, 4346 (2004) (cit. on p. 40).

[145] J. W. Abraham, T. Strunskus, F. Faupel, and M. Bonitz, *Molecular dynamics simulation of gold cluster growth during sputter deposition*, Journal of Applied Physics **119**, 185301 (2016) (cit. on pp. 57, 73, 78, 82, 85).

[146] T. Karabacak, J. P. Singh, Y.-P. Zhao, G.-C. Wang, and T.-M. Lu, *Scaling during shadowing growth of isolated nanocolumns*, Physical Review B **68**, 125408 (2003) (cit. on p. 58).

[147] Y. Shim, and J. G. Amar, *Effects of Shadowing in Oblique-Incidence Metal (100) Epitaxial Growth*, Physical Review Letters **98**, 046103 (2007) (cit. on p. 58).

[148] L. Bai, and D. Breen, *Calculating Center of Mass in an Unbounded 2D Environment*, Journal of Graphics, GPU, and Game Tools **13**, 53 (2008) (cit. on p. 68).

[149] M. Schwartzkopf, A. Hinz, O. Polonskyi, T. Strunskus, F. C. Löhrer, V. Körstgens, P. Müller-Buschbaum, F. Faupel, and S. V. Roth, *Role of Sputter Deposition Rate in Tailoring Nanogranular Gold Structures on Polymer Surfaces*, ACS Applied Materials & Interfaces **9**, 5629 (2017) (cit. on p. 81).

[150] M. Körner, M. Einax, and P. Maass, *Island size distributions in submonolayer growth: Prediction by mean field theory with coverage dependent capture numbers*, Physical Review B **82**, 201401 (2010) (cit. on p. 90).

[151] M. Smoluchowski, *Drei Vorträge über Diffusion, Brownsche Molekularbewegung und Koagulation von Kolloidteilchen*, Zeitschrift für Physik **17**, 557 (1916) (cit. on p. 93).

[152] B. M. Smirnov, *Processes involving clusters and small particles in a buffer gas*, Physics-Uspekhi **54**, 691 (2011) (cit. on p. 93).

[153] R. Ferrando, J. Jellinek, and R. L. Johnston, *Nanoalloys: From Theory to Applications of Alloy Clusters and Nanoparticles*, Chemical Reviews **108**, 845 (2008) (cit. on p. 99).

[154] E. Ringe, J. M. McMahon, K. Sohn, C. Cobley, Y. Xia, J. Huang, G. C. Schatz, L. D. Marks, and R. P. Van Duyne, *Unraveling the Effects of Size, Composition, and Substrate on the Localized Surface Plasmon Resonance Frequencies of Gold and Silver Nanocubes: A Systematic Single-Particle Approach*, The Journal of Physical Chemistry C **114**, 12511 (2010) (cit. on p. 99).

[155] F. Baletto, C. Mottet, and R. Ferrando, *Growth simulations of silver shells on copper and palladium nanoclusters*, Physical Review B **66**, 155420 (2002) (cit. on p. 99).

[156] G. Rossi, A. Rapallo, C. Mottet, A. Fortunelli, F. Baletto, and R. Ferrando, *Magic Polyicosahedral Core-Shell Clusters*, Physical Review Letters **93**, 105503 (2004) (cit. on p. 99).

[157]   A. Rapallo, G. Rossi, R. Ferrando, A. Fortunelli, B. C. Curley, L. D. Lloyd, G. M. Tar-
        buck, and R. L. Johnston, *Global optimization of bimetallic cluster structures. I. Size-
        mismatched Ag–Cu, Ag–Ni, and Au–Cu systems*, J. Chem. Phys. **122**, 194308 (2005)
        (cit. on p. 99).

[158]   P. Grammatikopoulos, J. Kioseoglou, A. Galea, J. Vernieres, M. Benelmekki, R. E. Diaz,
        and M. Sowwan, *Kinetic trapping through coalescence and the formation of patterned
        Ag-Cu nanoparticles*, Nanoscale **8**, 9780 (2016) (cit. on pp. 99, 102, 105, 111).

[159]   Y. Hu, A.-Q. Zhang, H.-J. Li, D.-J. Qian, and M. Chen, *Synthesis, Study, and Discrete
        Dipole Approximation Simulation of Ag-Au Bimetallic Nanostructures*, Nanoscale Re-
        search Letters **11**, 209 (2016) (cit. on p. 100).

[160]   R. D. Corpuz, Y. Ishida, M. T. Nguyen, and T. Yonezawa, *Synthesis of Positively Charged
        Photoluminescent Bimetallic Au–Ag Nanoclusters by Double-Target Sputtering Method
        on a Biocompatible Polymer Matrix*, Langmuir **33**, 9144 (2017) (cit. on p. 100).

[161]   G. Radnóczi, E. Bokányi, Z. Erdélyi, and F. Misják, *Size dependent spinodal decomposition
        in Cu-Ag nanoparticles*, Acta Materialia **123**, 82 (2017) (cit. on p. 100).

[162]   P. L. Williams, Y. Mishin, and J. C. Hamilton, *An embedded-atom potential for the
        Cu–Ag system*, Modelling and Simulation in Materials Science and Engineering **14**,
        817 (2006) (cit. on p. 102).

[163]   J. W. Abraham, and M. Bonitz, *Molecular dynamics simulation of Ag–Cu cluster growth
        on a thin polymer film*, Contributions to Plasma Physics **58**, 164 (2018) (cit. on pp. 104,
        106, 107, 110).

[164]   X. He, F. Cheng, and Z.-X. Chen, *The Lattice Kinetic Monte Carlo Simulation of Atomic
        Diffusion and Structural Transition for Gold*, Scientific Reports **6**, 33128 (2016) (cit. on
        p. 115).

[165]   C. H. Turner, Y. Lei, and Y. Bao, *Modeling the atomistic growth behavior of gold nanopar-
        ticles in solution*, Nanoscale **8**, 9354 (2016) (cit. on p. 115).

Acknowledgments

The present thesis owes its existence to the many people who generously assisted me throughout my doctoral journey.

First and foremost, I would like to express my sincere gratitude to my supervisor, Prof. Dr. Michael Bonitz, for the advice, guidance and care he has provided ever since I first joined his group in 2010. Over the years, I greatly benefited from his knowledge and scientific expertise. Furthermore, he gave me the invaluable opportunity to present my research at various domestic and international conferences, thus allowing me to become an active member of the scientific community.

For the long-standing collaboration, I am grateful to Prof. Dr. Franz Faupel and his group members Dr. Thomas Strunskus, Dr. Oleksandr Polonskyi and Alexander Hinz. Their experimental work provided the motivation for my computational investigations, and I learned a lot from them about metal–polymer nanocomposites.

I also thank Nuttawut Kongsuwan and Kangkang Wang, who gave me the opportunity to supervise their projects during their RISE internships in summer 2014 and 2015, respectively.

Finally, I wish to thank my colleagues for the friendly atmosphere and their willingness to share their knowledge. In particular, I am indebted to XXXwho proofread the manuscript of this thesis.

Selbständigkeitserklärung

Ich erkläre, dass die vorliegende Abhandlung – abgesehen von der Beratung durch den Betreuer – nach Inhalt und Form die eigene Arbeit ist.

Außerdem versichere ich, dass die Arbeit in dieser Form weder ganz noch zum Teil schon einer anderen Stelle im Rahmen eines Prüfungsverfahrens vorgelegen hat, noch nicht veröffentlicht worden ist und auch nicht zur Veröffentlichung eingereicht worden ist. Die hier vorgestellten Ergebnisse sind zum größten Teil bereits in wissenschaftlichen Fachzeitschriften publiziert worden. Eine ausführliche Publikationsliste findet sich auf Seite iii.

Die Arbeit ist unter Einhaltung der Regeln guter wissenschaftlicher Praxis der Deutschen Forschungsgemeinschaft entstanden.

_____
Ort, Datum

_____
Jan Willem Abraham